

Wave function-based electronic structure theory for solids

Malte Lange

Submitted in partial fulfillment of the  
requirements for the degree of  
Doctor of Philosophy  
under the Executive Committee  
of the Graduate School of Arts and Sciences

COLUMBIA UNIVERSITY

2021

© 2021

Malte Lange

All Rights Reserved

## **Abstract**

Application of wave function methods to solid-state systems

Malte Lange

This thesis describes the application of wave function-based and perturbative methods to extended systems, primarily semiconductors. In Chapter 1, I introduce the quantum chemistry problem along with current progress in the field. I then provide some requisite fundamental theory associated with the wave function-based methods and periodic boundary conditions. In Chapter 2, I describe the relationship between the traditional extended system GW method and the traditionally molecular coupled-cluster formalism through diagrammatic analysis. We find that the popular coupled cluster singles and doubles (CCSD) method contains most of the diagrams in GW theory and more, and the more accurate coupled cluster singles and doubles with perturbative triples (CCSD(T)) method contains all GW diagrams and more. Benchmarking on the GW100 test set indicates that CCSD and a number of its approximations are more accurate than GW theory.

In Chapter 3, I evaluate the potential for using composite schemes to reduce the computational cost of the CCSD method. We use focal point and downfolding techniques for excited state results for the GW100 along with some sample solids. Using composite methods reduces the cost of CCSD by reducing the number of orbitals treated at a higher level of theory, which is very similar to the active space methods used in single- and multi-reference calculations.

In Chapters 4 and 5, I describe how to best treat finite size effects for wave function-based

methods, including the impact of including terms like the Madelung constant and which extrapolation form to use. After establishing this, we use the prescribed procedure to compare the equation-of-motion second-order Møller-Plesset (EOM-MP2) method to the MP2 method of Grüneis and the GW method for a standard test set of 11 solid-state systems. We find that the MP2 method performs qualitatively and quantitatively poorly for extended systems, but EOM-MP2 and GW perform qualitatively well, with quantitative MAEs of 0.40 and 0.68eV, respectively relative to a zero-point corrected electronic band gap.

## Table of Contents

Acknowledgments . . . . .	iv
Dedication . . . . .	v
Chapter 1: Introduction . . . . .	1
1.1 Current Field . . . . .	1
1.2 Hartree-Fock . . . . .	5
1.3 Electron Correlation and Coupled-Cluster Theory . . . . .	6
1.4 Equation-of-Motion Coupled-Cluster Theory . . . . .	9
1.5 Periodic systems . . . . .	10
1.5.1 Periodic Hartree-Fock . . . . .	11
1.5.2 Periodic Coupled-Cluster . . . . .	11
1.6 Summary . . . . .	12
Chapter 2: Relationship between EOM-CC and GW Theory . . . . .	13
2.1 Introduction . . . . .	13
2.2 Theory . . . . .	15
2.2.1 The one-particle Green's function . . . . .	15
2.2.2 The <i>GW</i> approximation . . . . .	16
2.2.3 Equation-of-motion coupled-cluster theory . . . . .	19

2.3	Comparing the <i>GW</i> approximation and EOM-CC theory . . . . .	22
2.3.1	Comparing the Green's function . . . . .	22
2.3.2	Comparing the self-energy . . . . .	25
2.4	Application of EOM-CCSD to the <i>GW</i> 100 test set . . . . .	30
2.4.1	Approximations to EOM-CCSD . . . . .	30
2.4.2	Numerical details . . . . .	33
2.4.3	Comparison to $\Delta$ CCSD(T) ionization potentials . . . . .	34
2.4.4	Electron affinities and higher-energy excitations . . . . .	35
2.4.5	Accuracy of approximate EOM-CCSD . . . . .	38
2.5	Conclusions and outlook . . . . .	40
Chapter 3: Composite and Hybrid Methods . . . . .		42
3.1	Introduction . . . . .	42
3.2	Theory . . . . .	44
3.2.1	Orbitals and excitations . . . . .	44
3.2.2	Ground-state approximations . . . . .	45
3.2.3	Excited-state approximations . . . . .	48
3.3	Results . . . . .	49
3.3.1	Molecules . . . . .	50
3.3.2	Solids . . . . .	52
3.4	Conclusions . . . . .	55
Chapter 4: Finite-size effects in post-Hartree-Fock calculations of solids . . . . .		57
4.1	Introduction . . . . .	57

4.2	Integrable divergences . . . . .	58
4.2.1	Hartree-Fock theory . . . . .	58
4.2.2	Perturbation theory . . . . .	61
4.2.3	Coupled-cluster theory . . . . .	62
4.2.4	IP/EA equation-of-motion coupled-cluster theory . . . . .	65
4.3	The periodic Ewald potential . . . . .	67
4.3.1	Hartree Fock theory . . . . .	69
4.3.2	Perturbation theory . . . . .	71
4.3.3	Coupled-cluster theory . . . . .	73
4.3.4	IP/EA equation-of-motion coupled-cluster theory . . . . .	73
4.4	The shifted Ewald potential . . . . .	74
4.4.1	Hartree-Fock theory . . . . .	75
4.4.2	Perturbation theory . . . . .	76
4.4.3	Coupled-cluster theory . . . . .	77
4.4.4	IP/EA equation-of-motion coupled-cluster theory . . . . .	77
4.5	Conclusions and outlook . . . . .	78
Chapter 5: Improved MP2 band gaps of semiconductors and insulators . . . . .		79
5.1	Introduction . . . . .	79
5.2	Theory . . . . .	80
5.3	Results and Discussion . . . . .	82
5.4	Conclusion . . . . .	86
References . . . . .		88

## **Acknowledgements**

First and foremost I would like to thank my advisor Tim Berkelbach for his support and patience as I trekked through my PhD. He has been a great role model, helping me to continuously improve and push myself to perform and communicate better science.

Unsurprisingly, my colleagues throughout my PhD played a large role, especially those that I (and the group) started with at UChicago. Jonathan and Yeongsu helped me at every step and braved all of struggles together with me. The postdocs throughout my PhD were generous with their time, especially Xiao and Bryan who answered my many questions. I would like to especially thank Sam and James who were both great colleagues and friends outside of work. Their ideas and energy shaped a lot of the great things I got out of my PhD.

I would also like to thank all of my friends at UChicago who I had to unfortunately leave for Columbia, especially Chris, Hannah, Ahmad, Jeff, and Mark. But I fortunately made some good friends at Columbia including Jake, Matt, Sergio, and Ketan who made the move and re-start much easier.

I'd also like to thank my committee that helped me start at UChicago, Profs. Dmitri Talapin, David Mazzioti, and Greg Voth. And also my committee at Columbia that were willing to proctor my fourth year and thesis defenses, Profs. Rich Friesner, Angelo Cacciuto, David Reichman, and Chris Marianetti.

Finally, I'd like to thank my family, especially my parents and Gabby, who helped me the entire way, both intellectually and emotionally.

## **Dedication**

For Olive.

# Chapter 1: Introduction

## 1.1 Current Field

As technology and innovation are changing at an accelerating pace, many researchers, companies, and governments are increasingly turning to computational fields to manage large problem spaces and the need for high accuracy. Big data and informatics are perhaps the most recognizable examples, driving hot topics like social media, machine learning, delivery, drug discovery, and personalized healthcare, to name a few. Due to environmental pressures, there is also increasing technological innovation and change happening in energy technologies, especially in the solar energy and battery technology sectors. Computational fields, such as computational chemistry are becoming more and more important for applications such as drug discovery and energy materials.

To address these issues, computational chemists are faced with making predictions for increasingly larger systems at higher accuracy. This requires *ab-initio* methods that scale well (or parallelize well for high-performance computing) and exhibit small errors (on the order of 1kcal/mol) or are at least systematically improvable. Fortunately researchers have been making tremendous progress on many different types of methods for addressing these needs for a variety of chemistries, including but not limited to molecules, extended systems, transition metals, and superconductors. Additionally, advances in hardware capabilities are quickly pushing the feasible system sizes that can be computed. Thus this is an exciting time for computational chemists, as rapid innovation is placing computation front and center in novel material discovery.

Traditionally the density functional theory (DFT) and so-called GW theory have been the workhorses for tackling extended systems due to their relatively good accuracy and low relative computational cost. While DFT has a formal scaling of  $O(N^3)$  and through computational improvements now an  $O(N)$  scaling, the heavy reliance on the form of the exchange-correlation

functional has made DFT a poor choice for benchmarking and reliable predictions. These issues are further inherited by the GW method, resulting in high performance variability based on the chosen DFT reference. Furthermore, as an excited state formalism, GW itself is formally exact, but practical implementations fail to easily incorporate higher order (so-called vertex) corrections, making systematic improvement difficult to achieve. Therefore, while DFT and GW offer relatively good results, their inability to provide theoretically sound benchmarks makes further method development for extended systems tricky.

This thesis attempts to tackle this reliability issue by adapting well understood and reliable methods from molecular electronic structure. For a long time now, CC with singles, double, and perturbative triples [CCSD(T)] has been the "gold standard" of quantum chemistry for purposes of benchmarking and achieving chemical accuracy with respect to experiment. I will focus on perturbation theory (Møller-Plesset) and the coupled-cluster formalism, as these complement each other well and are easily linked through theory. Furthermore, the CC formalism easily supports systematic improvements through higher orders and excited state formalisms, such as equation-of-motion (EOM). Unfortunately, applying either perturbation methods or coupled-cluster theory is computationally very expensive due to their at least  $O(N^5)$  scaling.

Some initial attempts of applying wave function methods to solids have looked very promising for ground state observables such as the cohesion energy and bulk modulus[1, 2] as well as excited state observables such band structures[1, 3] and neutral excitations[4]. Other efforts have looked much less promising, showing that second-order perturbation methods can result in qualitatively incorrect results[5] or unreliable[6]. It seems that the success and failures of these results can be traced back to finite-size errors and basis set errors which are further compounded by the computational costs of wave function methods making requisite calculations for addressing these issues too expensive.

Fortunately, prior work has explored the effect of finite-size effects and possible methods for amelioration through twist-averaging and extrapolation methods[7]. Much of this has been borrowed from the QMC community[8] where finite-size errors are a primary source of error as

well. Basis set effects for solids have not been explored as extensively, with the field primarily using pseudopotential-based basis sets[mcclain2017aa, 3], although some work of introducing all-electron basis sets is underway[9]. The issue of computational complexity is being addressed by a variety of approaches. Some progress is being made in purely computational approaches such as embedding techniques[10, 11, 12], focal point techniques[], and coulomb integral solvers[13]. Other attempts consist of finding low-scaling approximations to CC with singles, doubles (CCSD) and CCSD(T)[14, 15, 16] or solving the periodic Schrödinger problem using stochastic methods[17].

My work has helped in improving the practical applications of perturbation theory and coupled cluster to ground state and excited state observables in solids. I helped in better understanding and reliably removing finite-size errors by addressing the root cause of finite size errors (an integrable divergence) and giving best practices for setting up calculations along with the correct convergence behaviors (see Chapter 4). I also explored the potential for using composite and interacting schemes for lower the computational cost of CCSD calculations with minimal impact on accuracy (see Chapter 5). The culmination of this work has been a set of benchmarks for a variety of solids which will aid further method development and bring the field closer to chemically accurate and reliable methods for solids.

Tangential to progress in the solid state, progress in understanding and addressing computational cost and basis set errors in molecular systems is the starting point for applying these in solids. Extensive progress is being made for improved basis sets either through R12/F12 methods[18, 19, 20, 21, 22] or better extrapolation techniques for achieving the complete basis set limit[23, 24, 25, 26, 27]. Outstanding challenges for R12/F12 methods include, but are not limited to choosing the correct correlation factor[28, 29], efficient calculation of multi-electron integrals with general correlation factors[28], and higher order many-body interactions[30]. For reviews of progress in addressing finite basis set errors, see[29, 31, 32, 33, 34, 35, 36].

Computational cost has been a long standing issue in the computational chemistry field. Some of the most promising avenues with possible applications to solids include embedding methods[10,

11, 12] and local methods[37, 38, 39, 40, 41], with methods such as the domain-localized pair natural orbital approach yielding linear scaling for methods such as CCSD and CCSD(T)[42, 43]. Other attempts include composite methods[14, 15, 16] and perturbative approximations to CCSD and CCSDT[44], such as CC2 and CCSD(T). Similar approaches have been developed for the equation-of-motion (EOM) excited state formalism, which benefit from reduced scaling in the ground state reference as well as approximations to the EOM equations themselves[45, 46].

Progress in the GW community is also continuing to push forward the molecular and solid state fields. Current benchmarks for GW theory on band gaps of extended systems yield mean absolute errors on the order of 0.5eV relative to experiment, with some materials treated at sub 0.1eV accuracy. Current efforts are aiming to include phonon effects for improved band gap accuracy relative to experiment by using Allen, Heine, and Cardona (AHC) theory along with vertex corrections and partial self-consistency[47, 48, 49, 50, 51]. GW has also been combined with the dynamic mean field theory (DMFT) in order to tackle strongly correlated materials[52, 53]. While GW theory is difficult to improve systematically and has strong sensitivity to its reference (DFT or HF choice), it has historically performed well for solid state materials and can benefit greatly from improved benchmarks provided by wave function-based methods.

Although wave function-based methods like MP2 and CCSD are relatively new methods for extended systems, existing literature and an active community has led to rapid progress in the adoption of these methods. Borrowing from the DFT and GW communities as well as the existing molecular results for wave function-methods will continue to push forward efforts in the solid-state. Improvements to machine learning models may prove useful to heavily reducing computational cost, improving accuracy, and speeding up material screening. Together these fields are poised to be an important part of the future of technological innovations, especially in pressing areas like climate change.

## 1.2 Hartree-Fock

The electronic structure problem that we are interested in is the time-independent, non-relativistic Schrödinger equation in the Born-Oppenheimer approximation

$$\hat{H}|\Psi\rangle = E|\Psi\rangle \quad (1.1)$$

where

$$\hat{H} = -\sum_i^{N_e} \frac{1}{2} \nabla_i^2 - \sum_i^{N_e} \sum_A^{N_n} \frac{Z_A}{|\mathbf{r}_i - \mathbf{r}_A|} + \sum_{i>j}^{N_e} \frac{1}{|\mathbf{r}_i - \mathbf{r}_j|}, \quad (1.2)$$

is the Hamiltonian,  $\Psi$  is the wave function, and  $E$  is the energy. Here we are using atomic units,  $i, j, \dots$  as electronic indices,  $A, B, \dots$  as nuclear indices,  $M_A$  as the nuclear mass, and  $Z_A$  as the nuclear charge,  $N_e$  is the number of electrons, and  $N_n$  is the number of nuclei.

Approximating the exact ground-state wave function with the lowest-energy single Slater determinant  $\Phi$  defines the Hartree-Fock method. To evaluate the Hartree-Fock energy, we take the expectation value of the Hamiltonian relative to the trial wave function

$$E_{HF} = \langle \Phi | \hat{H} | \Phi \rangle. \quad (1.3)$$

In practice, we must choose a finite one-particle basis from which to build the wave function. We choose the linear combination of atomic orbitals (LCAO) method, since this description of electron behavior appeals readily to chemical intuition. We then build our molecular orbitals (MOs) from these atomic orbitals. Roothaan and Hall showed that using a finite basis, the Hartree-Fock equation above could be written as a generalized matrix eigenvalue equation,

$$\mathbf{FC} = \mathbf{SC}\boldsymbol{\varepsilon}, \quad (1.4)$$

where  $\mathbf{F}$  is the Fock matrix,  $\mathbf{C}$  is the coefficient matrix for the AOs,  $\mathbf{S}$  is the overlap matrix, and  $\boldsymbol{\varepsilon}$  is the energy matrix whose diagonal are the MO energies. Because the Fock matrix depends on

the unknown solution matrix  $\mathbf{C}$ , the eigenvalue equation is solved using the self-consistent field (SCF) method. Once completed, the self-consistent HF result will yield the canonical HF orbitals and energies. By the Aufbau principle, the lowest  $N$  of these are identified as occupied and the remainder are unoccupied (virtual) orbitals. While not physical, these virtual orbitals are important for constructing many-body wave functions beyond the HF Slater determinant.

The correlated methods that we cover in the next section move beyond the mean-field HF picture and include explicit electron-electron interactions. In quantum chemistry, the correlation energy is defined to be the difference between the exact energy and the Hartree-Fock energy

$$E_{corr} = E - E_{HF}. \quad (1.5)$$

We explore the concept of correlation in the next section.

### 1.3 Electron Correlation and Coupled-Cluster Theory

The lack of correlation in HF comes from choosing only a single determinant to express the wave function. To rectify this, we include more determinants, thus the  $N$ -body trial wave function becomes a weighted sum of determinants (including the HF determinant). To obtain these additional determinants, we introduce excitations of the reference HF determinant by moving electrons from the occupied orbitals into the virtual orbitals. In the limit of performing all permutations of excitations and weighting them correctly, we recover the true  $N$ -body wave function. Wave function methods that use only the single HF Slater determinant as a reference are referred to as single-reference methods and are said to recover dynamic correlation. There are also so-called multi-reference methods which perform excitations on top of multiple reference determinants, which are necessary to describe static correlation. In this thesis we will focus exclusively on perturbation and coupled-cluster methods that recover dynamic correlation.

Here we start with the full configuration interaction (FCI) method, which gives a formula for constructing the full  $N$ -body wave function. From there we will truncate the FCI expression to

reduce the factorial scaling to a tractable polynomial problem, resulting in truncated CI methods. Truncated CI schemes however no longer respect necessary size-consistency and size-extensivity, and so we then show how the CC formalism improves on the truncated CI methods.

The FCI wave function can be constructed from the HF reference (but also other references),  $|\Phi_0\rangle$  using an excitation operator  $\hat{C}$ ,

$$|\Psi\rangle = \hat{C} |\Phi_0\rangle = (1 + \hat{C}_1 + \hat{C}_2 + \hat{C}_3 + \dots) |\Phi_0\rangle, \quad (1.6)$$

where  $\hat{C}_n$  are excitation operators,

$$\begin{aligned} \hat{C}_1 &= \sum_i^{\text{occ}} \sum_a^{\text{vir}} r_i^a a_a^\dagger a_i, & \hat{C}_2 &= \frac{1}{4} \sum_{ij}^{\text{occ}} \sum_{ab}^{\text{vir}} r_{ij}^{ab} a_a^\dagger a_b^\dagger a_i a_j, \\ \hat{C}_n &= \frac{1}{(n!)^2} \sum_{ij\dots k}^{\text{occ}} \sum_{ab\dots c}^{\text{vir}} r_{ij\dots k}^{ab\dots c} a_a^\dagger a_b^\dagger \dots a_c^\dagger a_i a_j \dots a_k. \end{aligned} \quad (1.7)$$

For a given operator order, we remove  $n$  electrons from occupied orbitals and place them into  $n$  virtual orbitals to construct new determinants. However, including all of these excitations grows factorially in  $N$ , and so for computational purposes we typically need to truncate the FCI expansion. Typically truncations are limited to singles, doubles (CISD) or singles, doubles, and triples (CISDT), as even these still scale as  $O(N^6)$  and  $O(N^8)$ , respectively. However, by truncating the FCI wave function, the energy is no longer size-extensive, which is a critical feature for calculations on large molecules or extended systems.

Instead we turn to the coupled-cluster (CC) formalism which includes "disconnected" product terms at each truncation order to approximate higher order interactions. By allowing lower orders to approximate higher orders, CC inherently includes up to infinite-order excitations and thus solves the size-extensivity issue. In the limit of "full" CC and CI, the two methods converge to the exact wave function.

CC theory is usually defined by the exponential ansatz,

$$|\Psi\rangle = e^{\hat{T}} |\Phi_0\rangle \quad (1.8)$$

where the  $T$  operator is  $T = T_1 + T_2 + \dots$ , with

$$\hat{T}_1 = \sum_i^{occ} \sum_a^{vir} t_i^a a_a^\dagger a_i, \quad \hat{T}_2 = \frac{1}{4} \sum_{ij}^{occ} \sum_{ab}^{vir} t_{ij}^{ab} a_a^\dagger a_b^\dagger a_j a_i, \quad (1.9a)$$

$$\hat{T}_n = \frac{1}{(n!)^2} \sum_{ij\dots k}^{occ} \sum_{ab\dots c}^{vir} t_{ij\dots k}^{ab\dots c} a_a^\dagger a_b^\dagger \dots a_c^\dagger a_k \dots a_j a_i. \quad (1.9b)$$

We insert the CC wave function into the Schrödinger equation

$$\hat{H} e^{\hat{T}} |\Phi\rangle = E e^{\hat{T}} |\Phi\rangle. \quad (1.10)$$

Multiplying on the left with the inverse exponential and then left projecting with the bra, we get,

$$\langle \Phi | e^{-\hat{T}} \hat{H} e^{\hat{T}} | \Phi \rangle = E, \quad (1.11)$$

We now have the so-called "similarity-transformed" Hamiltonian,  $\bar{H} = e^{-\hat{T}} \hat{H} e^{\hat{T}}$ . Eq. 1.11 defines the CC energy equation, but it doesn't address how to determine the amplitudes of the  $T$  operator  $t_{ij}^{ab\dots}$ . For this we need the amplitude equations, which we obtain through left projecting with excited determinants,

$$\langle \Phi_{ij\dots}^{ab\dots} | e^{-\hat{T}} \hat{H} e^{\hat{T}} | \Phi \rangle = 0. \quad (1.12)$$

The energy equation, Eqs. 1.11, and amplitude equations, 1.12, define CC theory.

Programmable equations for CC theory of arbitrary order can be derived using the tools of many-body theory, described, e.g. in Ref. [54]. For example, the energy equation is

$$E_{CC} - E_0 = \sum_{ia} f_{ia} t_i^a + \frac{1}{4} \sum_{ijab} \langle ij || ab \rangle t_{ij}^{ab} + \frac{1}{2} \sum_{ijab} \langle ij || ab \rangle t_i^a t_j^b. \quad (1.13)$$

where  $f_{ia}$  are matrix elements of the Fock operator and  $\langle ij||ab\rangle$  are antisymmetrized two-electron integrals. The work in this thesis primarily considers the CCSD level of theory. Solving the CCSD equations scales as  $O(N_o^2 N_v^4)$ , where  $N_o$  is the number of occupied orbitals and  $N_v$  is the number of virtual orbitals, or  $O(N^6)$  in the system size  $N$ .

## 1.4 Equation-of-Motion Coupled-Cluster Theory

Much of this thesis is focused on the excited state properties of solid-state systems, especially the ionization potentials (IPs) and electron affinities (EAs) that define the band structure and band gap. While IPs and EAs can be found by subtracting the energies of two ground state calculations, this method is complicated, because it invariably requires at least one open-shell calculation and makes obtaining higher lying IPs and EAs difficult. Thus we are interested in a framework that allows direct calculation of excited states from a single ground state. This is achieved by equation-of-motion CC (EOM-CC). The EOM framework builds on top of the ground state results from CC and is mathematically and intuitively similar to configuration interaction; however, here we use the CC ground state as a reference rather than the HF determinant. The excited state wavefunction is written as

$$|\Psi_k\rangle = \hat{R}_k |\Psi_0\rangle = \hat{R}_k e^{\hat{T}} |\Phi_0\rangle \quad (1.14)$$

where  $\hat{R}_k$  is an excitation operator. When our new wave function  $\Psi_k$  is inserted in the Schrödinger equation, we end up with an eigenvalue equation,

$$\hat{H} |\Psi_k\rangle = \hat{H} \hat{R}_k e^{\hat{T}} |\Phi_0\rangle = E_k \hat{R}_k e^{\hat{T}} |\Phi_0\rangle. \quad (1.15)$$

Left-multiplying by  $e^{-\hat{T}}$  as we did for the ground state and using the fact that  $\hat{R}_k$  and  $\hat{T}$  commute,

$$e^{-\hat{T}} \hat{H} \hat{R}_k e^{\hat{T}} |\Phi_0\rangle = e^{-\hat{T}} \hat{H} e^{\hat{T}} \hat{R}_k |\Phi_0\rangle = E_k \hat{R}_k |\Phi_0\rangle, \quad (1.16)$$

we see that the EOM problem is the eigenvalue problem of diagonalizing the similarity-transformed Hamiltonian,  $\bar{H} = e^{-\hat{T}}\hat{H}e^{\hat{T}}$  in the space of excited HF determinants,  $\hat{R}_k |\Phi_0\rangle$ . This is the primary difference between CI and the EOM-CC framework: in CI one diagonalizes the "bare" Hamiltonian,  $\hat{H}$ , but in the EOM-CC framework one diagonalizes the "dressed" Hamiltonian,  $\bar{H}$ .

For IPs, the excitation operator is

$$\hat{R}_k^{IP} = \sum_i r_i(k) a_i + \sum_{ija} r_{ij}^a(k) a_a^\dagger a_i a_j \quad (1.17)$$

and for EAs, the excitation operator is

$$\hat{R}_k^{EA} = \sum_a r^a(k) a_a^\dagger + \sum_{iab} r_i^{ab}(k) a_a^\dagger a_i a_b^\dagger. \quad (1.18)$$

The matrix-vector multiplication used to iteratively find IPs and EAs scales as  $O(N_o^3 N_v^2)$  and  $O(N_o^2 N_v^3)$ , respectively, or  $O(N^5)$  overall.

## 1.5 Periodic systems

In order to apply the above methods to periodic systems like crystals, we use symmetry-adapted basis functions and periodic boundary conditions. In the work presented in this thesis, we choose atomic orbitals that are translational-symmetry-adapted linear combinations of Gaussian AOs

$$\phi_{\mu\mathbf{k}}(\mathbf{r}) = \sum_{\mathbf{T}} e^{i\mathbf{k}\cdot\mathbf{T}} \tilde{\phi}_\mu(\mathbf{r} - \mathbf{T}) \equiv e^{i\mathbf{k}\cdot\mathbf{T}} u_{\mu\mathbf{k}}(\mathbf{r}), \quad (1.19)$$

where  $u_{\mu\mathbf{k}}(\mathbf{r})$  is a Bloch function fully periodic with respect to all lattice translations  $\mathbf{T}$ . Another popular choice for basis functions of periodic systems are plane waves. In the above,  $\mathbf{k}$  is a crystal momentum in the first Brillouin zone, which is typically sampled using a uniform mesh. The thermodynamic limit is achieved in the limit of infinitely dense sampling of momenta in the Brillouin zone. The translational invariance of the Hamiltonian leads a conservation of crystal momentum. The cost of periodic calculations is reduced by explicitly using this symmetry.

### 1.5.1 Periodic Hartree-Fock

In the above symmetry-adapted basis, the periodic HF equations are

$$\mathbf{F}^{(k)} \mathbf{C}^{(k)} = \mathbf{S}^{(k)} \mathbf{C}^{(k)} \boldsymbol{\epsilon}^{(k)}. \quad (1.20)$$

Matrices are built for each  $k$ -point, e.g. the overlap matrix is

$$S_{\mu\nu}(\mathbf{k}) = \int_{\Omega} d\mathbf{r} \phi_{\mu,\mathbf{k}}^*(\mathbf{r}) \phi_{\nu,\mathbf{k}}(\mathbf{r}), \quad (1.21)$$

where  $\Omega$  is the volume of the unit cell.

### 1.5.2 Periodic Coupled-Cluster

For our excitation processes in CC theory, the crystal momenta of the orbitals must be defined, e.g.

$$\sum_{ia} t_i^a(\dots) \rightarrow \sum_{ia} \sum_{\mathbf{k}_i \mathbf{k}_a} t_{i\mathbf{k}_i}^{a\mathbf{k}_a}(\dots). \quad (1.22)$$

Conservation of crystal momentum requires that

$$(\mathbf{k}_a - \mathbf{k}_i) \cdot \mathbf{a} = 2\pi m \quad (1.23)$$

for single excitations and

$$(\mathbf{k}_a + \mathbf{k}_b - \mathbf{k}_i - \mathbf{k}_j) \cdot \mathbf{a} = 2\pi m \quad (1.24)$$

for double excitations. Here  $m$  is an integer and  $\mathbf{a}$  is a lattice vector. Although conventional CCSD scales as  $O(N^6)$ , periodic CCSD scales as  $O(N_k^4 n^6)$  where  $N_k$  is the number of  $k$ -points sampled in the Brillouin zone and  $n$  is the number of orbitals in the unit cell.

For the ionization potentials (IPs) and electron affinities (EAs), we are interested in the quasi-particle behavior at a given  $k$ -points. The IP excitation operator for periodic systems at a given

k-point,  $\mathbf{k}_{IP}$ , is written

$$\hat{R}^{IP}(n, \mathbf{k}_{IP}) = \sum_i r_{i\mathbf{k}_{IP}}(n) a_{i\mathbf{k}_{IP}} + \sum_{ija} \sum'_{\mathbf{k}_i \mathbf{k}_j \mathbf{k}_a} r_{i\mathbf{k}_i \mathbf{k}_j \mathbf{k}_a}^{a\mathbf{k}_a}(n) a_{a\mathbf{k}_a}^\dagger a_{i\mathbf{k}_i} a_{j\mathbf{k}_j} \quad (1.25)$$

where the primed summation requires that

$$(\mathbf{k}_{IP} - \mathbf{k}_i - \mathbf{k}_j + \mathbf{k}_a) \cdot \mathbf{a} = 2\pi m. \quad (1.26)$$

An analogous excitation operator can be defined for the EA problem. The scaling of periodic IP/EA-EOM-CCSD is  $O(N_k^3 n^5)$ .

## 1.6 Summary

In the first chapter we gave an overview of some of the exciting advances in quantum chemistry, ranging from low-scaling methods to applications in the solid state. We then introduced the quantum chemistry problem and reviewed the theory for ground and excited state Hartree-Fock and coupled-cluster formalisms. In the following chapters we will delve into the relationship between CC and GW theories, investigate the performance of lower-scaling and composite methods, and finally the correct handling of finite-size effects in solid-state systems. By the end, the goal is to give a promising standard of protocol for how to correctly apply traditional molecular methods such as HF and CC to solid-state systems in cost-effective ways.

## Chapter 2: Relationship between EOM-CC and GW Theory

The material for this chapter was taken from Reference [55]

### 2.1 Introduction

The accurate calculation of excited-state properties constitutes one of the major challenges in modern computational materials science. For charged excitations, namely the ionization potentials and electron affinities as measured by photoelectron spectroscopy, the  $GW$  approximation has proven to be a powerful and successful tool in the condensed phase. Formally, the  $GW$  approximation (reviewed below) arises as the lowest-order self-energy diagram when the one-particle Green's function  $G$  is expanded in terms of the screened Coulomb interaction  $W$  [56, 57], with screening treated in the random-phase approximation. Neglected diagrams can be assigned to vertex corrections (appearing both in the self-energy and the polarization propagator), which are a natural target for post- $GW$  theories and an ongoing area of activity [58, 59, 60, 61, 62].

In contrast to time-dependent Green's function-based diagrammatic theories, wavefunction-based theories and concomitant time-independent perturbation theory offer an alternative route towards systematically improvable excited-state calculations [63]. The great variety of wavefunction ansatzes, combined with the long history of development and benchmarking in the molecular quantum chemistry community, makes such approaches particularly promising. Unfortunately, the formal comparison between wavefunction-based and Green's function-based techniques is complicated by a difference in both the approach and the language. Here, we present such a comparison, by analyzing the one-particle Green's function calculated using equation-of-motion coupled-cluster theory to that calculated using the  $GW$  approximation. A relation between the two can be anticipated based on the known exact relation between total *ground-state* energies calculated using

the ring coupled-cluster doubles approach and using the random-phase approximation [64, 65, 66], the latter of which is at the heart of screening in the  $GW$  approximation. However, for charged excitation energies, the equivalence is not so straightforward.

Although this article focuses on the connections between the  $GW$  approximation and EOM-CC theory because of their shared connections to the random-phase approximation [64, 65, 66], we emphasize that a number of other Green’s function techniques have been developed and used successfully on molecular problems [67, 68]. A non-exhaustive list of the most popular approaches include those that are essentially finite-order – such as the outer-valence Green’s function approach [67], the partial third-order (P3) approach [69], and its renormalized variant (P3+) [70] – and those that are rigorously infinite-order – such as the two-particle-hole Tamm-Dancoff approximation [71], its extended variant [72], the algebraic diagrammatic construction (ADC) [73], and the nondiagonal renormalized approach exact to second order (NR2) [74]. Recently there has been renewed interest in the second-order Green’s function [75], especially in its self-consistent [76, 77] and finite-temperature [78] variations. We emphasize that many of the above methods exhibit an attractive  $N^5$  scaling, whereas the  $GW$  approximation and EOM-CCSD both exhibit  $N^6$  scaling (see below), which we identify as the cost needed for a rigorous treatment of RPA physics.

In wavefunction-based techniques, ionization potentials and electron affinities can either be calculated as a difference in ground-state energies (between the neutral and ionic systems) or via the equation-of-motion framework, which directly results in an eigensystem whose eigenvalues are the ionization potentials or electron affinities. Equation-of-motion coupled-cluster (EOM-CC) theory is one such framework, which typically achieves accurate excitation energies when performed with single and double excitations (EOM-CCSD) [79, 80]. At the intersection of these methods, Nooijen and Snijders derived a one-particle Green’s function in the CC framework [81, 82], the poles and residues of which are precisely those of the conventional EOM-CC formalism (in the bivariational framework). The CC Green’s function has seen a renewed interest in recent years [3, 83, 84, 85, 86, 87, 88]. One of the main goals of the present work is to relate the latter theory to the  $GW$  approximation, which is carried out in Sec. 2.3.

A number of *numerical* comparisons between Green’s function-based and wavefunction-based techniques for charged excitation energies have been carried out in recent years. In particular, comparisons between the *GW* approximation and wavefunction-based techniques have been performed for one-dimensional lattice models [89], for a test set of 24 organic acceptor molecules [90], for oligoacenes [91], and for a test set of 100 molecules [92, 93]; the latter test set is known as the *GW100*, introduced in Ref.[94], and forms the basis of our numerical study in Sec. 3.3.

In light of recent efforts to bring the systematic improvability of wavefunction-based theories into the solid state [95, 5, 96, 97, 98, 99, 100, 3, 13, 1], we believe it timely to establish the relationship, both formally and numerically, between popular wavefunction approaches and Green’s function approaches – the latter of which has dominated solid-state electronic structure. Future work in both Green’s function-based and wavefunction-based approaches can benefit from the analysis and results of the present work.

The layout of this article is as follows. In Sec. 2.2, we provide the requisite theoretical background associated with general features of the one-particle Green’s function, the *GW* approximation to the self-energy, and equation-of-motion coupled-cluster theory. In Sec. 2.3, we perform a detailed diagrammatic comparison of the two methods, comparing separately their Green’s functions and self-energies. In Sec. 3.3, we use equation-of-motion coupled-cluster theory to calculate ionizations potentials and electron affinities of the *GW100* test set, and evaluate a number of accurate but efficient approximations, which are straightforwardly analyzed with the previously introduced diagrammatic description. In Sec. 3.4, we conclude with an outlook for future developments.

## 2.2 Theory

### 2.2.1 The one-particle Green’s function

The one-particle time-ordered Green’s function is defined by [101, 67]

$$iG_{pq}(\omega) = \int d(t_1 - t_2) e^{i\omega(t_1 - t_2)} \langle \Psi_0 | T[\hat{a}_p(t_1) \hat{a}_q^\dagger(t_2)] | \Psi_0 \rangle \quad (2.1)$$

where  $T$  is the time-ordering operator,  $\Psi_0$  is the exact interacting ground state, and  $p, q$  index a complete set of single-particle spin-orbitals. The irreducible self-energy matrix  $\Sigma(\omega)$  satisfies the relation  $\mathbf{G}(\omega) = [\omega - \mathbf{f} - \Sigma(\omega)]^{-1}$ , where  $\mathbf{f}$  is the matrix associated with some one-body (mean-field) operator such that  $\Sigma$  contains the remaining effects of the electronic interactions. Although in practice,  $\mathbf{f}$  is commonly the Kohn-Sham matrix of density functional theory, here we consider it to be the Fock matrix and will let  $p, q, r, s$  index the canonical Hartree-Fock (HF) orbitals, such that  $\mathbf{f}$  is diagonal:  $f_{pq} = \varepsilon_p \delta_{pq}$ . Following convention, indices  $i, j, k, l$  are used for the  $n_{\text{occ}}$  occupied orbitals in the HF determinant and  $a, b, c, d$  for the  $n_{\text{vir}}$  virtual (unoccupied) orbitals; in total there are  $M = n_{\text{occ}} + n_{\text{vir}}$  orbitals.

## 2.2.2 The GW approximation

The charged excitation energies (ionization potentials and electron affinities) occur at the poles of the Green's function, i.e. they are the self-consistent eigenvalues of a frequency-dependent one-particle matrix  $\mathbf{H}(\omega)$ :

$$\sum_q H_{pq}(\omega = E_n) R_q^n = E_n R_p^n, \quad (2.2)$$

with

$$H_{pq}(\omega) = \omega \delta_{pq} - [\mathbf{G}(\omega)]_{pq}^{-1} = \varepsilon_p \delta_{pq} + \Sigma_{pq}(\omega). \quad (2.3)$$

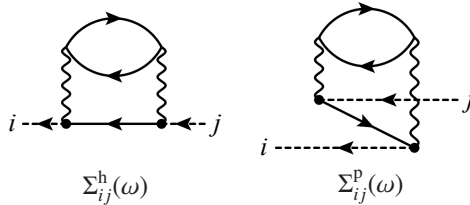


Figure 2.1: Lowest-order time-ordered (Goldstone) ring diagrams appearing in the hole (h) and particle (p) contributions to the self-energy, for occupied orbitals  $i, j$ . The dashed lines only serve to indicate the connectivity in a Goldstone diagram for the Green's function.

In the  $GW$  approximation [56], the self-energy is given by

$$\begin{aligned} \Sigma(\mathbf{r}_1, \mathbf{r}_2; \omega) &= \frac{i}{2\pi} \int d\omega' e^{i\eta\omega'} G(\mathbf{r}_1, \mathbf{r}_2; \omega + \omega') \\ &\quad \times W_c(\mathbf{r}_2, \mathbf{r}_1; \omega'), \end{aligned} \quad (2.4)$$

where  $W_c = W - v$  is the correlation part of the screened interaction; recall that the bare exchange term has been included (self-consistently) in the Fock operator  $\mathbf{f}$ . The dielectric function that screens the Coulomb interaction is evaluated with the random-phase approximation (RPA), corresponding to a resummation of all ring diagrams contributing to the polarization propagator; furthermore, all vertex corrections are neglected. Henceforth, we limit the discussion to the non-self-consistent  $G_0W_0$  approximation, where  $G_0$  and  $W_0$  are evaluated in a “one-shot” manner using the orbitals and orbital energies of the mean-field problem (in this case, HF). In a finite single-particle basis set, the frequency integration can be done analytically to show that the self-energy has separate hole (h) and particle (p) contributions [102, 103, 104],

$$\begin{aligned} \Sigma_{pq}(\omega) &= \Sigma_{pq}^h(\omega) + \Sigma_{pq}^p(\omega) \\ &= \sum_v \left\{ \sum_k \left[ \frac{[M_{kp}^v]^* M_{kq}^v}{\omega - (\varepsilon_k - \Omega_v) - i\eta} \right] + \sum_c \left[ \frac{[M_{cp}^v]^* M_{cq}^v}{\omega - (\varepsilon_c + \Omega_v) + i\eta} \right] \right\}, \end{aligned} \quad (2.5)$$

which are associated with the two possible time orderings (Goldstone diagrams) of the corresponding Feynman diagram for the self-energy, i.e.  $\Sigma_{pq}(t_2 - t_1)$  with  $t_2 > t_1$  or with  $t_2 < t_1$ . Expressed in terms of time-ordered Goldstone diagrams, the lowest-order ring diagrams appearing in the hole and particle contributions to the  $GW$  self-energy are shown in Fig. 2.1, for the single-particle indices  $i, j$  in the occupied orbital subspace. The poles of the  $GW$  self-energy occur at  $\omega = \varepsilon_k - \Omega_v$  and  $\omega = \varepsilon_c + \Omega_v$ , i.e. at sums and differences of the orbital energies  $\varepsilon_p$  and neutral excitation energies  $\Omega_v$ . For future reference, we note that – in gapped molecules and materials – the particle contribution to the self-energy of hole states is only weakly dependent on frequency, because the quasiparticle energy  $\omega \approx \varepsilon_k$  is far from the poles at  $\varepsilon_c + \Omega_v$ ; the separation is roughly twice the gap.

The transition amplitudes associated with the poles of the self-energy are given by

$$M_{pq}^\nu = \int d\mathbf{x}_1 d\mathbf{x}_2 \rho_\nu(\mathbf{x}_1) r_{12}^{-1} \phi_p^*(\mathbf{x}_2) \phi_q(\mathbf{x}_2) \quad (2.6)$$

where

$$\rho_\nu(\mathbf{x}) = \langle \Psi_0 | \hat{n}(\mathbf{x}) | \Psi_\nu \rangle = \sum_{pq} \phi_p^*(\mathbf{x}) \phi_q(\mathbf{x}) \langle \Psi_0 | \hat{a}_p^\dagger \hat{a}_q | \Psi_\nu \rangle \quad (2.7)$$

is the transition density of the neutral excited state  $\Psi_\nu$ .

The level of theory used to construct the polarizability determines the energies  $\Omega_\nu$  and wavefunctions  $\Psi_\nu$  entering in the above equations. Using any time-dependent mean-field response,  $|\Psi_\nu\rangle = \sum_{ai} [X_{ai}^\nu a_a^\dagger a_i - Y_{ai}^\nu a_i^\dagger a_a] |\Psi_0\rangle$ , leads to an eigensystem commonly associated with the RPA,

$$\begin{pmatrix} \mathbf{A} & \mathbf{B} \\ -\mathbf{B}^* & -\mathbf{A}^* \end{pmatrix} \begin{pmatrix} \mathbf{X}^\nu \\ \mathbf{Y}^\nu \end{pmatrix} = \Omega_\nu \begin{pmatrix} \mathbf{X}^\nu \\ \mathbf{Y}^\nu \end{pmatrix}, \quad (2.8)$$

and transition amplitudes

$$M_{pq}^\nu = \sum_{ai} [X_{ai}^\nu \langle ip|aq\rangle + Y_{ai}^\nu \langle ap|i q\rangle], \quad (2.9)$$

where the two-electron integrals are given by  $\langle pq|rs\rangle \equiv \int d\mathbf{x}_1 d\mathbf{x}_2 \phi_p^*(\mathbf{x}_1) \phi_q^*(\mathbf{x}_2) r_{12}^{-1} \phi_r(\mathbf{x}_1) \phi_s(\mathbf{x}_2)$  and  $\mathbf{x}$  is a combined spin and spatial variable.

Specifically using time-dependent HF theory, the  $\mathbf{A}$  and  $\mathbf{B}$  matrices (each of dimension  $n_{\text{occ}} n_{\text{vir}} \times n_{\text{occ}} n_{\text{vir}}$ ) have elements

$$A_{ai,bj} = (\varepsilon_a - \varepsilon_i) \delta_{ab} \delta_{ij} + \langle aj||ib\rangle, \quad (2.10a)$$

$$B_{ai,bj} = \langle ij||ab\rangle. \quad (2.10b)$$

where the anti-symmetrized two-electron integrals are  $\langle pq||rs\rangle \equiv \langle pq|rs\rangle - \langle pq|sr\rangle$ . Using the more conventional time-dependent Hartree dielectric function yields the same structure, but ne-

glects the exchange integrals in the  $\mathbf{A}$  and  $\mathbf{B}$  matrices; this corresponds to the common version of the RPA and the one used in the  $GW$  approximation. The RPA eigenvalues come in positive- and negative-energy pairs, comprising only  $n_{\text{occ}}n_{\text{vir}}$  distinct eigenvalues; thus there are  $Mn_{\text{occ}}n_{\text{vir}}$  poles in the  $GW$  self-energy.

In the form given here, the solution of the RPA eigenvalue problem in Eq. (2.8) highlights the canonical  $N^6$  scaling of the  $GW$  approximation [103, 105], which is identical to that of EOM-CCSD. This  $GW$  scaling comes from the need to calculate *all* RPA eigenvalues in order to reliably calculate just one quasiparticle energy in Eq. (2.5). Alternative formulations can reduce this scaling.

### 2.2.3 Equation-of-motion coupled-cluster theory

Equation-of-motion coupled-cluster theories start from the ground-state CC wavefunction,  $|\Psi\rangle = e^{\hat{T}}|\Phi\rangle$ , where the cluster operator  $\hat{T}$  creates neutral excitations with respect to the reference determinant  $|\Phi\rangle$ ,

$$\hat{T} = \hat{T}_1 + \hat{T}_2 + \dots = \sum_{ai} t_i^a \hat{a}_a^\dagger \hat{a}_i + \frac{1}{4} \sum_{abij} t_{ij}^{ab} \hat{a}_a^\dagger \hat{a}_b^\dagger \hat{a}_j \hat{a}_i + \dots \quad (2.11)$$

The ground-state energy and cluster amplitudes are determined by the conditions

$$E_{CC} = \langle \Phi | \bar{H} | \Phi \rangle \quad (2.12a)$$

$$0 = \langle \Phi_i^a | \bar{H} | \Phi \rangle \quad (2.12b)$$

$$0 = \langle \Phi_{ij}^{ab} | \bar{H} | \Phi \rangle \quad (2.12c)$$

and so on, where  $|\Phi_i^a\rangle = \hat{a}_a^\dagger \hat{a}_i |\Phi\rangle$ , etc. and  $\bar{H} \equiv e^{-\hat{T}} \hat{H} e^{\hat{T}}$  is a similarity-transformed Hamiltonian. As seen above, the reference determinant is the right-hand eigenvector of  $\bar{H}$ . Because  $\bar{H}$  is non-Hermitian, it has distinct left-hand and right-hand eigenvectors for each eigenvalue; for the ground

state, the left-hand eigenvector of  $\hat{H}$  is given by

$$\langle \tilde{\Psi}_0 | = \langle \Phi | (1 + \hat{\Lambda}) e^{-\hat{T}}, \quad (2.13)$$

$$\hat{\Lambda} = \hat{\Lambda}_1 + \hat{\Lambda}_2 + \dots = \sum_{ai} \lambda_a^i \hat{a}_i^\dagger \hat{a}_a + \frac{1}{4} \sum_{abij} \lambda_{ab}^{ij} \hat{a}_i^\dagger \hat{a}_j^\dagger \hat{a}_b \hat{a}_a + \dots \quad (2.14)$$

Charged excitation energies in EOM-CC are calculated as eigenvalues of a  $\bar{H}$  in a finite basis of  $(N \pm 1)$ -electron Slater determinants;  $(N - 1)$ -electron excitation energies are calculated via the ionization potential (IP) framework and  $(N + 1)$ -electron excitation energies via the electron affinity (EA) framework [81, 82, 79, 80]. For example, the IP-EOM-CC energies are determined by

$$(E_{CC} - \bar{H}) \hat{R}^{N-1}(n) |\Phi\rangle = \Omega_n^{N-1} \hat{R}^{N-1}(n) |\Phi\rangle \quad (2.15)$$

$$\begin{aligned} \hat{R}^{N-1}(n) &= \hat{R}_1^{N-1}(n) + \hat{R}_2^{N-1}(n) + \dots \\ &= \sum_i r_i(n) \hat{a}_i + \frac{1}{2} \sum_{aij} r_{ij}^a(n) \hat{a}_a^\dagger \hat{a}_j \hat{a}_i + \dots \end{aligned} \quad (2.16)$$

where  $\Omega_n^{N-1} = E_0^N - E_n^{N-1}$  is the negative of a many-body ionization potential and corresponds to an exact pole of the one-particle Green's function. Again,  $\bar{H}$  has distinct left-hand eigenvectors,

$$\langle \Phi | \hat{L}^{N-1}(n) (E_{CC} - \bar{H}) = \langle \Phi | \hat{L}^{N-1}(n) \Omega_n^{N-1} \quad (2.17)$$

$$\begin{aligned} \hat{L}^{N-1}(n) &= \hat{L}_1^{N-1}(n) + \hat{L}_2^{N-1}(n) + \dots \\ &= \sum_a l^a(n) \hat{a}_a^\dagger + \frac{1}{2} \sum_{abi} l_i^{ab}(n) \hat{a}_a^\dagger \hat{a}_b^\dagger \hat{a}_i + \dots \end{aligned} \quad (2.18)$$

The left-hand and right-hand eigenstates of the untransformed  $\hat{H}$  are then given by

$$|\Psi_n^{N-1}\rangle = e^{\hat{T}} \hat{R}^{N-1}(n) |\Phi\rangle \quad (2.19)$$

$$\langle \tilde{\Psi}_n^{N-1} | = \langle \Phi | \hat{L}^{N-1}(n) e^{-\hat{T}} \quad (2.20)$$

and form a biorthogonal set. With appropriate normalization, the eigenstates yield a resolution-of-

the-identity in the  $(N \pm 1)$ -electron space

$$\begin{aligned}
1 &= \sum_n |\Psi_n^{N\pm 1}\rangle \langle \tilde{\Psi}_n^{N\pm 1}| \\
&= \sum_n e^{\hat{T}} \hat{R}^{N\pm 1}(n) |\Phi\rangle \langle \Phi| \hat{L}^{N\pm 1}(n) e^{-\hat{T}}.
\end{aligned} \tag{2.21}$$

As first done by Nooijen and Snijders [81, 82], this enables an algebraic Lehmann representation of the Green's function, which (as usual) separates into IP and EA contributions due to the time-ordering operator,  $G_{pq}(\omega) = G_{pq}^{\text{IP}}(\omega) + G_{pq}^{\text{EA}}(\omega)$ . For example, the IP part is given by

$$G_{pq}^{\text{IP}}(\omega) = \sum_n \frac{\tilde{\psi}_q(n) \psi_p(n)}{\omega - \Omega_n^{N-1} + i\eta}, \tag{2.22a}$$

$$\tilde{\psi}_q(n) = \langle \Phi | (1 + \hat{\Lambda}) e^{-\hat{T}} \hat{a}_q^\dagger e^{\hat{T}} \hat{R}^{N-1}(n) | \Phi \rangle, \tag{2.22b}$$

$$\psi_p(n) = \langle \Phi | \hat{L}^{N-1}(n) e^{-\hat{T}} \hat{a}_p e^{\hat{T}} | \Phi \rangle. \tag{2.22c}$$

Using conventional many-body techniques for the  $\hat{T}$ ,  $\hat{R}$ , and  $\hat{\Lambda}$  operators enables separate diagrammatic expansions of the IP and EA contributions to the Green's function [81, 82], which is properly size extensive as a sum of connected diagrams. In particular, using IP-EOM-CCSD, the IP Green's function is given as the sum over all time-ordered (Goldstone) diagrams for which cutting the diagram after each endpoint or vertex always leaves a sum of disconnected diagrams at previous times, each of which has no more than two electron and two hole open propagator lines. Based on the outcome of this procedure, components of each diagram can be classified as belonging to the cluster operators  $\hat{T}_n$ , the EOM operators  $\hat{R}_n$ , or the de-excitation operators  $\hat{\Lambda}_n$  (in Refs.[81, 82], these operators are designated more precisely as  $\hat{T}_n$ ,  $\hat{S}_n^{(p)}(\omega)$ , and  $\hat{R}_n^{(pq)}(\omega)$  respectively). Importantly in this construction, *at each order in perturbation theory, all time-orderings of a given Feynman diagram are not included.*

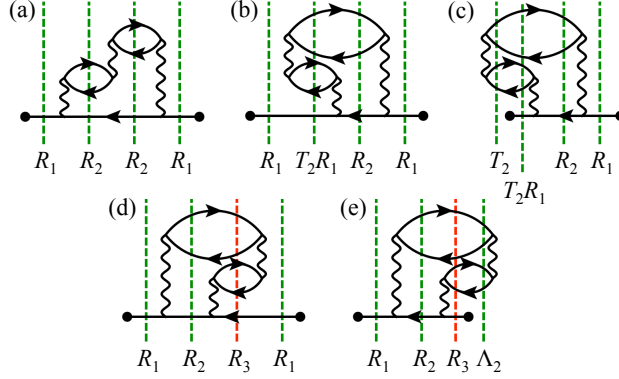


Figure 2.2: The only five third-order Goldstone diagrams contributing to  $G_{ij}^{\text{IP}}$  originating from  $\Sigma_{ij}(t_1, t_2)$  with  $t_1 < t_2$ , in the  $GW$  approximation. Only (a), (b), and (c) are included in the EOM-CCSD Green's function; all five are included in the EOM-CCSDT Green's function. Time increases from left to right.

## 2.3 Comparing the $GW$ approximation and EOM-CC theory

### 2.3.1 Comparing the Green's function

We first compare the time-ordered Goldstone diagrams appearing in the Green's function of the  $GW$  approximation and EOM-CC theory. By construction, the first-order terms in the Green's function are vanishing. At second order, there are ten Feynman diagrams arising from six diagrams for the proper self-energy, only two of which are not accounted for by a self-consistent HF calculation. The  $GW$  Green's function includes only one of these two diagrams, with a single ring, which translates to  $4! = 24$  Goldstone diagrams, *all of which* are included in the EOM-CCSD Green's function. However, the EOM-CCSD Green's function also includes all Goldstone diagrams associated with the second-order exchange diagram (another 24 Goldstone diagrams). Therefore, as is well known, the EOM-CCSD Green's function is correct through second order, and thus exact for two-electron problems; the  $GW$  Green's function is not.

At third order, the comparison is more complicated. Again, the  $GW$  Green's function contains one irreducible Feynman diagram, which includes two rings leading to  $5! = 120$  Goldstone diagrams. For simplicity of analysis, we focus on IP diagrams ( $t_1 < t_2$ ) in the occupied orbital subspace,  $G_{ij}^{\text{IP}}(t_1, t_2)$ , generated by the hole part of the self-energy, i.e.  $\Sigma_{ij}(t_1, t_2)$  with  $t_1 < t_2$ .

The  $GW$  approximation produces five such Goldstone diagrams, *only three of which* are included in the EOM-CCSD Green's function. When cut after the second interaction, diagrams (d) and (e) produce, at earlier times, a connected diagram in the 3-hole+2-particle (3h2p) space, which is included in the EOM-CCSDT Green's function, but not the EOM-CCSD one. In contrast, diagrams (b) and (c) also have a 3h2p configuration, but one that is generated by the disconnected product of the  $T_2$  [2-hole+2-particle (2h2p)] and  $R_1$  [1-hole (1h)] operators. Therefore, *some of the non-TDA  $GW$  diagrams are included in the EOM-CCSD Green's function, but not all of them.*

The above analysis is straightforward to generalize to higher order, and we find that the irreducible part of the EOM-CCSD Green's function at  $n$ th order contains only a vanishing fraction of the ring diagrams included in the  $GW$  Green's function; at  $n$ th order, the fraction of diagrams included is  $O(1/n)$ . (Of course, a large number of *reducible* Green's function diagrams are included at  $n$ th order, due to combinations of low-order diagrams.) In spite of this apparent flaw of EOM-CCSD theory, we emphasize that the EOM-CCSD Green's function contains many other non-ring diagrams that are not contained in the  $GW$  approximation. For example, three third-order diagrams corresponding to various particle-particle and particle-hole ladders are shown in Fig. 2.3. Diagrams (a) and (c) include vertex corrections to the self-energy and diagram (b) includes a vertex correction to the polarization propagator.

The behavior we have described should be compared to the enumeration of Goldstone diagrams for the correlation energy (the vacuum amplitude): in this context, ground-state CCSD includes ring diagrams with *all possible time orderings*, completely encompassing those diagrams contained

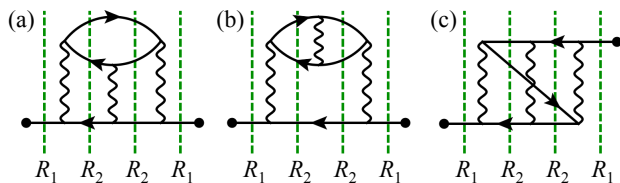


Figure 2.3: Three example third-order Goldstone diagrams contributing to the IP part of the EOM-CCSD Green's function with  $t_1 < t_2$ , which are not included in the  $GW$  Green's function. All diagrams shown are generated by the EOM (2h1p) formalism, independent of coupled-cluster theory. Time increases from left to right.

in the RPA [64, 66]. Similarly, one of us (T.C.B.) has recently shown that the frequency-dependent polarizability calculated with neutral-excitation EOM-CCSD encompasses all diagrams contained in the (dynamical) RPA [106, 107]. The difference observed here for the one-particle Green’s function can be traced to the need for the EOM-CC operators to simultaneously describe screening and free-particle propagation, as exemplified in diagrams (d) and (e) in Fig. 2.2. For exactly this reason, the CCSD correlation energy *is not recovered* from the EOM-CCSD Green’s function, as discussed by Nooijen and Snijders [82],

$$E_{\text{CCSD}} \neq \frac{1}{4\pi i} \int d\omega \text{Tr} \{ (\mathbf{h} + \omega \mathbf{1}) \mathbf{G}_{\text{CCSD}}^{\text{IP}}(\omega) \}. \quad (2.23)$$

Because of Eq. (2.23), there is no EOM-ring-CCD Green’s function that produces the RPA correlation energy. The above can roughly be viewed as a reminder that although the CCSD energy is exact to third order in perturbation theory, the EOM-CCSD energies are only exact to second order. However, the EOM-CCSD Green’s function does yield the CCSD reduced density matrix and is thus properly number-conserving,

$$\rho_{\text{CCSD}} = \frac{1}{2\pi i} \int d\omega [\mathbf{G}_{\text{CCSD}}^{\text{IP}}(\omega)] \quad (2.24)$$

$$N = \text{Tr} \{ \rho_{\text{CCSD}} \}. \quad (2.25)$$

Therefore, despite the error in the individual poles of the EOM-CCSD Green’s function, some “sum rules” are satisfied.

In this section, we have compared the Green’s functions generated by EOM-CC and the *GW* approximation. A more direct connection with the *GW* approximation and related time-dependent diagrammatic methods can be made by directly targeting an EOM-CC self-energy or polarization propagator; work along these lines is currently in progress in our group. However, an *approximate* algebraic self-energy can be worked out directly from the EOM-CC eigenvalue problem, which we turn to next.

### 2.3.2 Comparing the self-energy

For the remainder of the article, we will only consider IP-EOM-CCSD; the results for EA-EOM-CCSD are completely analogous. We introduce the normal-ordered Hamiltonian, with respect to the HF reference,  $\hat{H}_N \equiv \hat{H} - E_{\text{HF}}$  and its similarity-transformed variant  $\bar{H}_N \equiv \bar{H} - E_{\text{CC}}$ . The linear eigenvalue problem in Eqs. (2.15) and (2.16) clearly leads to a (schematic) matrix representation

$$\Delta\bar{\mathbf{H}}_{\text{CC}} = - \begin{pmatrix} \langle \Phi_i | \bar{H}_N | \Phi_k \rangle & \langle \Phi_i | \bar{H}_N | \Phi_{kl}^b \rangle \\ \langle \Phi_{ij}^a | \bar{H}_N | \Phi_k \rangle & \langle \Phi_{ij}^a | \bar{H}_N | \Phi_{kl}^b \rangle \end{pmatrix}; \quad (2.26)$$

In this section, we will show that the *GW* excitation energies are closely related to the eigenvalues of the approximated matrix

$$\Delta\bar{\mathbf{H}}_{\text{CCGW}} = - \begin{pmatrix} \langle \Phi_i | e^{-\hat{T}_2} \hat{f}_N e^{\hat{T}_2} | \Phi_k \rangle & \langle \Phi_i | \bar{H}_N | \Phi_{kl}^b \rangle \\ \langle \Phi_{ij}^a | \bar{H}_N | \Phi_k \rangle & \langle \Phi_{ij}^a | H_N | \Phi_{kl}^b \rangle \end{pmatrix}, \quad (2.27)$$

where  $\hat{f}_N$  is the normal-ordered Fock operator,  $\hat{T}_1 = 0$  everywhere, the  $\hat{T}_2$  amplitudes satisfy an approximate version of Eq. (2.12c) known as “ring-CCD” [64, 66], and the untransformed Hamiltonian ( $\hat{T}_2 = 0$ ) is used in the doubles-doubles block.

If desired, antisymmetrization can further be removed from most two-electron integrals leading to the use of “direct ring-CCD” [64, 66] in the one-hole space combined with a more conventional TDH treatment of screening in the two-hole+one-particle. However, we keep antisymmetrization throughout, which makes the theory manifestly self-interaction free, while retaining only the essential ingredients of the *GW* approximation.

Using a Löwdin partitioning [108], the eigenvalues of the Hamiltonian in Eq. (2.27) can be

found self-consistently for the frequency-dependent matrix

$$\begin{aligned}
A_{ij}(\omega) &= -\langle \Phi_i | e^{-\hat{T}_2} \hat{f}_N e^{\hat{T}_2} | \Phi_j \rangle \\
&\quad + \frac{1}{4} \sum_{abklmn} \langle \Phi_i | \bar{H} | \Phi_{kl}^a \rangle [G_{2h1p}]_{klmn}^{ab}(\omega) \langle \Phi_{mn}^b | \bar{H} | \Phi_j \rangle \\
&= \varepsilon_i \delta_{ij} + \tilde{\Sigma}_{ij}^p + \tilde{\Sigma}_{ij}^h(\omega)
\end{aligned} \tag{2.28}$$

where  $G_{2h1p}(\omega)$  is a specific time-sequence of the three-particle Green's function,

$$\begin{aligned}
[G_{2h1p}]_{klmn}^{ab}(\omega) &= -i \int dt e^{i\omega t} \langle \Phi_0 | [\hat{a}_a^\dagger \hat{a}_k \hat{a}_l](0) [\hat{a}_b^\dagger \hat{a}_m \hat{a}_n](t) | \Phi_0 \rangle \\
&= \langle \Phi_0 | \hat{a}_a^\dagger \hat{a}_k \hat{a}_l \frac{1}{\omega - (-\mathcal{P} \hat{H}_N \mathcal{P})} \hat{a}_b^\dagger \hat{a}_m \hat{a}_n | \Phi_0 \rangle;
\end{aligned} \tag{2.29}$$

this Green's function describes propagation in the 2h1p subspace generated by the projection operator  $\mathcal{P}$ . The self-consistent eigenvalue problem defined in Eq. (2.28) is analogous to that of the *GW* approximation defined in Eqs. (2.3) and (2.5). There are two significant differences that originate from the treatment of time-ordering in EOM-CC theory. First, the particle contribution to the self-energy of the IP part of the Green's function  $\tilde{\Sigma}_{ij}^p$  is frequency-independent; analogously, in EA-EOM-CC, the hole contribution to the self-energy of the EA part of the Green's function is frequency-independent. However, as discussed above, the frequency dependence of these terms – when calculating the respective excitation energy – is typically very weak. Second, the effective self-energy in IP-EOM-CC (resp. EA-EOM-CC) only has matrix elements in the occupied (virtual) orbital space; this is in contrast to the self-energy in any proper diagrammatic theory, which has matrix elements in the entire orbital space. We emphasize that neither of these differences reflects an approximation, but only a difference in formalism; diagrammatically-defined self-energy theories and EOM-CC can both be made exact in their appropriate limits, while retaining their respective (different) mathematical structures.

To summarize the structure of this effective “self-energy” from an EOM-CC-based theory: for the IPs, the forward time-ordered self-energy (the hole contribution) arises from coupling between 1h and 2h1p configurations, whereas the reverse time-ordered self-energy (the particle contribu-

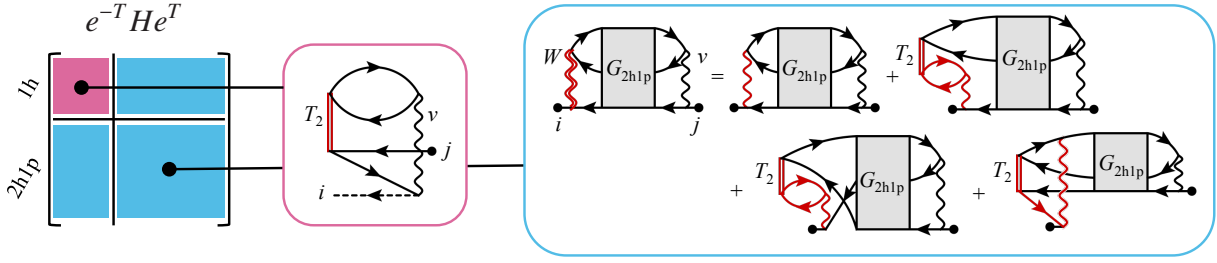


Figure 2.4: Goldstone self-energy diagrams arising from the different sectors of the IP-EOM-CCSD similarity-transformed Hamiltonian. The  $\hat{T}_2$ -transformed Fock operator in the 1h space generates a frequency-independent screened-exchange self-energy  $\tilde{\Sigma}_{ij}^p$ . The  $\hat{T}_2$ -transformed repulsion integral  $W_{iakl}$ , which couples the 1h and 2h1p spaces, generates non-Tamm-Dancoff screening on top of the Tamm-Dancoff ring and ladder diagrams generated in the 2h1p space; this leads to a frequency-dependent screened-exchange self-energy  $\tilde{\Sigma}_{ij}^h(\omega)$ .

tion) arises from the similarity transformation of the Fock operator in the 1h subspace; this behavior is shown schematically in Fig. 2.4. In the  $GW$  language, both of these effects can be viewed as giving rise to screening of the quasiparticle excitations. From this point of view, we observe that the IP-EOM-CISD methodology [109], obtained by setting  $\hat{T}_1 = \hat{T}_2 = 0$  in IP-EOM-CCSD, only includes one of the two time orderings, each diagram of which is fully forward-time-ordered in the TDA sense. Finally, we note that the *true* CCSD self-energy can be straightforwardly obtained numerically, by calculating both the IP and EA Green's functions and using Dyson's equation,

$$\Sigma_{pq}(\omega) = (\omega - \varepsilon_p)\delta_{pq} - [\mathbf{G}^{\text{IP}}(\omega) + \mathbf{G}^{\text{EA}}(\omega)]_{pq}^{-1}. \quad (2.30)$$

Naturally, the frequency-dependent matrix  $\omega - \mathbf{f} - \Sigma(\omega)$  will have eigenvalues given exactly by the IP/EA-EOM-CCSD excitation energies, as well as the proper analytical (frequency-dependent) structure.

We now proceed to make the comparison between the approximate IP-EOM-CCSD of Eq. (2.27) and the  $GW$  approximation more explicit. First, we consider the frequency-dependent hole contribution  $\Sigma_{ij}^h(\omega)$ . The 2h1p Green's function can be expressed in two ways: first, as a perturbative

series that can be translated into diagrams,

$$[G_{2\text{h1p}}]_{klmn}^{ab}(\omega) = \sum_{p=0}^{\infty} \langle \Phi_{kl}^a | \hat{R}_0(\omega) [\mathcal{P} \hat{V}_N \hat{R}_0(\omega)]^p | \Phi_{mn}^b \rangle \quad (2.31)$$

where  $\hat{R}_0(\omega) = [\omega - (-\hat{f}_N)]^{-1}$  is the resolvent of the Fock operator and  $\hat{V}_N = \hat{H}_N - \hat{f}_N$  is the normal-ordered fluctuation operator. Alternatively,  $G_{2\text{h1p}}$  can be expressed in terms of the solutions of an eigenproblem,

$$[G_{2\text{h1p}}]_{klmn}^{ab}(\omega) = \sum_{\nu} \frac{r_{kl}^a(\nu) [r_{mn}^b(\nu)]^*}{\omega - E_{\nu}^{2\text{h1p}}} \quad (2.32)$$

where  $E_{\nu}^{2\text{h1p}}$  is an eigenvalue of the 2h1p block of the Hamiltonian  $\langle \Phi_{kl}^a | (-\tilde{H}_N) | \Phi_{mn}^b \rangle$  with eigenvector  $|\nu\rangle = \frac{1}{2} \sum_{akl} r_{kl}^a(\nu) | \Phi_{kl}^a \rangle$ . Notably, the set of diagrams contained in  $G_{2\text{h1p}}$  is identically those included in the two-particle-hole TDA theory of the self-energy [71], mentioned in the introduction. The CC self-energy goes beyond the TDA diagrams via the outer vertices, i.e. the matrix elements of the similarity-transformed Hamiltonian, which can be evaluated to give

$$\begin{aligned} \langle \Phi_i | \tilde{H} | \Phi_{kl}^a \rangle &= W_{iakl} = \langle ia || kl \rangle + \sum_{me} \langle im || ke \rangle t_{lm}^{ae}, \\ &- \sum_{me} \langle im || le \rangle t_{km}^{ae} + \frac{1}{2} \sum_{ef} \langle ia || ef \rangle t_{kl}^{ef} \end{aligned} \quad (2.33a)$$

$$\langle \Phi_{mn}^b | \tilde{H} | \Phi_j \rangle = \langle mn || jb \rangle, \quad (2.33b)$$

leading to the self-energy

$$\tilde{\Sigma}_{ij}^{\text{h}}(\omega) = \frac{1}{4} \sum_{abklmn} W_{iakl} [G_{2\text{h1p}}]_{klmn}^{ab}(\omega) \langle mn || jb \rangle. \quad (2.34)$$

Viewing  $W$  as a screened Coulomb interaction leads to the set of diagrams shown in Fig. 2.4. The construction of the intermediate  $W$  has a non-iterative  $N^6$  cost, which is usually swamped by the iterative  $N^5$  cost of subsequent matrix-vector multiplies during Davidson diagonalization.

The use of exact CCSD amplitudes in Eq. (2.33a) includes many beyond- $GW$  insertions in the

polarization propagator. However, as discussed, the closest comparison can be made when the  $\hat{T}_2$  amplitudes solve the approximate ring-CCD equations,

$$\begin{aligned}
t_{ij}^{ab}(\varepsilon_i + \varepsilon_j - \varepsilon_a - \varepsilon_b) &= \langle ab || ij \rangle \\
&+ \sum_{ck} t_{ik}^{ac} \langle kb || cj \rangle + \sum_{ck} \langle ak || ic \rangle t_{kj}^{cb} + \sum_{cdkl} t_{ik}^{ac} \langle kl || cd \rangle t_{lj}^{db}.
\end{aligned} \tag{2.35}$$

Iteration of these equations adds higher-order non-TDA ring diagrams in the self-energy, very much like in the  $GW$  approximation. However, consistent with the analysis presented in Sec. 2.3.1, *the non-TDA diagrams are generated in an asymmetric and incomplete manner.*

Beyond this issue of non-TDA diagrams on the later-time side of the self-energy, the approximation described so far has three additional qualitative differences from the  $GW$  approximation. First, the presence of antisymmetrized vertices generates many exchange diagrams not included in the conventional  $GW$  approximation. In particular, the “exterior” antisymmetrization is responsible for some of the self-energy diagrams that are in the second-order screened exchange (SOSEX) approach [110] and “interior” antisymmetrization yields particle-hole ladders that improve the quality of the polarization propagator. Second, the 2h1p Green’s function includes the interaction between two holes in the intermediate 2h1p state, leading to hole-hole ladder insertions, which are vertex corrections beyond the structure of the  $GW$  self-energy. Third, the final term in Eq. (2.33a) can be shown to produce mixed ring-ladder diagrams that are not included at the  $GW$  or SOSEX levels of theory.

Finally, we consider the frequency-independent particle contribution to the self-energy. In IP-EOM-CCD, this term is given by

$$\tilde{\Sigma}_{ij}^p = \frac{1}{2} \sum_{kab} \langle ik || ab \rangle t_{kj}^{ba}, \tag{2.36}$$

which can be represented by the single diagram shown in Fig. 2.4. This diagram must be evaluated as a scalar without frequency dependence according to the usual diagrammatic rules of time-independent perturbation theory [63]. With this interpretation, the iteration of the ring-CCSD

equations again generates all TDA-screening diagrams plus an asymmetric subset of non-TDA screening diagrams. Antisymmetrization is responsible for subsets of both  $GW$  and SOSEX diagrams.

## 2.4 Application of EOM-CCSD to the $GW100$ test set

Having established the formal relation between EOM-CCSD and the  $GW$  approximation, we now present a numerical comparison. In particular, we will study the so-called  $GW100$  test set [94], comprising 100 small- to medium-sized molecules with up to 66 active electrons in 400 spatial orbitals. The  $GW100$  test set was introduced by van Setten and co-authors [94] in order to provide a simple and controlled class of problems with which to compare theoretical and computational approximations of  $GW$ -based implementations. This important research agenda aims to enforce reproducibility within the community and highlight the successes and limitations of the aforementioned time-dependent diagrammatic techniques, thereby identifying avenues for future research. The  $GW100$  has been studied by a number of different groups [94, 92, 93, 111, 112].

In addition to providing results and analysis for conventional IP- and EA-EOM-CCSD excitation energies, we will also consider a number of approximations. These approximations make the computational cost more competitive with that of the  $GW$  approximation and – in light of the previous sections – many of them can be understood as selective inclusion of certain diagrams. These approximations are described in the next section. Some of these approximations have been investigated and compared for charged excitations [113, 114, 46] and for neutral electronic excitations [45, 115].

### 2.4.1 Approximations to EOM-CCSD

As mentioned previously, in their canonical forms, the  $GW$  approximation and the IP/EA-EOM-CCSD formalism both scale as  $N^6$ . For the latter class of methods, this scaling originates from the solution of the ground-state CCSD equations, while the subsequent ionized EOM eigenvalue problem exhibits only  $N^5$  scaling (with relatively cheap, non-iterative  $N^6$  steps associated

with construction of the intermediates). For this reason, a natural target for approximations leading to reduced cost is the ground-state calculation. Despite the distinction we draw between ground-state and excited-state approximations, we note that the results of the previous section have shown that the determination of the  $T$ -amplitudes via ground-state CCSD directly affects the diagrams contributing to the one-particle Green's function.

*MBPT2 ground state.* The most severe approximation to the ground state is that of second-order many-body perturbation theory (MBPT2). For a canonical Hartree-Fock reference, which we use throughout this work, this is equivalent to second-order Møller-Plesset perturbation theory (MP2). In this approach,  $\hat{T}_1 = 0$  and the  $\hat{T}_2$  amplitudes are approximated by

$$t_{ij}^{ab} \approx \frac{\langle ab||ij \rangle}{\varepsilon_i + \varepsilon_j - \varepsilon_a - \varepsilon_b}. \quad (2.37)$$

Due to the transformation from atomic orbitals to molecular orbitals, an MBPT2 calculation scales as  $N^5$  and so the use of MBPT2 amplitudes in an IP/EA-EOM calculation leads to overall  $N^5$  methods for ionization potentials and electron affinities. Following Refs.[116, 117, 45], we call this method EOM-MBPT2; the same method has also been referred to as EOM-CCSD(2) [118].

*CC2 ground state.* A popular approximation to reduce the cost of CCSD is the CC2 model [119]. In this technique, the  $\hat{T}_1$  amplitude equations are unchanged from those of CCSD, while the  $\hat{T}_2$  amplitude equations (2.12c) are changed such that  $\hat{T}_2$  only connects to the Fock operator

$$0 = \langle \Phi_{ij}^{ab} | e^{-\hat{T}_1} \hat{H}_N e^{\hat{T}_1} + e^{-\hat{T}_2} \hat{f}_N e^{\hat{T}_2} | \Phi \rangle. \quad (2.38)$$

This leads to approximate  $\hat{T}_2$  amplitudes that are very similar to those of MBPT2,

$$t_{ij}^{ab} \approx \frac{\overline{\langle ab||ij \rangle}}{\varepsilon_i + \varepsilon_j - \varepsilon_a - \varepsilon_b}, \quad (2.39)$$

where  $\overline{\langle ab||ij \rangle} \equiv \langle \Phi_{ij}^{ab} | e^{-\hat{T}_1} \hat{H}_N e^{\hat{T}_1} | \Phi \rangle$  are  $\hat{T}_1$ -transformed two-electron integrals. Like MBPT2, the CC2 approximation removes the  $\hat{T}_2$  contractions responsible for  $N^6$  scaling and is thus an iterative

$N^5$  technique. While CC2 treats dynamical correlation at essentially the same level as MBPT2, the full treatment of single excitations generated by  $\hat{T}_1$  allows orbital relaxation, which should be beneficial in cases where the HF determinant is suboptimal.

*Linearized CCSD.* The final ground-state approximation that we consider is linearized CCSD (linCCSD) [120], which is the least severe approximation to CCSD. In this approach, all quadratic products of the CCSD amplitudes are neglected in the amplitude equations. In diagrammatic language, this approximation neglects many – *but not all* – of the non-TDA diagrams in the Green’s function; for example, the third-order non-TDA diagrams shown in Fig. 2.2(b) and (c) are included even when the amplitude equations are linearized. The non-TDA time-ordering is a result of the combination of  $\hat{R}_1$  and  $\hat{T}_2$ , rather than of nonlinear terms in the  $\hat{T}_2$  equations. Although linearized CCSD still scales as  $N^6$ , the method is more amenable to parallelization [120], which may be desirable for large systems or solids [2, 100, 1, 13].

*Excited state approximation.* After the ground-state calculation, the most expensive contribution to an EOM-CCSD calculation comes from the large doubles-doubles block of the similarity-transformed Hamiltonian. A natural approximation then is to replace the doubles-doubles block by simple orbital-energy differences,

$$\langle \Phi_{ij}^a | \bar{H}_N | \Phi_{kl}^b \rangle \approx (\varepsilon_a - \varepsilon_i - \varepsilon_j) \delta_{ab} \delta_{ik} \delta_{jl}, \quad (2.40)$$

leading to a diagonal structure and a straightforward Löwdin partitioning. Naturally, this approach is only reasonable for principle charged excitations with a large weight in the singles (one-hole or one-particle) sector.

This partitioned variant of EOM-CCSD theory still exhibits  $N^5$  scaling after the  $\hat{T}$ -amplitudes are determined, but requires the construction and storage of far fewer integral intermediates. Formally, this approximate partitioning technique can be combined with any treatment of the ground-state CC equations, though it only makes practical sense for approximate ground-state calculations whose cost does not overwhelm that of the EOM calculation. We will combine the approxi-

mate partitioning technique with MBPT2 and CC2 ground states, denoting the results as P-EOM-MBPT2 and P-EOM-CC2, respectively.

As first discussed in Ref.[116], the P-EOM-MBPT2 method is formally very close to the non-self-consistent second-order Green’s function technique (GF2), where the self-energy is composed of second-order ring and exchange diagrams [75, 121]. When applied exactly as described, P-EOM-MBPT2 actually includes a few third-order self-energy diagrams – as can be seen in Fig. 2.4. These can be removed by also neglecting the  $\hat{T}$ -amplitudes in the screened Coulomb interaction  $W_{iakl}$  that couples the 1h and 2h1p space, given in Eq. (2.33a). However, this additional ground-state correlation is found to be responsible for a remarkable improvement in the accuracy of P-EOM-MBPT2 when compared to GF2.

With respect to the hierarchy of linear-response CC2 methods described in Ref.[122], the EOM-CC2 method described here is equivalent to IP-CCSD[f]<sub>CC2</sub> and the P-EOM-CC2 method is between IP-CCSD[0]<sub>CC2</sub> and IP-CCSD[1]<sub>CC2</sub>.

#### 2.4.2 Numerical details

We have applied the above methods to calculate the first few principle ionization potentials and electron affinities for the molecules in the *GW*100 test set. Followings Refs.[92, 93], we work in the localized-orbital def2-TZVPP basis set [123], using corresponding pseudopotentials for elements in the fifth and sixth row of the periodic table; core orbitals were frozen in all calculations. While this choice of basis is a good trade-off between cost and accuracy, our results are not converged with respect to the basis set and should not be compared directly to experiment or to calculations in other basis sets, such as plane-wave based *GW* calculations [111, 112]. Instead, these calculations can be directly compared to preexisting ionization potentials in the same basis [92, 93]. More importantly, our calculations are internally consistent; the main purpose of this section is to benchmark the accuracy of cost-saving approximations to EOM-CCSD and demonstrate the utility of EOM-CCSD techniques for excited-state properties of benchmark data sets. Extrapolation to the complete basis set limit and comparison with other non-CC techniques is reserved for

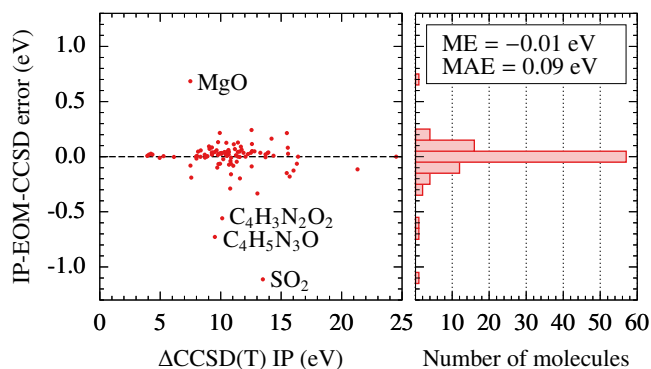


Figure 2.5: Comparison of ionization potentials predicted by IP-EOM-CCSD compared to those predicted by  $\Delta$ CCSD(T) from Ref.[92]. Errors with respect to the latter are presented as a scatter plot (left) and histogram (right). Four molecules with errors exceeding 0.5 eV are explicitly labeled.

future work.

An advantage of the IP/EA-EOM-CCSD approaches is an avoidance of open-shell calculations for charged molecules. As such, all of our calculations were performed using a spin-free implementation based on a closed-shell restricted HF reference, and free of spin contamination. All calculations were performed using the PySCF software package [124].

Recent work [111] has identified two molecules from the original *GW*100 test set with incorrect geometries: vinyl bromide and phenol. For consistency with previously published results, we have performed calculations on the original geometries.

### 2.4.3 Comparison to $\Delta$ CCSD(T) ionization potentials

We first aim to establish the accuracy of EOM-CCSD for the *GW*100 test set. As a ground-state theory, CCSD with perturbative triples [CCSD(T)] represents the ‘gold standard’ for weakly-correlated medium-sized molecules [125] and scales as  $N^7$ , which is more expensive than any method considered here. At this high level of theory, the first IP of each molecule has been calculated by Krause et al. [92], as a difference in ground-state energies between neutral and charged molecules – the so-called  $\Delta$ CCSD(T) scheme. Higher-energy IPs and EAs, in particular those with the same symmetry as the first, cannot be calculated using this approach

In Fig. 2.5, we show the comparison between IPs predicted by  $\Delta$ CCSD(T) and IP-EOM-CCSD.

The IP-EOM-CCSD values exhibit a signed mean error (ME) of  $-0.01$  eV and a mean absolute error (MAE) of  $0.09$  eV. The small mean error indicates that the errors are not systematic. Only four molecules, identified in Fig. 2.5 have errors larger than  $0.5$  eV, suggesting that IP-EOM-CCSD represents a good approximation to  $\Delta$ CCSD(T), at least for the molecules included in the *GW100*. The most fair comparison, based on diagrams generated, is to the  $G_0W_0$  approximation based on a HF reference ( $G_0W_0@HF$ ). As reported by Caruso et al. [93], such an approach overestimates IPs, leading to a ME of  $0.26$  eV and a MAE of  $0.35$  eV. Interestingly, this is significantly better than the more popular (at least in the solid state)  $G_0W_0$  approximation based on a PBE starting point ( $G_0W_0@PBE$ ), which severely and systematically underestimates IPs, leading to a ME of  $-0.69$  eV and a MAE of  $0.69$  eV [93].

#### 2.4.4 Electron affinities and higher-energy excitations

By construction, EOM-CCSD can straightforwardly predict higher-energy ionization potentials, corresponding to more deeply-bound electrons, as well as the first and higher electron affinities. In order to provide a larger set of benchmark data for the *GW* community, in Tab. 2.1 we report the first three occupied and unoccupied quasiparticle energies (i.e. the negative of the first three IPs and EAs with large quasiparticle weights) for each molecule in the *GW100* test set, as calculated by IP- and EA-EOM-CCSD, and accounting for their multiplicities.

Formula	Name	HOMO-2	HOMO-1	HOMO	LUMO	LUMO+1	LUMO+2
He	helium			$-24.51$ ( $\times 1$ )	$22.22$ ( $\times 1$ )	$39.82$ ( $\times 3$ )	$166.90$ ( $\times 1$ )
Ne	neon	$-48.33$ ( $\times 1$ )	$-21.21$ ( $\times 3$ )		$20.84$ ( $\times 1$ )	$21.87$ ( $\times 2$ )	$74.27$ ( $\times 3$ )
Ar	argon	$-29.58$ ( $\times 1$ )	$-15.63$ ( $\times 2$ )		$14.73$ ( $\times 3$ )	$17.19$ ( $\times 4$ )	$20.69$ ( $\times 1$ )
Kr	krypton	$-27.14$ ( $\times 1$ )	$-13.98$ ( $\times 3$ )		$10.41$ ( $\times 2$ )	$12.24$ ( $\times 4$ )	$18.78$ ( $\times 1$ )
Xe	xenon	$-23.67$ ( $\times 1$ )	$-12.23$ ( $\times 3$ )		$7.72$ ( $\times 3$ )	$8.91$ ( $\times 3$ )	$12.29$ ( $\times 1$ )
H <sub>2</sub>	hydrogen			$-16.40$ ( $\times 1$ )	$4.22$ ( $\times 1$ )	$8.05$ ( $\times 1$ )	$16.04$ ( $\times 1$ )
Li <sub>2</sub>	lithium dimer	$-63.39$ ( $\times 1$ )	$-63.38$ ( $\times 1$ )	$-5.27$ ( $\times 1$ )	$-0.12$ ( $\times 1$ )	$0.99$ ( $\times 2$ )	$1.00$ ( $\times 1$ )
Na <sub>2</sub>	sodium dimer	$-37.24$ ( $\times 2$ )	$-37.21$ ( $\times 1$ )	$-4.94$ ( $\times 1$ )	$-0.26$ ( $\times 1$ )	$0.60$ ( $\times 2$ )	$0.78$ ( $\times 1$ )
Na <sub>4</sub>	sodium tetramer	$-36.60$ ( $\times 1$ )	$-5.59$ ( $\times 1$ )	$-4.25$ ( $\times 1$ )	$-0.53$ ( $\times 1$ )	$-0.10$ ( $\times 1$ )	$0.10$ ( $\times 1$ )
Na <sub>6</sub>	sodium hexamer	$-36.52$ ( $\times 1$ )	$-5.68$ ( $\times 1$ )	$-4.37$ ( $\times 2$ )	$-0.49$ ( $\times 1$ )	$-0.34$ ( $\times 2$ )	$-0.07$ ( $\times 1$ )
K <sub>2</sub>	potassium dimer	$-23.83$ ( $\times 2$ )	$-23.77$ ( $\times 1$ )	$-4.08$ ( $\times 1$ )	$-0.32$ ( $\times 1$ )	$0.77$ ( $\times 1$ )	$0.83$ ( $\times 2$ )
Rb <sub>2</sub>	rubidium dimer	$-20.09$ ( $\times 2$ )	$-20.02$ ( $\times 1$ )	$-3.93$ ( $\times 1$ )	$-0.37$ ( $\times 1$ )	$0.18$ ( $\times 1$ )	$0.35$ ( $\times 1$ )

N <sub>2</sub>	nitrogen	-18.84 (×1)	-17.21 (×1)	-15.60 (×1)	3.05 (×2)	8.97 (×1)	9.47 (×1)
P <sub>2</sub>	phosphorus dimer	-14.79 (×1)	-10.75 (×1)	-10.59 (×1)	-0.10 (×2)	3.47 (×1)	6.30 (×1)
As <sub>2</sub>	arsenic dimer	-14.64 (×1)	-10.14 (×1)	-9.91 (×2)	-0.26 (×1)	3.31 (×1)	6.88 (×1)
F <sub>2</sub>	fluorine	-21.09 (×1)	-18.85 (×1)	-15.53 (×1)	0.39 (×1)	15.34 (×1)	15.34 (×1)
Cl <sub>2</sub>	chlorine	-15.98 (×1)	-14.41 (×1)	-11.46 (×2)	-0.19 (×1)	9.10 (×1)	10.03 (×1)
Br <sub>2</sub>	bromine	-14.44 (×1)	-12.89 (×1)	-10.54 (×1)	-0.94 (×1)	7.05 (×1)	7.09 (×1)
I <sub>2</sub>	iodine	-12.76 (×1)	-11.38 (×2)	-9.55 (×2)	-1.50 (×1)	5.10 (×1)	5.15 (×1)
CH <sub>4</sub>	methane		-23.38 (×1)	-14.38 (×3)	3.45 (×1)	5.79 (×3)	7.88 (×3)
C <sub>2</sub> H <sub>6</sub>	ethane	-13.05 (×1)	-12.71 (×1)	-12.71 (×1)	3.11 (×1)	4.21 (×1)	5.24 (×2)
C <sub>3</sub> H <sub>8</sub>	propane	-12.25 (×1)	-12.12 (×1)	-12.05 (×1)	2.95 (×1)	4.13 (×1)	4.32 (×1)
C <sub>4</sub> H <sub>10</sub>	butane	-11.92 (×1)	-11.81 (×1)	-11.56 (×1)	2.88 (×1)	3.46 (×1)	4.12 (×1)
C <sub>2</sub> H <sub>4</sub>	ethylene	-14.91 (×1)	-13.11 (×1)	-10.69 (×1)	2.63 (×1)	3.94 (×1)	4.60 (×1)
C <sub>2</sub> H <sub>2</sub>	ethyne	-19.13 (×1)	-17.23 (×1)	-11.55 (×2)	3.50 (×2)	3.58 (×1)	4.53 (×1)
C <sub>4</sub>	tetracarbon	-14.65 (×1)	-11.46 (×1)	-11.27 (×1)	-2.36 (×1)	-0.01 (×1)	1.71 (×1)
C <sub>3</sub> H <sub>6</sub>	cyclopropane	-13.14 (×1)	-10.86 (×1)	-10.85 (×1)	3.46 (×1)	3.96 (×1)	4.10 (×1)
C <sub>6</sub> H <sub>6</sub>	benzene	-12.14 (×2)	-9.32 (×1)	-9.32 (×1)	1.78 (×2)	3.11 (×1)	4.00 (×2)
C <sub>8</sub> H <sub>8</sub>	cyclooctatetraene	-10.01 (×1)	-10.00 (×1)	-8.40 (×1)	0.79 (×1)	2.52 (×1)	2.54 (×1)
C <sub>5</sub> H <sub>6</sub>	cyclopentadiene	-12.52 (×1)	-11.03 (×1)	-8.69 (×1)	1.77 (×1)	3.27 (×1)	4.06 (×1)
C <sub>2</sub> H <sub>3</sub> F	vinyl fluoride	-14.79 (×1)	-13.86 (×1)	-10.60 (×1)	2.80 (×1)	3.93 (×1)	4.34 (×1)
C <sub>2</sub> H <sub>3</sub> Cl	vinyl chloride	-13.21 (×1)	-11.65 (×1)	-10.13 (×1)	2.12 (×1)	3.49 (×1)	3.84 (×1)
C <sub>2</sub> H <sub>3</sub> Br	vinyl bromide	-13.38 (×1)	-10.71 (×1)	-9.29 (×1)	2.02 (×1)	3.55 (×1)	4.27 (×1)
C <sub>2</sub> H <sub>3</sub> I	vinyl iodide	-11.71 (×1)	-9.92 (×1)	-9.36 (×1)	1.40 (×1)	1.75 (×1)	3.59 (×1)
CF <sub>4</sub>	tetrafluoromethane	-18.35 (×2)	-17.37 (×2)	-16.24 (×3)	4.89 (×1)	6.86 (×2)	9.20 (×2)
CCl <sub>4</sub>	tetrachloromethane	-13.40 (×2)	-12.46 (×3)	-11.60 (×3)	0.86 (×1)	2.20 (×3)	5.20 (×1)
CBr <sub>4</sub>	tetrabromomethane	-12.13 (×2)	-11.25 (×3)	-10.48 (×2)	-0.49 (×1)	1.21 (×3)	4.60 (×1)
Cl <sub>4</sub>	tetraiodomethane		-9.99 (×2)	-9.30 (×2)	-1.62 (×1)	0.34 (×2)	4.73 (×2)
SiH <sub>4</sub>	silane		-18.46 (×1)	-12.84 (×3)	3.10 (×3)	3.71 (×1)	6.75 (×2)
GeH <sub>4</sub>	germane	-38.07 (×1)	-18.69 (×1)	-12.53 (×2)	3.16 (×1)	3.54 (×3)	7.04 (×2)
Si <sub>2</sub> H <sub>6</sub>	disilane	-12.25 (×1)	-12.25 (×1)	-10.71 (×1)	2.27 (×1)	2.28 (×2)	2.75 (×1)
Si <sub>5</sub> H <sub>12</sub>	pentasilane	-10.84 (×1)	-10.64 (×1)	-9.36 (×1)	0.79 (×1)	1.57 (×1)	1.61 (×1)
LiH	lithium hydride		-64.54 (×1)	-7.96 (×1)	0.09 (×1)	2.01 (×2)	3.41 (×1)
KH	potassium hydride	-24.59 (×2)	-24.38 (×1)	-6.13 (×1)	-0.04 (×1)	1.60 (×2)	1.90 (×1)
BH <sub>3</sub>	borane		-18.35 (×1)	-13.31 (×2)	0.33 (×1)	3.36 (×1)	4.32 (×2)
B <sub>2</sub> H <sub>6</sub>	diborane	-14.00 (×1)	-13.48 (×1)	-12.29 (×1)	1.20 (×1)	2.51 (×1)	3.46 (×1)
NH <sub>3</sub>	ammonia	-27.78 (×1)	-16.52 (×2)	-10.77 (×1)	2.84 (×1)	5.26 (×2)	11.18 (×2)
HN <sub>3</sub>	hydrazoic acid	-15.92 (×1)	-12.25 (×1)	-10.72 (×1)	2.02 (×1)	3.02 (×1)	3.17 (×1)
PH <sub>3</sub>	phosphine	-20.25 (×1)	-13.75 (×2)	-10.57 (×1)	2.95 (×1)	3.12 (×2)	7.11 (×2)
AsH <sub>3</sub>	arsine	-19.82 (×1)	-13.18 (×2)	-10.42 (×1)	2.86 (×1)	3.01 (×2)	7.44 (×2)
SH <sub>2</sub>	hydrogen sulfide	-15.65 (×1)	-13.39 (×1)	-10.35 (×1)	2.79 (×1)	3.20 (×1)	7.25 (×1)
FH	hydrogen fluoride	-39.30 (×1)	-19.84 (×1)	-15.90 (×1)	3.07 (×1)	14.20 (×1)	17.24 (×1)
ClH	hydrogen chloride	-25.44 (×1)	-16.65 (×1)	-12.64 (×1)	2.70 (×1)	7.91 (×1)	12.18 (×1)

LiF	lithium fluoride	-33.11 (×1)	-11.76 (×1)	-11.28 (×2)	-0.02 (×1)	2.74 (×2)	3.51 (×1)
F <sub>2</sub> Mg	magnesium fluoride	-14.15 (×1)	-13.76 (×2)	-13.71 (×1)	-0.04 (×1)	1.94 (×2)	4.13 (×1)
TiF <sub>4</sub>	titanium fluoride	-16.86 (×1)	-16.29 (×2)	-15.69 (×2)	-1.06 (×2)	0.07 (×3)	0.98 (×1)
AlF <sub>3</sub>	aluminum fluoride	-16.08 (×2)	-15.86 (×2)	-15.31 (×1)	0.67 (×1)	1.86 (×1)	3.90 (×2)
BF	boron monofluoride	-21.27 (×1)	-18.16 (×2)	-11.20 (×1)	1.51 (×2)	3.29 (×1)	4.70 (×1)
SF <sub>4</sub>	sulfur tetrafluoride	-15.26 (×1)	-15.04 (×1)	-12.70 (×1)	0.94 (×1)	3.79 (×1)	4.86 (×1)
BrK	potassium bromide	-19.37 (×1)	-8.41 (×1)	-8.17 (×2)	-0.45 (×1)	1.40 (×2)	1.73 (×1)
GaCl	gallium monochloride	-14.09 (×1)	-11.46 (×2)	-9.79 (×1)	0.27 (×2)	2.49 (×1)	6.60 (×1)
NaCl	sodium chloride	-20.83 (×1)	-9.55 (×1)	-9.12 (×2)	-0.59 (×1)	1.18 (×2)	2.08 (×1)
MgCl <sub>2</sub>	magnesium chloride	-12.52 (×1)	-11.88 (×2)	-11.76 (×2)	-0.19 (×1)	1.40 (×2)	3.91 (×1)
AlI <sub>3</sub>	aluminum chloride	-10.39 (×2)	-10.29 (×2)	-9.84 (×1)	-0.33 (×1)	-0.28 (×1)	2.25 (×2)
BN	boron nitride	-27.96 (×1)	-13.69 (×1)	-11.93 (×2)	-3.16 (×1)	2.65 (×2)	3.69 (×1)
NCH	hydrogen cyanide	-20.60 (×1)	-13.91 (×1)	-13.90 (×1)	3.21 (×2)	3.45 (×1)	4.55 (×1)
PN	phosphorus mononitride	-16.37 (×1)	-12.42 (×1)	-11.80 (×1)	0.46 (×1)	3.40 (×1)	8.42 (×1)
H <sub>2</sub> NNH <sub>2</sub>	hydrazine	-15.39 (×1)	-11.28 (×1)	-9.62 (×1)	2.51 (×1)	3.69 (×1)	4.55 (×1)
H <sub>2</sub> CO	formaldehyde	-16.04 (×1)	-14.56 (×1)	-10.78 (×1)	1.67 (×1)	3.68 (×1)	5.24 (×1)
CH <sub>4</sub> O	methanol	-14.32 (×1)	-13.33 (×1)	-10.18 (×1)	1.91 (×1)	3.14 (×1)	4.00 (×1)
C <sub>2</sub> H <sub>6</sub> O	ethanol	-13.43 (×1)	-12.27 (×1)	-10.61 (×1)	2.86 (×1)	3.73 (×1)	4.69 (×1)
C <sub>2</sub> H <sub>4</sub> O	acetaldehyde	-14.32 (×1)	-13.33 (×1)	-10.18 (×1)	1.91 (×1)	3.14 (×1)	4.00 (×1)
C <sub>4</sub> H <sub>10</sub> O	ethoxy ethane	-12.36 (×1)	-11.50 (×1)	-9.75 (×1)	2.96 (×1)	3.46 (×1)	3.93 (×1)
CH <sub>2</sub> O <sub>2</sub>	formic acid	-14.94 (×1)	-12.55 (×1)	-11.42 (×1)	2.70 (×1)	3.07 (×1)	4.29 (×1)
HOOH	hydrogen peroxide	-15.38 (×1)	-12.84 (×1)	-11.39 (×1)	3.01 (×1)	3.02 (×1)	4.87 (×1)
H <sub>2</sub> O	water	-18.90 (×1)	-14.70 (×1)	-12.48 (×1)	2.88 (×1)	4.91 (×1)	13.32 (×1)
CO <sub>2</sub>	carbon dioxide	-18.11 (×1)	-17.99 (×2)	-13.73 (×1)	2.80 (×1)	4.29 (×2)	6.59 (×1)
CS <sub>2</sub>	carbon disulfide	-14.57 (×1)	-13.27 (×2)	-10.01 (×2)	0.29 (×2)	3.34 (×1)	4.46 (×1)
OCS	carbon oxide sulfide	-16.12 (×1)	-16.12 (×2)	-11.24 (×2)	1.85 (×2)	3.13 (×1)	4.78 (×1)
OCS <sub>e</sub>	carbon oxide selenide	-15.89 (×2)	-15.63 (×1)	-10.50 (×2)	1.44 (×2)	2.60 (×1)	4.18 (×1)
CO	carbon monoxide	-19.42 (×1)	-15.49 (×1)	-14.37 (×1)	1.22 (×2)	5.30 (×1)	6.59 (×1)
O <sub>3</sub>	ozone	-13.48 (×1)	-12.93 (×1)	-12.79 (×1)	-1.52 (×1)	5.23 (×1)	7.28 (×1)
SO <sub>2</sub>	sulfur dioxide	-13.50 (×1)	-13.12 (×1)	-12.37 (×1)	-0.34 (×1)	3.98 (×1)	4.39 (×1)
BeO	beryllium monoxide	-26.77 (×1)	-10.97 (×1)	-9.88 (×2)	-2.01 (×1)	2.31 (×1)	2.48 (×1)
MgO	magnesium monoxide	-24.89 (×1)	-8.76 (×1)	-8.17 (×2)	-1.29 (×1)	1.16 (×2)	2.90 (×1)
C <sub>7</sub> H <sub>8</sub>	toluene	-11.74 (×1)	-9.19 (×1)	-8.90 (×1)	1.71 (×1)	1.85 (×1)	2.97 (×1)
C <sub>8</sub> H <sub>10</sub>	ethylbenzene	-11.57 (×1)	-9.15 (×1)	-8.85 (×1)	1.76 (×1)	1.76 (×1)	2.85 (×1)
C <sub>6</sub> F <sub>6</sub>	hexafluorobenzene	-14.09 (×1)	-13.12 (×1)	-10.15 (×2)	1.08 (×2)	1.15 (×1)	3.66 (×2)
C <sub>6</sub> H <sub>5</sub> OH	phenol	-11.99 (×1)	-9.42 (×1)	-8.69 (×1)	1.62 (×1)	2.35 (×1)	2.84 (×1)
C <sub>6</sub> H <sub>5</sub> NH <sub>2</sub>	aniline	-11.01 (×1)	-9.21 (×1)	-7.98 (×1)	1.83 (×1)	2.29 (×1)	2.82 (×1)
C <sub>5</sub> H <sub>5</sub> N	pyridine	-10.45 (×1)	-9.74 (×1)	-9.72 (×1)	1.24 (×1)	1.62 (×1)	3.21 (×1)
C <sub>5</sub> H <sub>5</sub> N <sub>5</sub> O	guanine	-10.05 (×1)	-9.81 (×1)	-8.04 (×1)	1.57 (×1)	1.87 (×1)	1.98 (×1)
C <sub>5</sub> H <sub>5</sub> N <sub>5</sub>	adenine	-9.59 (×1)	-9.39 (×1)	-8.33 (×1)	1.28 (×1)	2.06 (×1)	2.51 (×1)
C <sub>4</sub> H <sub>5</sub> N <sub>3</sub> O	cytosine	-9.66 (×1)	-9.54 (×1)	-8.78 (×1)	0.92 (×1)	2.29 (×1)	2.51 (×1)

C <sub>5</sub> H <sub>6</sub> N <sub>2</sub> O <sub>2</sub>	thymine	-10.55 (×1)	-10.19 (×1)	-9.15 (×1)	0.77 (×1)	2.15 (×1)	2.42 (×1)
C <sub>4</sub> H <sub>4</sub> N <sub>2</sub> O <sub>2</sub>	uracil	-10.65 (×1)	-10.29 (×1)	-9.57 (×1)	0.70 (×1)	2.10 (×1)	2.35 (×1)
CH <sub>4</sub> N <sub>2</sub> O	urea	-10.65 (×1)	-10.52 (×1)	-10.08 (×1)	2.33 (×1)	3.51 (×1)	4.09 (×1)
Ag <sub>2</sub>	silver dimer	-11.08 (×2)	-10.82 (×1)	-7.41 (×1)	-0.70 (×1)	1.00 (×2)	1.41 (×1)
Cu <sub>2</sub>	copper dimer	-9.37 (×2)	-9.22 (×1)	-7.38 (×1)	-0.34 (×1)	2.11 (×1)	2.16 (×2)
NCCu	copper cyanide	-12.17 (×1)	-11.21 (×2)	-10.69 (×1)	-0.98 (×1)	1.92 (×2)	3.08 (×1)

Table 2.1: Quasiparticle energies (negative of the ionization potentials and electron affinities) of molecules in the *GW*100 calculated with IP/EA-EOM-CCSD in the def2-TZVPP basis set.

#### 2.4.5 Accuracy of approximate EOM-CCSD

We next assess the accuracy of approximations to EOM-CCSD, using the *GW*100 test set. Henceforth, we compare all approximations to EOM-CCSD, and not to  $\Delta$ CCSD(T), for a number of reasons. First, the comparison is perhaps the most fair because all approximate techniques are derived from EOM-CCSD, and so the most we can expect is that they reproduce this parent method. Second, although EOM-CCSD was shown above to provide an accurate reproduction of the  $\Delta$ CCSD(T) values, the latter approach can be challenging for open-shell systems like those used in the  $(N \pm 1)$ -electron calculations. For example, while the unrestricted formalism used in Ref.[92] provides a better approximate treatment of multireference effects, it also suffers from spin contamination, which can affect the IPs and EAs by up to 0.5 eV, as discussed in Ref.[126]. Third, it allows us to compare EAs, which are not available in the literature based on  $\Delta$ CCSD(T).

In Tab. 2.2, we present IP and EA error metrics for a variety of approximate techniques (all 100 molecules were studied by each approach except for CC2-based approaches, because the ground-state CC2 failed to converge for twelve molecules; the full data set for individual molecules is given as Supplemental Material). Perhaps most remarkably, we find that all CC-based methods exhibit MEs of less than 0.13 eV and MAEs of less than 0.16 eV. These results can be compared to those based on the *GW* approximation, as given in Tab. 2.2. These latter results are taken from Ref.[93] and include only ionization potentials compared to CCSD(T) data; given the good agreement between CCSD(T) and IP-EOM-CCSD shown above, we expect similar error metrics

Method	IP ME (eV)	IP MAE (eV)	EA ME (eV)	EA MAE
EOM-linCCSD	0.13	0.14	0.05	0.11
EOM-CC2	0.00	0.14	0.08	0.15
EOM-MBPT2	0.03	0.13	0.08	0.16
P-EOM-CC2	-0.08	0.12	-0.04	0.08
P-EOM-MBPT2	-0.08	0.16	-0.03	0.08
GF2@HF	-0.38	0.42	-0.19	0.22
$G_0W_0$ @HF [93]	0.26	0.35		
$G_0W_0$ @PBE [93]	-0.69	0.69		
scGW [93]	-0.30	0.32		

Table 2.2: Mean error (ME) and mean absolute error (MAE) in eV of ionization potentials (IPs) and electron affinities (EAs) for molecules contained in the  $GW100$  test set. Error metrics are calculated with respect to IP/EA-EOM-CCSD without approximation, except for the  $GW$  results from Ref. [93], which are calculated with respect to  $\Delta$ CCSD(T) results from Ref.[92].

if the  $GW$  results were compared to IP-EOM-CCSD instead. Depending on the choice of mean-field reference or with full self-consistency,  $GW$ -based approximations give errors on the order of 0.3 – 0.7 eV.

Overall, we see that approximations in the ground-state calculation lead to an average increase in the IP or EA and approximations in the EOM calculation lead to an average decrease in the IP or EA. This behavior can be understood because most perturbative approximations to CCSD lead to overcorrelation, which decreases the ground-state energy (increases the IP or EA) or decreases the excited-state energy (decreases the IP or EA).

Without any partitioning, the EOM-linCCSD, EOM-CC2, and EOM-MBPT2 all perform similarly. Although the error incurred by the most expensive linearized CCSD is slightly larger (compared to the other approximate treatments of the ground state), the error is extremely systematic with a very small spread; for example, over 50 molecules overestimate the IP by 0.1 eV and another 30 molecules overestimate the IP by 0.2 eV. All  $N^5$  approximate methods – based on CC2 or MBPT2, with or without partitioning – perform impressively well. EOM-CC2 and EOM-MBPT2 exhibit very similar results (even on the level of individual molecules), suggesting that the orbital relaxation due to  $\hat{T}_1$  is not important in many of these cases. With partitioning, the ME becomes only slightly negative without any significant increase in the MAE.

The qualitatively similar performance of all approximate EOM-CC methods and their improvement compared to  $G_0W_0@HF$  suggests that the precise details of screening are not important in molecules, and perhaps second-order exchange is more important. To test this, we also show the results of IPs and EAs calculated using the second-order Green’s function (GF2); the mean error is large and negative,  $-0.38$  eV for IPs and  $-0.19$  eV for EAs, which can be compared to the IP results of  $G_0W_0@HF$ ,  $+0.26$  eV. Remarkably, the P-EOM-MBPT2 approach, which has essentially identical cost as GF2, reduces the mean error of the latter to only  $-0.08$  eV. This result suggests that the combination of second-order exchange with a small amount of screening, beyond the second-order ring diagram, is important for quantitative accuracy. Given the extremely low cost, we identify P-EOM-MBPT2 as an attractive low-cost approach for IPs and EAs of larger molecules, with potential applications in the solid state. However, it must be kept in mind that the increased importance of screening in solids may preclude the success of perturbative approximations.

## 2.5 Conclusions and outlook

To summarize, we have presented a diagrammatic, algebraic, and numerical evaluation of quasiparticle excitation energies predicted by EOM-CCSD, especially as compared to those of the  $GW$  approximation. Although the EOM-CCSD Green’s function includes fewer ring diagrams than the  $GW$  approximation, we find that its inclusion of many more diagrams – including ladders and exchange – produces excitation energies that are much more accurate than those from the  $GW$  approximation. To completely encompass all  $GW$  diagrams requires the use of non-perturbative EOM-CCSDT.

We also investigated the accuracy of a number of cost-saving approximations to EOM-CCSD, many of which reduce the canonical scaling to  $N^5$  (which could be further reduced through density-fitting [127] or tensor hypercontraction [128]). All CC-based approximations considered yield very small errors on average. For systems where screening is relatively unimportant, such as molecules or large band-gap insulators, we identify P-EOM-MBPT2 as an accurate and inexpensive  $N^5$  ap-

proach. We attribute the success of P-EOM-MBPT2 to its exact treatment of screening and exchange through second order (as in GF2), combined with a small number of third-order diagrams.

We anticipate that the framework and connections laid out here will aid future work on the *GW* approximation, through the identification of the most important excluded diagrams. With respect to IP/EA-EOM-CCSD calculations of band structures in solids [1], the present work motivates efforts to quantify the error induced by neglecting some of the non-TDA ring diagrams, which are conventionally thought to be crucial for screening in solids. In the same vein, the inclusion of triple excitations, perhaps even perturbatively, could be an important ingredient in recovering – and rigorously surpassing – RPA physics.

## Chapter 3: Composite and Hybrid Methods

The material for this chapter was taken from Reference [129]

### 3.1 Introduction

The formidable scaling of canonical coupled-cluster theory, which limits its applicability to large systems, has motivated the development of myriad cost-saving approaches. A nonexhaustive list includes the use of frozen natural orbitals [130, 131, 15], local correlation [132, 41, 133, 134, 135], and F12 theory [20]. Most relevant to the present work are the various hybrid approaches combining different levels of single-reference coupled-cluster (CC) or perturbation theory [136, 137], including active-space CC [138, 139], the CC(P;Q) framework [140, 141], partitioned equation-of-motion CC [116, 118, 117, 45], and multilevel CC [142, 143, 144].

In the present work, we are motivated by recent applications of CC theory to atomistic solids [96, 145, 1, 146, 147, 148, 4]. Many gapped semiconductors and insulators are only moderately correlated and thus CC theory with single and double excitations (CCSD) has been found to work well. However, the  $k$ -point sampled supercells may contain up to hundreds of electrons in thousands of orbitals. Therefore, here we limit our discussion to CCSD in both its ground-state [125] and excited-state equation-of-motion (EOM) [149, 79, 80] frameworks. Extensions to higher-order CC theories or combinations with other reduced cost approaches are straightforward to imagine.

More so than ground-state calculations, a main motivation in this work is to reduce the cost of subsequent excited-state calculations for ionization potentials (IPs), electron affinities (EAs), and neutral electronic excitations (EEs). Even though ground-state CCSD has  $N^6$  cost, which is higher than or equal to that of EOM-CCSD for IPs/EAs and EEs –  $N^5$  and  $N^6$  respectively – many excited-state calculations are dominated by the EOM step, for a variety of reasons. Ground-state

calculations require the solution of the  $t$ -amplitude equations, which have a (presumed) unique solution that can be quickly found using a variety of convergence accelerators, commonly leading to convergence within about ten iterations. By contrast, excited state eigenvalues are commonly found through a series of matrix-vector multiplications within the Davidson algorithm; here the potential need to find many eigenvalues increases the cost and numerical issues such as root-flipping frustrate convergence. Again looking ahead to the solid-state, excitation *spectra* are much more insightful than a few low-lying eigenvalues, and these spectra require only a single ground-state calculation but *many* EOM matrix-vector multiplies.

Seeking efficient EOM-CCSD calculations, the main purpose of this work is to present and test an EOM technique that partitions double excitations into those that are internal and those that are external to a predefined active space; the former will be treated by CC theory, the latter by perturbation theory, and they will be allowed to interact with one another. In the limit where *all* double excitations are treated perturbatively, our method will reduce to the ‘partitioned’ EOM approach first presented in Refs. [116, 117]. Going beyond this partitioned EOM approach, we will show that the selective nonperturbative inclusion of a few low-lying double excitations can significantly improve the quality of the results. Within the proposed EOM approach, it is natural to solve the preceding ground-state CCSD equations at the same level of theory, for both formal and computational reasons. This leads to a ground-state method first derived by Nooijen [136], later discussed by Bochevarov and Sherrill [137], and more recently developed by Koch and co-workers [142, 143, 144] as multilevel coupled-cluster theory. We emphasize that our presentation of this ground-state method is only review, to lay the foundation for hybrid approaches to excitation energies, which has been significantly less explored.

The layout of this article is as follows. In Sec. 3.2.1, we define the active space, relevant excitations, and the use of canonical and natural orbitals. In Sec. 3.2.2, we review the combination of CC and perturbation theory for ground states. In Sec. 3.2.3, we extend this partitioning of excitations to the calculation of excited states in the EOM-CCSD framework. In Sec. 3.3, we present the results of these methods on a test set of small molecules and present a few preliminary

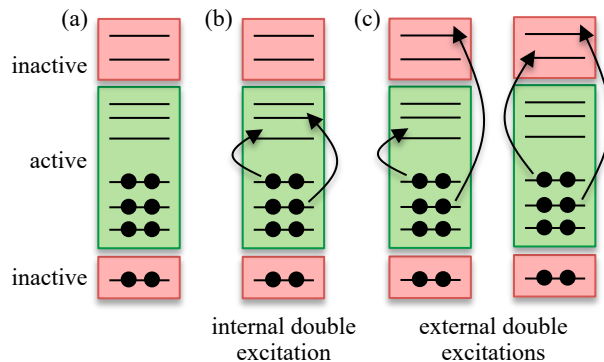


Figure 3.1: Orbital partitioning into active and inactive (a) and examples of an internal double excitation (b) and external double excitations (c).

calculations on solids. In Sec. 3.4, we conclude and provide an outlook.

## 3.2 Theory

### 3.2.1 Orbitals and excitations

All of our methods are single-reference in nature and we will assume a Hartree-Fock (HF) reference throughout. Molecular orbitals that are occupied are indexed by  $i, j, k, l$  and orbitals that are unoccupied are indexed by  $a, b, c, d$  (but may not correspond to canonical HF virtuals). We partition these molecular orbitals into those that are active and those that are inactive (sometimes called frozen). Following typical active space nomenclature, excitations that involve *only* active orbitals will be defined as ‘internal’. Remaining excitations are commonly partitioned into semi-internal (involving active and inactive orbitals) and external (inactive orbitals only); these two classes of excitations will be treated equally in our work and so we will refer to both types of excitations as ‘external.’ A schematic of the active space and associated internal and external double excitations is shown in Fig. 3.1.

A large improvement in the behavior of methods with truncated basis sets is achieved through the use of approximate natural orbitals (NOs), which diagonalize the one-electron reduced density matrix in the virtual space  $\gamma_{ab}$ ,  $\gamma\mathbf{V} = \mathbf{V}\mathbf{n}$ . Here, we use the MP2 density matrix and its associated NOs. Based on the eigenvalues  $n_a$ , the set of NOs is divided in two. Following Ref. [15], we

separate the  $K$  orbitals to the  $L$  most important NOs based on the percent occupation,

$$\sum_{a=1}^L \frac{n_a}{N} = \text{tol.} \tag{3.1}$$

where  $N = \sum_{a=1}^K n_a$  and  $\text{tol.}$  is a user-defined tolerance. A tolerance between 98 and 100% roughly corresponds to a number of NOs that is 30–100% of the original number of virtual COs. These  $L$  NOs are included in the virtual part of the active space and the remaining  $K - L$  NOs are inactive.

For simplicity, the Fock matrix is typically diagonalized in the active NO basis via a transformation to semicanonical orbitals. In our calculations that treat active and inactive orbitals simultaneously, we will test the use of a split semicanonical basis: we rotate the virtual block of the Fock matrix into the NO basis and then separately diagonalize it in the truncated NO space and in the remaining orbital space. This is similar to what is done in the construction of valence virtual orbitals [150] and in multilevel CC calculations [151].

We note that Refs. [136, 137], which were early works concerning the hybrid ground-state approach described here, operated in the CO basis, whereas the multilevel coupled-cluster approach [142, 143] typically uses localized orbitals and treats physical regions of the molecule at different levels of theory. In the context of relatively homogeneous extended systems (studied in Sec. 3.3.2), delocalized orbital partitioning is more straightforward, especially because it allows the most efficient Brillouin zone sampling. However, the use of localized orbital partitioning would correspond to a kind of periodic embedding (similar to one-shot density matrix embedding theory [152, 153] or dynamical mean-field theory [154]) that is interesting to consider in future research.

### 3.2.2 Ground-state approximations

As discussed in the introduction, our goal is to test a class of methods that partition the excitations into those that are internal and those that are external to an active space of orbitals, to be treated by CCSD and perturbation theory respectively. Moreover, we seek methods that allow these

two classes of excitations to *interact*. Here we review such a method for ground-state calculations, first presented by Nooijen [136] (who called it CC/PT), later discussed by Bochevarov and Sherrill [137] (who called it CCSD-MP2), and most recently developed by Koch and co-workers [142] (who called it extended CC2 or multilevel CC). However, the idea of internal/external partitioning in CC theory has naturally appeared in multireference formulations [155], including the use of perturbative external amplitudes [156].

We write the CCSD excitation operator as a sum of internal and external excitation operators,

$$T = T^{(\text{int})} + T^{(\text{ext})} \quad (3.2)$$

where the external excitation operator is fixed to its first-order perturbative (MP2) value,

$$T^{(\text{ext})} = \frac{1}{4} \sum_{(ijab)}^{\text{ext}} t_{ij}^{ab} a_a^\dagger a_b^\dagger a_j a_i \quad (3.3)$$

$$t_{ij}^{ab} = \frac{\langle ab || ij \rangle}{\varepsilon_i + \varepsilon_j - \varepsilon_a - \varepsilon_b} \quad (3.4)$$

where the notation indicates that the excitation  $(ijab)$  is an external excitation, i.e. one or more of the orbital indices are inactive. The internal excitation operator has the usual CCSD form

$$T^{(\text{int})} = \sum_{(ia)}^{\text{int}} t_i^a a_a^\dagger a_i + \frac{1}{4} \sum_{(ijab)}^{\text{int}} t_{ij}^{ab} a_a^\dagger a_b^\dagger a_j a_i \quad (3.5)$$

and its amplitudes are determined by solving the CCSD equations in the space of single and double internal excitations

$$\langle \Phi_i^a | e^{-T} H e^T | \Phi \rangle = 0, \quad (ia) \text{ internal} \quad (3.6a)$$

$$\langle \Phi_{ij}^{ab} | e^{-T} H e^T | \Phi \rangle = 0, \quad (ijab) \text{ internal.} \quad (3.6b)$$

This scheme leads to the iterative, infinite-order solution of the internal excitation amplitudes in the presence of the external excitation amplitudes, fixed to their value from first-order perturbation

theory. Because the internal amplitudes interact with the external amplitudes, we will refer to this as an ‘interacting’ method that combines CCSD and MP2, denoted i-CCSD/MP2. The final correlation energy  $E_c$  is calculated in the usual way and includes contributions from both internal and external excitations,

$$E_c^{\text{int}} = \frac{1}{4} \left[ \sum_{(ijab)}^{\text{int}} + \sum_{(ijab)}^{\text{ext}} \right] \langle ij || ab \rangle \left( t_{ij}^{ab} + 2t_i^a t_j^b \right). \quad (3.7)$$

The i-CCSD/MP2 approach can be considered as an extension of the active space CC approach, e.g. CCSD. Whereas the latter only includes a select set of internal excitations at a given level, i-CCSD/MP2 additionally includes their coupling to perturbatively-evaluated external excitations at the same level. Furthermore the internal-external coupling is present during the CC iterations, which distinguishes i-CCSD/MP2 from noniterative perturbation theory corrections.

In the limit where the internal amplitudes are completely disconnected from the external amplitudes, the above method reduces to a simple and well-known ‘composite’ method, which we will call c-CCSD/MP2. This approach combines the results of three calculations: CCSD in an active space (i.e. with truncated orbitals), MP2 in the same active space, and MP2 in the full orbital space, leading to the correlation energy

$$E_c^{\text{comp}} = E_{\text{CCSD}}^{(\text{act})} + E_{\text{MP2}}^{(\text{full})} - E_{\text{MP2}}^{(\text{act})}. \quad (3.8)$$

Finally, in the extreme limit where we neglect the perturbative correction, we have a ‘truncated’ method, to be referred to as t-CCSD, with correlation energy

$$E_c^{\text{trunc}} = E_{\text{CCSD}}^{(\text{act})}. \quad (3.9)$$

To summarize, we have three different schemes that combine CCSD and perturbation theory – truncated, composite, and interacting (t-, c-, and i-) – which can be performed in either the CO or NO basis. The methods have increasing costs that are summarized in Tab. 3.1.

Method	ground-state cost	IP cost	EA cost
Truncated	$O^2V^4$	$O^3V^2$	$O^2V^3$
Composite	$O^2V^4, o^2v^2$	$O^3V^2, o^3v$	$O^2V^3, ov^3$
Interacting	$O^2V^2v^2$	$Oo^2v^2$	$o^2v^2V$
CCSD	$o^2v^4$	$o^3v^2$	$o^2v^3$

Table 3.1: Computational scaling of the various methods considered in this work ignoring orbital transformations. The number of active occupied and virtual orbitals are denoted by  $O$  and  $V$  and the number of total occupied and virtual orbitals is denoted by  $o$  and  $v$ .

### 3.2.3 Excited-state approximations

Excitation energies in CC theory are commonly obtained with the EOM framework, which amounts to finding eigenvalues of the similarity-transformed, normal-ordered Hamiltonian  $\bar{H}_N = e^{-T}H_Ne^T$ . Here, we consider the  $T$  operator to be determined as above, which may correspond to using the first-order (MP2)  $T$ , the infinite-order CCSD  $T$ , or a hybrid CCSD/MP2  $T$ . The similarity transformed Hamiltonian is diagonalized in a subspace of single and double excitations.

As for the ground state, we partition the excitations in the calculation of excited states. In particular, all single excitations (internal and external) and internal double excitations will be treated without approximation. However, external double excitations will be treated perturbatively. In practice, this perturbative treatment amounts to a dense Hamiltonian block in the internal doubles space and a diagonal approximation in the external doubles space; for example, for IPs,

$$\langle \Phi_{ij}^a | e^{-T} H_N e^T | \Phi_{kl}^b \rangle \approx (\varepsilon_i + \varepsilon_j - \varepsilon_a) \delta_{ik} \delta_{jl} \delta_{ab}. \quad (3.10)$$

We have tested including the direct coupling between the internal and external double excitations, but we find that the results are largely unchanged and so we neglect this coupling; importantly, the internal and external double excitations still interact indirectly through the single excitations. Therefore, we refer to this method as i-EOM-CCSD/MP2 and reemphasize that we use the i-CCSD/MP2 ground-state solution. This approach is similar to that taken in the application of multilevel CCSD to excitation energies [143] where the use of correlated natural transition orbitals has been recently tested [151]. To our knowledge, multilevel CCSD has only been applied to neu-

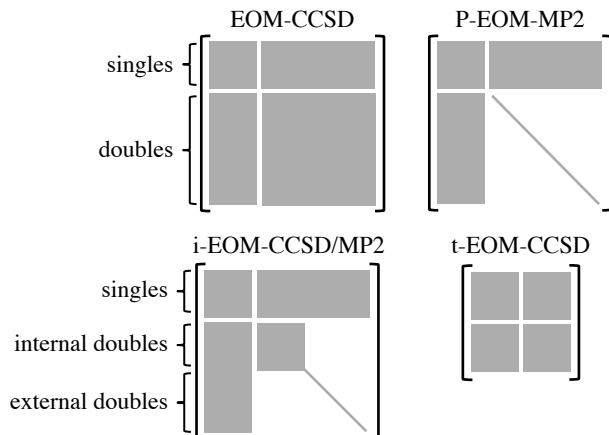


Figure 3.2: Structure of the similarity-transformed Hamiltonian matrices used in EOM-CCSD (top left), the partitioned EOM-MP2 approach (top right), the interacting i-EOM-CCSD/MP2 (bottom left), and the truncated t-EOM-CCSD (bottom right).

tral excitation energies and here we extend approaches of this type to charged excitation energies, i.e. ionization potentials and electron affinities. In the limit where all double excitations are treated perturbatively, our approach reduces to the conventional partitioned-EOM-MP2 (P-EOM-MP2) framework [116, 117, 45]. The structures of the EOM Hamiltonian matrix for these excited-state methods are shown in Fig. 3.2.

Like for the ground-state one can define schemes that are simpler than i-EOM-CCSD/MP2. The virtual space can be strictly truncated, leading to EOM-CCSD in an active space, i.e. t-EOM-CCSD. The resulting excitation energy can be corrected using a lower-level of theory, such as P-EOM-MP2, leading to the composite method for excitation energies c-EOM-CCSD/MP2. The computational cost of excited-state calculations is determined by matrix-vector products, also known as the sigma vector construction. In Tab. 3.1, we list the computational scaling associated with each of the excited-state methods discussed.

### 3.3 Results

Here we apply the above methods to a test set of small molecules and to a few solid state systems. All calculations were performed using PySCF [157]. All occupied orbitals, including core orbitals, were correlated.

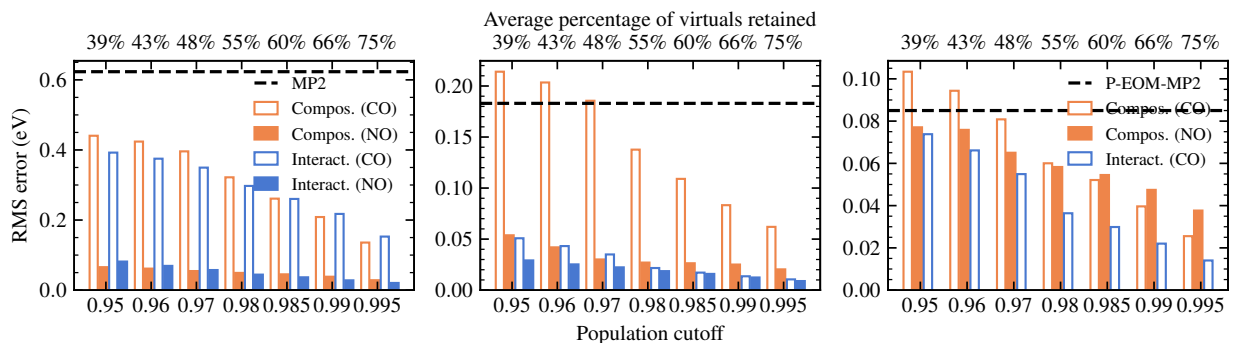


Figure 3.3: Root mean square error of the correlation energy (left), ionization potential (middle), and electron affinity (right) of 76 molecules selected from the GW100 test set, using the combination CCSD/MP2 schemes discussed here. Error is with respect to CCSD or EOM-CCSD. Various results are presented using the canonical orbital (CO) basis and the natural orbital (NO) basis.

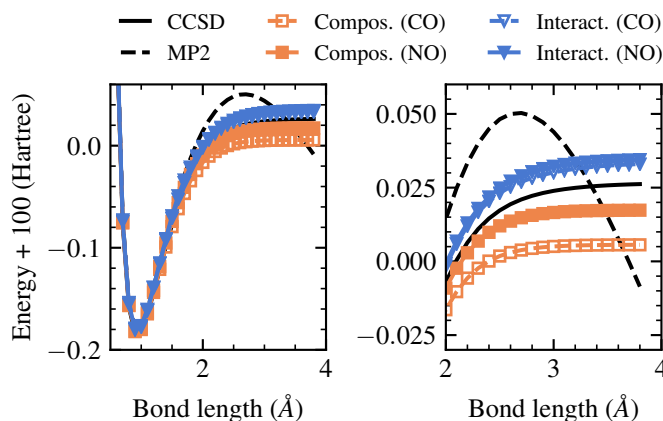


Figure 3.4: Bond dissociation curve for the HF molecule in the 6-31G\* basis with five active virtual orbitals. Right panel is zoomed into the dissociation region.

### 3.3.1 Molecules

Our molecular calculations were performed on the 76 smallest molecules from the GW100 test set [94], excluding H<sub>2</sub> and He, using the def2-TZVPP basis set.

In Fig. 3.3, we show the root-mean-square error in the correlation energy, IP, and EA, compared to CCSD or EOM-CCSD, as a function of the orbital truncation, produced by the composite method (orange) and by the interacting method (blue) in the CO basis (open bars) and the NO basis (filled bars). For comparison, we truncate canonical orbitals by keeping the same number of energy-ordered virtuals as prescribed by the NO truncation. In Fig. 3.3, we also list the average fraction of

virtual orbitals kept for a given orbital truncation threshold; over the range studied, the calculations retain about 40% to 75% of the virtuals.

Looking first at the correlation energy, we see that the composite and interacting methods perform very similarly and that both benefit enormously from a transformation to NOs. This suggests that the interaction between the internal and external amplitudes is not important. In fact, the composite method outperforms the more expensive interacting method for most orbital truncations. The interacting method in the NO basis performs the best when more than about half of the virtuals are retained. Most importantly, we note that either of the methods performed in the NO basis yield an average error of less than 0.1 eV (4 millihartree) with only 40% of the virtuals, which yields an enormous savings in the cost of the calculation due to the high  $v^4$  scaling of canonical CCSD.

This comparable performance in ground-state energies only holds for molecules near their equilibrium geometries, where both MP2 and CCSD are qualitatively correct. As discussed in Ref. [137] and shown as an example in Fig. 3.4 (dissociation of the HF molecule), the interacting method gives improved results over the composite method for molecules at stretched geometries corresponding to single-bond breaking. This improvement is most significant in the CO basis, which was the case investigated in Ref. [137], however the performance is more similar in the NO basis. Looking forward towards condensed-phase systems, we expect to see similar behavior for three-dimensional metallic systems, where the MP2 energy diverges but the CCSD energy converges [158].

Next, we move on to the results for the excited-state methods, also shown in Fig. 3.3. For simplicity, we limit our results to IPs and EAs, but the method can be straightforwardly applied to neutral excitation energies. For IPs, we see that the interacting method is relatively insensitive to the basis and significantly outperforms the composite method in the CO basis. In fact, the interacting method in the CO basis performs about the same as the composite method in the NO basis. Based on their similar ground-state behavior, we conclude that the superior performance of the interacting method is due to the (indirect) interaction between internal and external double

excitations in the EOM Hamiltonian matrix. For EAs, the composite method performs much better than it did for IPs in the canonical basis; similar behavior has been observed before for neutral excitation energies [14]. In the NO basis, the interacting method does not perform particularly well for EAs (not shown), exhibiting errors on the order of 0.3 eV or more. We attribute this to the inappropriate choice of NOs for EAs, as just mentioned.

### 3.3.2 Solids

We have performed preliminary applications of the presented methods to two solids: lithium fluoride (a large gap insulator) and silicon (a small gap semiconductor). All calculations were performed at the  $\Gamma$  point of the Brillouin zone of a cubic eight-atom unit cell using GTH pseudopotentials [159, 160] and the GTH-DZVP basis set [161]. Sampling the  $\Gamma$  point only allowed us to use a molecular implementation of the methods. The results here surely have finite-size errors and future work will be devoted to an implementation of these methods with  $k$ -point sampling and translational symmetry.

First, in Fig. 3.5, we show results for the LiF crystal, including the correlation energy per formula unit and the quasiparticle band gap (IP+EA). Although the large band gap of LiF may suggest the relative unimportance of higher-order perturbation theory, we note that MP2 and CCSD yield correlation energies that differ by 1 eV. Turning to approximate CC methods, we first observe that a naive truncation of virtuals in the CO basis gives very poor convergence to the full CCSD result, but freezing in the NO basis gives a significant improvement, as has been already shown in plane-wave-based CCSD calculations [96]. Correcting the truncated result with the composite method yields rapid convergence in the NO basis, but less so in the CO basis. Convergence to 0.1 eV can be achieved with the composite method in the NO basis using only about one-third of the total number of virtuals. This result is quite surprising given the relatively small size of the GTH-DZVP basis set. Similar to their performance in molecules, we see that the interacting approaches give smooth convergence that is similar to the composite methods but performs slightly better in the CO basis but slightly worse in the NO basis.

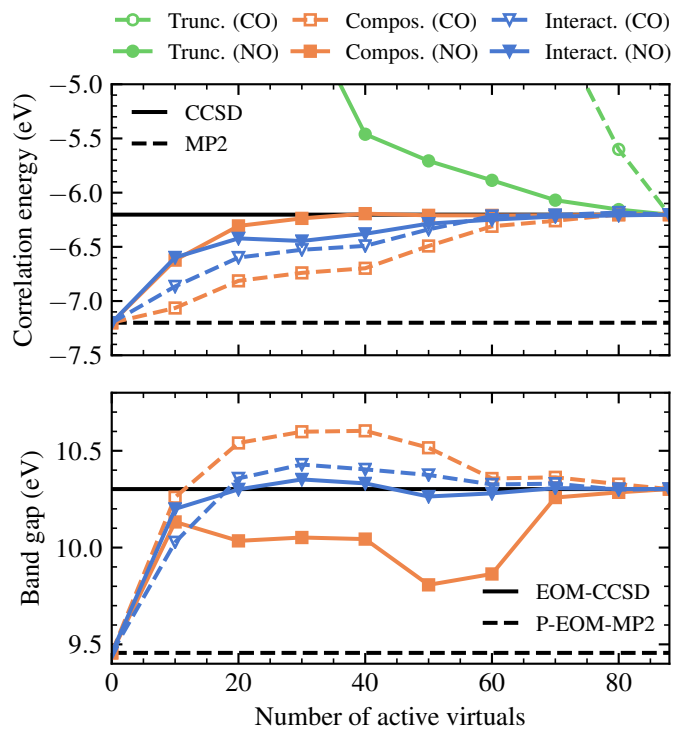


Figure 3.5: Correlation energy per formula unit (top) and quasiparticle band gap (bottom) for the lithium fluoride crystal in the GTH-DZVP basis for a cubic eight-atom cell.

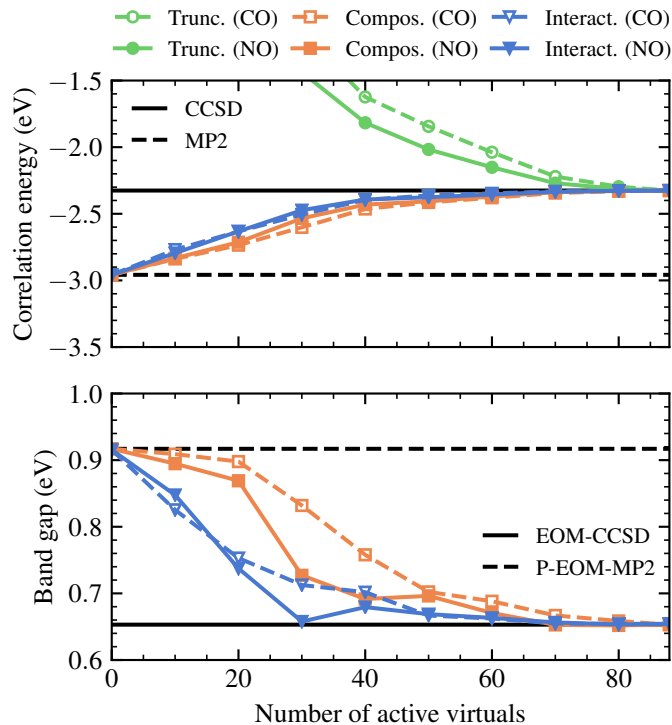


Figure 3.6: The same as in Fig. 3.5, but for the silicon crystal.

In the bottom panel of Fig. 3.5, we show the convergence of the band gap. First we note that EOM-CCSD and the much cheaper P-EOM-MP2 differ by about 0.8 eV, corresponding to a 10% error for the latter. In contrast to its behavior for the correlation energy, the composite method does not perform particularly well for band gaps, in either the CO or NO basis, exhibiting errors on the order of 0.3–0.5 eV until the virtual space is nearly exhausted. The interacting method displays the most systematic behavior and rapid convergence with an increasing number of virtuals. In particular, the interacting method in the NO basis reliably converges the band gap to within 0.1 eV using only 15% of the virtuals. For comparison, the experimental band gap of LiF is approximately 14 eV [162], however we emphasize that our results are not in the thermodynamic limit.

In Fig. 3.6, we show the same data but for the Si crystal. Compared to LiF, Si has a much smaller band gap, which may change the behavior of the methods that combine CCSD and MP2. Looking at the correlation energy, we see that all methods converge more slowly towards the CCSD result. Surprisingly, the use of NOs is significantly less drastic, especially for simple truncation.

The composite and interacting methods perform very similarly and 0.1 eV accuracy is obtained with about half of the virtual space. Results are similar for the band gap, which is converged by the interacting method to the same accuracy with roughly the same number of virtuals; the composite method converges more smoothly than it did for LiF, but still more slowly than the interacting method. Again, for rough comparison only, the experimental indirect band gap of silicon is about 1.1 eV, which is accurately reproduced by EOM-CCSD in the thermodynamic limit [1].

### 3.4 Conclusions

We have discussed and compared a number of ground-state and excited-state methods that combine CC and perturbation theory based on a partitioning of excitations that are internal or external to an active space. We furthermore compared performance in the canonical orbital basis and the semicanonical natural orbital basis. On a test set of small molecules at their equilibrium geometries, the composite method and the interacting method yield similar performance; the former is cheaper but may break down in physical regimes where MP2 fails qualitatively. The use of semicanonical natural orbitals provides significant improvement in the both the composite and interacting methods.

We presented the first applications of many of these methods to periodic solids, using lithium fluoride and silicon as examples with a large and small band gap respectively. The transformation to natural orbitals was found to be significantly more impactful for the large gap LiF. Nonetheless, both the composite and interacting methods are able to reproduce the CCSD result to within 0.1 eV using roughly half of the virtual space. This reduction in the number of retained virtuals leads to a significant computational savings and should enable the application of periodic coupled-cluster theory to systems with larger unit cells, bigger basis sets, and more dense Brillouin zone sampling. However, CCSD may not achieve the necessary precision for some correlated materials and an approximate treatment of triple excitations using similar active space ideas – such as active-space CC or CC(P;Q) – is a promising future direction for solid-state CC theory.

Although the composite method gives results that are comparable to the interacting method

for the ground state and first excited states, it has a number of disadvantages. First, the composite method does not yield an accurate wavefunction; instead, it relies upon error cancellation in the energies of various inaccurate wavefunctions. Therefore, it does not provide a natural route towards the calculation of accurate observables other than the energy (however, see Ref. [14] for a recent discussion). Second, not all applications of EOM-CCSD require the explicit enumeration of eigenvalues and eigenvectors. In particular, the calculation of frequency-dependent quantities, such as the Green's function [81] or other spectra [163], only requires the solution  $|X_B(\omega)\rangle$  of a system of linear equations,  $(\omega - \tilde{H}_N)|X_B(\omega)\rangle = |B\rangle$ , where  $|B\rangle$  is a known state. The solution of this system of linear equations is naturally obtained using iterative algorithms, such as the generalized minimal residual method, which only require matrix-vector multiplications. While a composite approach does not provide a natural solution to these calculations (again see Ref. [14]), the interacting method yields a single, accurate, reduced-cost matrix-vector multiplication. The development and testing of such an approach for the calculation of spectra, especially for solid-state systems, is now ongoing in our research group.

## Chapter 4: Finite-size effects in post-Hartree-Fock calculations of solids

The material for this chapter was taken from a manuscript currently being written by Tim Berkelbach, Xiao Wang, and Malte Lange.

### 4.1 Introduction

Electronic structure calculations of solids are inevitably prone to finite-size effects, although physically meaningful results are only obtained in the thermodynamic limit (TDL). These finite-size effects are apparent in the size of clusters used in incremental [164, 165, 166, 167] or embedding [168, 169, 170, 171] schemes and in the density of points sampled from the Brillouin zone in calculations with periodic boundary conditions [172, 173].

Many correlated electronic structure calculations can be separated into a mean-field part and a post-mean-field part; examples include the random-phase approximation, the  $G_0W_0$  approximation, and most quantum chemical post-Hartree-Fock methods such as Møller-Plesset perturbation theory and coupled-cluster theory. The mean-field and post-mean-field calculations do not necessarily exhibit the same finite-size behaviors, similarly to their dependence on the size of the single-particle basis set [174, 175]. Specifically, mean-field calculations that include exact exchange (including Hartree-Fock and hybrid density functional theory) can potentially exhibit a very large finite-size error with slow convergence to the TDL [176]. In contrast, the remaining electron correlation is expected to be local in space (for gapped materials such as semiconductors and insulators) such that the finite-size errors are small and quick to converge.

These notes review three approaches for the treatment of leading-order finite-size errors in Hartree-Fock and post-Hartree-Fock calculations of solids. The three approaches are based on (1) addressing all integrable divergences; (2) the periodic Ewald potential commonly used in the

quantum Monte Carlo community; and (3) a shifted Ewald potential that unifies the above two viewpoints. We emphasize that all three methods lead to the same result. Each is just a different picture for the same physical result.

## 4.2 Integrable divergences

We consider a supercell of  $N$  electrons and  $M$  nuclei with charges  $Z_A$ . The supercell has side length  $L$  and volume  $\Omega = L^3$ . Brillouin zone sampling with  $N_k$  points is equivalent to the use of a supercell composed of  $N_k$  primitive cells such that  $L \propto N_k^{1/3}$ . The properties of such a finite system can be thought of as having been calculated with an approximate quadrature for Brillouin zone integration. As long as the integrand is analytic, the quadrature error is  $O(L^{-3}) \sim O(N_k^{-1})$ . However, in practice, we may face larger finite-size errors of  $O(L^{-1}) \sim O(N_k^{-1/3})$  in periodic calculations based on HF, hybrid DFT, and post-HF methods. These errors can be attributed to non-analytic integrands, i.e. to an integrable divergence that typically occurs at  $\mathbf{G} = 0$ , where  $\mathbf{G}$  is a reciprocal lattice vector in plane-wave expansions.

### 4.2.1 Hartree-Fock theory

The HF energy, including the nuclear repulsion energy, is given by

$$\begin{aligned} E_0 &= \langle \Phi | H | \Phi \rangle \\ &= \sum_{i=1}^N [T_{ii} + V_{ii}] + \frac{1}{2} \sum_{ij} [\langle ij | ij \rangle - \langle ij | ji \rangle] + E_{\text{nuc}}, \end{aligned} \quad (4.1)$$

and contains a number of potentially divergent terms due to the long-range nature of the Coulomb interaction. For example, the Hartree component of the electron-electron interaction is

$$\begin{aligned} E_{\text{H}} &= \frac{1}{2} \sum_{ij} \langle ij | ij \rangle \\ &= \frac{1}{2} \sum_{ij} \frac{4\pi}{\Omega} \sum_{\mathbf{G}} \frac{\rho_{ii}(\mathbf{G}) \rho_{jj}(-\mathbf{G})}{G^2} \end{aligned} \quad (4.2)$$

where

$$\rho_{pq}(\mathbf{G}) = \frac{1}{\Omega} \int d^3r e^{i\mathbf{G}\cdot\mathbf{r}} \phi_p^*(\mathbf{r}) \phi_q(\mathbf{r}). \quad (4.3)$$

The  $\mathbf{G} = 0$  component of the Hartree energy is divergent because  $\rho_{ii}(\mathbf{G} = 0) = 1$ . However, due to charge neutrality, the divergent ( $\mathbf{G} = 0$ ) components of the Hartree energy, the electron-nuclear attraction energy, and the nuclear repulsion energy sum to zero and can therefore be ignored [177]. In particular, the nuclear repulsion energy can then be evaluated by Ewald summation, for which the elimination of the  $\mathbf{G} = 0$  term is equivalent to the conventional introduction of a neutralizing background charge density.

The only remaining divergence is in the  $i = j$  terms of the exchange energy (the  $i \neq j$  terms are not divergent due to the orthogonality of the orbitals  $\rho_{i \neq j}(\mathbf{G} = 0) = 0$ ),

$$\bar{E}_X = -\frac{1}{2} \sum_i \frac{4\pi}{\Omega} \sum_{\mathbf{G}} \frac{\rho_{ii}(\mathbf{G}) \rho_{ii}(-\mathbf{G})}{G^2}. \quad (4.4)$$

In the thermodynamic limit,  $L \rightarrow \infty$ , the sum over reciprocal lattice vectors becomes an integral, and the divergence is integrable. Simply neglecting the  $\mathbf{G} = 0$  contribution yields a finite-size (quadrature) error that scales as  $L^{-1}$  per cell or  $N_k^{-1/3}$  in the presence of Brillouin zone sampling. The simplest correction, which can be found by a variety of mathematical and physical arguments [178, 179, 180, 176], leads to

$$\bar{E}'_X = -\frac{1}{2} \sum_i \left\{ \frac{4\pi}{\Omega} \sum_{\mathbf{G} \neq 0} \left[ \frac{\rho_{ii}(\mathbf{G}) \rho_{ii}(-\mathbf{G})}{G^2} \right] - v_M \right\} \quad (4.5)$$

where  $v_M$  is the Madelung constant of the supercell,

$$v_M = \frac{4\pi}{\Omega} \sum_{\mathbf{G} \neq 0} \frac{1}{G^2} - \frac{4\pi}{(2\pi)^3} \int d^3q \frac{1}{q^2}, \quad (4.6)$$

and is a negative quantity. The total correction to the exchange energy is clearly  $Nv_M/2$ . The Madelung constant is twice the energy of a periodic array of unit point charges with a compensating background charge density, which can be efficiently calculated by Ewald summation [181]. The

Madelung constant of the supercell goes to zero in the thermodynamic limit as  $L^{-1}$  and cancels the leading-order quadrature error in the exchange energy. The so-corrected exchange energy, and thus the total HF energy, has a remaining finite-size error that decays as  $L^{-3}$  or  $N_k^{-1}$  [176].

The same technique can be used during the construction of the Fock (or Kohn-Sham) matrix with eigenvalues (orbital energies) given by

$$\varepsilon_p = T_{pp} + V_{pp} + \sum_j [\langle pj|pj\rangle - \langle pj|jp\rangle]. \quad (4.7)$$

Ignoring the electron-nuclear and Hartree terms whose divergence components sum to zero, the  $\mathbf{G} = 0$  divergence is only problematic for the exchange term when  $j = p$ , i.e. for occupied orbitals only. Treating the divergence as above leads to

$$\varepsilon_a = T_{aa} + V_{aa} + \sum_j [\langle aj|aj\rangle - \langle aj|ja\rangle] \quad (4.8a)$$

$$\varepsilon_i = T_{ii} + V_{ii} + \sum_j [\langle ij|ij\rangle - \langle ij|ji\rangle] + v_M \quad (4.8b)$$

where all terms are understood to have their  $\mathbf{G} = 0$  components neglected. The Madelung constant is negative and thus the occupied orbitals are all rigidly shifted down in energy by  $|v_M|$  compared to their values in the absence of the finite-size correction. The occupied orbital energies converge to the thermodynamic limit as  $L^{-3}$  and  $L^{-1}$  with and without the correction, respectively. The unoccupied orbital energies do not have divergence components and therefore stay unaffected and converge as  $L^{-3}$  in both cases. Apparently, the Fock matrix is corrected by the Madelung constant only on the diagonal and all crystalline orbital coefficients are unchanged.

In the PySCF package [124], periodic HF and hybrid DFT calculations can be performed with or without the above correction by supplying the keyword argument `exxdiv='ewald'` or `exxdiv=None` to the KHF or KDFT constructors.

In Fig. 4.1, we show HF results calculated for the diamond crystal in the gth-dzvp basis calculated without and with these finite-size corrections. The finite-size errors of total HF energies,

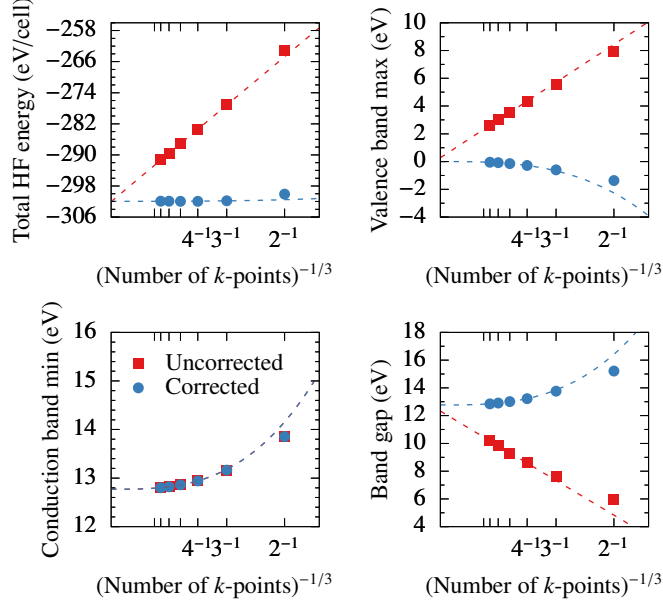


Figure 4.1: HF total energy, valence band maximum, conduction band minimum, and band gap of diamond in the gth-dzvp basis set. Results are uncorrected (red squares) or corrected (blue circles) according to a Madelung constant.

valence band maxima, and band gaps clearly scale as  $N_k^{-1/3}$  without the corrections; significant improvement of convergence ( $N_k^{-1}$ ) is observed after applying the correction scheme. As expected, the conduction band minima stay unaffected.

#### 4.2.2 Perturbation theory

Using the above finite-size corrected HF energy  $E_0$  and orbital energies  $\varepsilon_p$ , we partition the Hamiltonian in the usual Moller-Plesset form,  $H = H_0 + V$  with

$$H_0 = E_0 + \sum_p \varepsilon_p \{a_p^\dagger a_p\} \quad (4.9a)$$

$$V = \frac{1}{4} \sum_{pqrs} \langle pq||rs \rangle \{a_p^\dagger a_q^\dagger a_s a_r\} \quad (4.9b)$$

where  $\{\dots\}$  indicates normal-ordering with respect to the HF determinant. The ERIs  $\langle pq||rs \rangle$  are potentially problematic and must be handled on a case-by-case basis. As usual, the zeroth-order energy is exactly the HF one  $E_0$  and the first-order energy vanishes. As first pointed out in

Ref.[100], the MP2 (and CCSD) correlation energy can be written as

$$E_c^{(2)} = \frac{1}{4} \sum_{ijab} \frac{|\langle ij||ab \rangle|^2}{\varepsilon_i + \varepsilon_j - \varepsilon_a - \varepsilon_b} = \frac{1}{2} \sum_{\mathbf{G}} S(\mathbf{G})v(\mathbf{G}) \quad (4.10)$$

where

$$v(\mathbf{G}) = \frac{4\pi}{\Omega G^2} \quad (4.11)$$

$$S(\mathbf{G}) = \frac{1}{2} \sum_{ijab} \rho_{ia}(\mathbf{G})\rho_{jb}(-\mathbf{G}) \left[ 2t_{ij}^{ab} - t_{ij}^{ba} \right] \quad (4.12)$$

$$t_{ij}^{ab} = \frac{4\pi}{\Omega} \sum_{\mathbf{G}} \frac{\rho_{ia}(\mathbf{G})\rho_{jb}(-\mathbf{G})}{G^2}. \quad (4.13)$$

Note that Eqs. (4.11) and (4.12) are shared by MP2 and CCSD, while Eq. (4.13) is specific to MP2. Importantly, none of the terms appearing in the above reciprocal lattice vector sums is divergent at  $\mathbf{G} = 0$ , due to the orthogonality of occupied and virtual orbitals. In particular, the Taylor expansion of  $S(\mathbf{G})$  around  $\mathbf{G} = 0$  makes it clear that  $S(\mathbf{G}) = cG^2$  at small  $\mathbf{G}$  such that  $S(\mathbf{G})/G^2 = c$  at  $\mathbf{G} = 0$ ; neglecting this term incurs an error of  $O(L^{-3}) \sim O(N_k^{-1})$ , however the integration over this volume element can also be treated analytically in order to further reduce the finite-size error [100, 146].

If uncorrected HF orbital energies are used in the MP2 energy expression, then we expect the  $O(N_k^{-1/3})$  error to propagate into the MP2 correlation energy. In Fig. 4.2, we show the MP2 correlation energy for carbon diamond and LiF using uncorrected and corrected orbital energies. The results show the expected behavior based on the above discussion and clearly the use of corrected orbital energies is preferred.

### 4.2.3 Coupled-cluster theory

Using the above normal-ordered Hamiltonian Eq. (4.9), one can readily derive the CC amplitude and energy equations [182, 125]. The  $t_2$  amplitude equations have *six* integrable divergences (the  $t_1$  amplitude equations have none); one from the particle-particle ladder, one from the hole-hole ladder, and four from the particle-hole ladders.

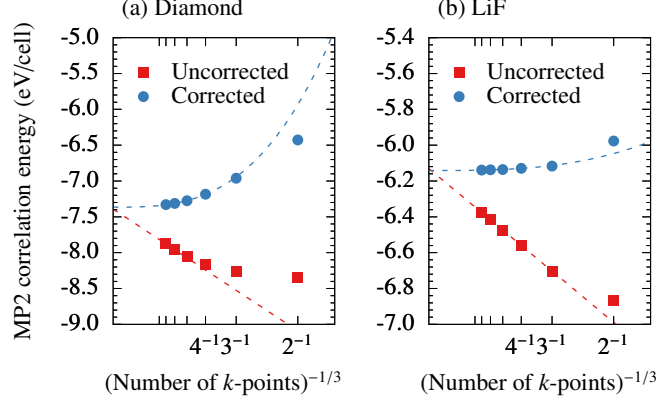


Figure 4.2: MP2 correlation energy of diamond (a) and LiF (b) in the gth-dzvp basis set using HF orbital energies that are uncorrected (red squares) or corrected (blue circles). Uncorrected MP2 energies have a finite-size error decaying as  $N_k^{-1/3}$  and corrected MP2 energies have a finite-size error decaying as  $N_k^{-1}$ .

For example, the particle-particle ladder contraction  $\sigma_{ij}^{ab}(\text{pp})$  is

$$\begin{aligned}\sigma_{ij}^{ab}(\text{pp}) &= \sum_{cd} \langle ab|cd \rangle t_{ij}^{cd} \\ &= \frac{4\pi}{\Omega} \sum_{\mathbf{G}} \sum_{cd} \frac{\rho_{ac}(\mathbf{G})\rho_{bd}(-\mathbf{G})}{G^2} t_{ij}^{cd}\end{aligned}\quad (4.14)$$

which has a divergent  $\mathbf{G} = 0$  term when  $c = a$  and  $d = b$ . Correcting the reciprocal lattice sum in the usual way leads to a Madelung constant,

$$\sigma_{ij}^{ab}(\text{pp}) = \frac{4\pi}{\Omega} \sum_{\mathbf{G} \neq 0} \sum_{cd} \frac{\rho_{ac}(\mathbf{G})\rho_{bd}(-\mathbf{G})}{G^2} t_{ij}^{cd} - v_{\text{M}} t_{ij}^{ab} \quad (4.15)$$

which we can see plays the role of an orbital energy correction, i.e. it is diagonal in the  $t$ -amplitude indices. If we collect the Madelung constants resulting from all six integrable divergences, we find  $-2v_{\text{M}} + 4v_{\text{M}} = 2v_{\text{M}}$ . This term cancels with a correction of  $-2v_{\text{M}}$  in the sum of two occupied orbital energies  $\varepsilon_i + \varepsilon_j$ . Therefore, the CCSD amplitude equations are completely independent of whether one corrects all integrable divergences or neglects  $\mathbf{G} = 0$  everywhere.

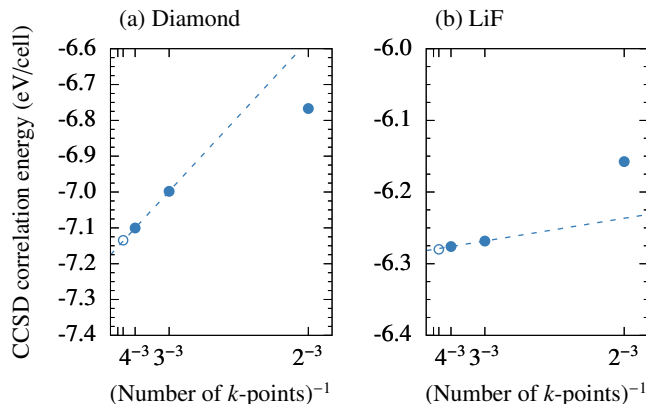


Figure 4.3: CCSD correlation energy of diamond (a) and LiF (b) in the gth-dzvp basis set. Open symbols at  $N_k = 5^3$  are calculated by a focal point technique combining results obtained with frozen virtual orbitals and results from  $N_k = 4^3$ , i.e.  $E(5^3) = E_{\text{frz}}(5^3) + E(4^3) - E_{\text{frz}}(4^3)$ .

As mentioned in the previous subsection, the CCSD correlation energy can be written

$$E_c = \frac{1}{2} \sum_{\mathbf{G}} S(\mathbf{G})v(\mathbf{G}) \quad (4.16)$$

where  $S(\mathbf{G})$  is given by Eq. (4.12) but with the  $t$ -amplitudes determined by the CCSD amplitude equations; as shown above, these  $t$ -amplitudes can be determined without  $L^{-1} \sim N_k^{-1/3}$  quadrature error. The function  $S(\mathbf{G})$  again goes to zero as  $G^2$  and the correlation energy quadrature has an  $O(L^{-3}) \sim O(N_k^{-1})$  error despite the neglect of the  $\mathbf{G} = 0$  term. The form of  $S(\mathbf{G})$  near  $\mathbf{G} = 0$  can be determined by extrapolation and used to estimate the contribution from the neglected volume element; this gives a useful finite-size correction but one that does not alter the formal scaling of the finite-size error [xx]. This approach is similar to ones used in the QMC community that correct the *total* energy based on the electronic structure factor [183].

In summary, *unlike in MP2*, the CCSD correlation energy has a finite-size error that scales as  $L^{-3} \sim N_k^{-1}$  independent of whether or not one uses ERI contractions that have been Madelung-corrected to account for their integrable divergence.

In Fig. 4.3, we show the CCSD correlation energy for carbon diamond and LiF; the results qualitatively exhibit  $N_k^{-1}$  scaling, although we emphasize that we cannot go to large enough  $k$ -point meshes to unambiguously see this behavior.

#### 4.2.4 IP/EA equation-of-motion coupled-cluster theory

Even in the QMC community, the IP, EA, and bandgap have been assumed to exhibit a finite-size error that scales like  $L^{-1} \sim N_k^{-1/3}$  [184, 185, 186], consistent with our previous treatments in EOM-CCSD [1]. Below we provide a formal proof of the scaling for the finite-size errors in IP/EA-EOM-CCSD.

The matrix-vector product used in iterative eigensolvers for EOM-CCSD has a number of integrable divergences beyond those of the orbital energies and they only appear in the doubles-doubles block. In the case of IP-EOM-CCSD, there are three such terms: two from the particle-hole ladders and one from the hole-hole ladder, i.e.

$$\begin{aligned} \langle \Phi_{ij}^a | [\bar{H}, R_2(n)] | \Phi \rangle &= (\varepsilon_a - \varepsilon_i - \varepsilon_j) r_{ij}^a \\ &- \sum_{kc} \langle kb|jc \rangle r_{ik}^c - \sum_{kc} \langle kb|ic \rangle r_{kj}^c + \sum_{kl} \langle kl|ij \rangle r_{kl}^b + \dots \end{aligned} \quad (4.17)$$

As for CCSD, the Madelung constant correction will only occur on the diagonal. Collecting the Madelung constants, including those from the orbital energies, gives net  $-v_M$ . The same  $-v_M$  occurs on the diagonal of the singles-singles block (due to the orbital-energy term). An identical analysis for EA-EOM-CCSD finds that the Madelung constant corrections completely cancel. Therefore all IPs are shifted by  $-v_M$  compared to their values calculated by neglecting the integrable divergence, all EAs are unshifted, and all IP and EA eigenvectors are completely unchanged; these are exactly the same conclusions as for the HF eigenvalues and eigenvectors.

In addition to the matrix-vector product, we must also analyze the  $\mathbf{G} = 0$  limit of the IP/EA energy expression to determine the scaling of their finite-size errors. Within EOM-CCSD, this can be calculated in a linear fashion as

$$\text{EA} = \Delta E^{(N+1)}(n) = \frac{\langle \Phi^a | [\bar{H}, R(n)] | \Phi \rangle}{\langle \Phi^a | R(n) | \Phi \rangle} = \frac{\sigma^a}{r^a} \quad (4.18a)$$

$$-\text{IP} = \Delta E^{(N-1)}(n) = \frac{\langle \Phi_i | [\bar{H}, R(n)] | \Phi \rangle}{\langle \Phi_i | R(n) | \Phi \rangle} = \frac{\sigma_i}{r_i}. \quad (4.18b)$$

Unlike for the ground-state energy, the  $\mathbf{G} = 0$  limit of the two-body component of the above is an integrable divergence. In other words,

$$\lim_{\mathbf{G} \rightarrow 0} [(N \pm 1)S_{N \pm 1}(\mathbf{G}) - NS_N(\mathbf{G})] = (\text{cst}) + O(G^2). \quad (4.19)$$

In Ref.[186], a similar expression to Eqs. (4.18) was analyzed leading to the following corrections,

$$\text{EA} = \Delta E^{(N+1)}(n) = (\dots)_{\mathbf{G} \neq 0} - \frac{v_M}{2} \left( \frac{1}{\epsilon} - 1 \right) \quad (4.20a)$$

$$-\text{IP} = \Delta E^{(N-1)}(n) = (\dots)_{\mathbf{G} \neq 0} - \frac{v_M}{2} \left( \frac{1}{\epsilon} + 1 \right) \quad (4.20b)$$

where the subscript  $\mathbf{G} \neq 0$  indicates all terms are calculated by neglecting the  $\mathbf{G} = 0$  component and  $\epsilon$  is the dielectric constant of the material. These corrections agree with the above (and those from HF theory) when  $\epsilon = 1$ . However, they modify the correction whenever  $\epsilon \neq 1$ . The IP and EA are individually changed, and the band gap correction is  $v_M/\epsilon$  (the terms independent of  $\epsilon$  are due to the neutralizing backgrounds and cancel in the band gap calculation). Although derived in Ref.[186] from a many-body perspective, this dielectric-dependent correction has been known for a long time based on physical arguments, especially for charged defects in solids [187, 188] and used in some previous QMC calculations [184, 185].

In Fig. 4.4, we show the IP and EA calculated for diamond and LiF when the results are uncorrected, corrected with a Madelung constant like for the HF eigenvalues, or corrected with the additional inclusion of a dielectric constant  $\epsilon$ . Clearly the results with  $\epsilon$ -dependent corrections give the best performance. Furthermore, both the uncorrected and corrected results exhibit a finite-size error that scales like  $L^{-1} \sim N_k^{-1/3}$ . It is unclear whether the  $\epsilon$ -dependent correction completely eliminates this error or not; some papers claim that this correction gives a  $L^{-3} \sim N_k^{-1}$  finite-size error [189].

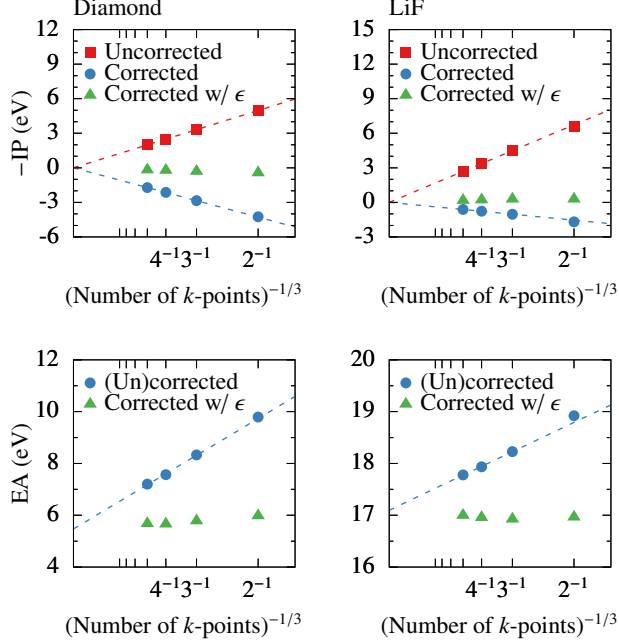


Figure 4.4: EOM-CCSD calculations of the IP and EA of diamond and LiF using the correction schemes described in the text. Calculations were done using the gth-dzvp basis with frozen virtuals; 4 virtual orbitals were correlated at each  $k$ -point.

### 4.3 The periodic Ewald potential

Rather than handling the  $\mathbf{G} = 0$  divergence on a term-by-term basis, it can be addressed from the outset in the many-body Hamiltonian. This approach is commonly adopted for quantum Monte Carlo (QMC) simulations of periodic systems [190]. Again, we consider a periodic supercell of  $N$  electrons and  $M$  nuclei with charges  $Z_A$  such that the supercell has net charge  $Q = \sum_A Z_A - N$ . We then add a positive and negative background charge density, which collectively enforce charge neutrality. The many-body Hamiltonian in first quantization, neglecting the nuclear kinetic energy, is then given by

$$\begin{aligned}
 H = & - \sum_{i=1}^N \frac{1}{2} \nabla_i^2 - \sum_{i=1}^N \sum_{A=1}^M Z_A v_E(r_i, R_A) + \sum_{i=1}^N \sum_{j>i}^N v_E(r_i, r_j) \\
 & + \sum_{A=1}^M \sum_{B>A}^M Z_A Z_B v_E(R_A, R_B) + \frac{N v_M}{2} + \frac{v_M}{2} \sum_{A=1}^M Z_A^2,
 \end{aligned} \tag{4.21}$$

where  $v_E(r, s)$  is commonly called the Ewald potential. Interested readers can refer to Ref. [190] for the derivation of Eq. (4.21). The Ewald potential is the periodic potential at position  $r$  due to a unit charge at position  $s$  along with its uniform neutralizing background. Furthermore, the zero of the potential is chosen so that the average value of  $v_E(r, s)$  vanishes, leading to the plane-wave representation

$$v_E(r, s) = \frac{1}{\Omega} \sum_{\mathbf{G} \neq 0} \frac{4\pi}{G^2} e^{i\mathbf{G} \cdot (r-s)}. \quad (4.22)$$

In practice, the above sum is conditionally convergent and  $v_E(r, s)$  is most efficiently computed by Ewald summation. The above expression should be understood as a distribution, which gives conditional convergence when used inside an integral, as is always the case in calculations with basis sets. In particular, the ERIs calculated with the Ewald potential are always well-defined,

$$\begin{aligned} \langle pq|rs \rangle &= \frac{4\pi}{\Omega} \sum_{\mathbf{G} \neq 0} \frac{\rho_{pr}(\mathbf{G})\rho_{qs}(-\mathbf{G})}{G^2} \\ &= \int dr_1 \int dr_2 \frac{[\rho_{pr}(r_1) - \delta_{pr}] [\rho_{qs}(r_2) - \delta_{qs}]}{r_{12}}. \end{aligned} \quad (4.23)$$

The second equality above emphasizes that the Ewald potential ERIs do not need to be evaluated with plane waves and alternative schemes are possible such as Gaussian density fitting [157]. The Madelung constant  $v_M$  is the same one defined in Eq. (4.6), i.e. it can be equivalently defined as the potential at the location of a point charge due to its periodic array of images and uniform neutralizing background; it can be expressed in terms of the Ewald potential,

$$v_M = \lim_{r \rightarrow s} \left( v_E(r, s) - \frac{1}{|r - s|} \right). \quad (4.24)$$

In summary, the second, third, and fourth terms in Eq. (4.21) are the pairwise interaction energy between the charges and their periodic images in a neutralizing background; the fifth and sixth terms are the interaction energy between each charge and its own periodic images in a neutralizing background. The fourth and sixth terms sum to  $E_{\text{nuc}}$ , the periodic nuclear repulsion energy as commonly calculated via Ewald summation.

### 4.3.1 Hartree Fock theory

Using the Hamiltonian in Eq. (4.21) as  $H = H_{\text{el}} + E_{\text{nuc}}$  to calculate the HF energy as the expectation value of an  $N$ -electron determinant gives

$$\begin{aligned} E_0 &= \langle \Phi | H_{\text{el}} | \Phi \rangle \\ &= \sum_{i=1}^N [T_{ii} + V_{ii}] + \frac{1}{2} \sum_{ij} [\langle ij | ij \rangle - \langle ij | ji \rangle] + \frac{N\nu_{\text{M}}}{2} \end{aligned} \quad (4.25)$$

where all one- and two-electron Coulomb integrals are calculated using  $v_{\text{E}}(r, s)$ , e.g.

$$\begin{aligned} \langle pq | rs \rangle &= \int d^3 r_1 \int d^3 r_2 \rho_{pr}(r_1) v_{\text{E}}(r_1, r_2) \rho_{qs}(r_2) \\ &= \frac{4\pi}{\Omega} \sum_{G \neq 0} \frac{\rho_{pr}(G) \rho_{qs}(-G)}{G^2}. \end{aligned} \quad (4.26)$$

Importantly, the use of the Ewald potential removes the need for any special treatment of terms with  $\mathbf{G} = 0$ . The HF energy is the same as found in the previous section, where the finite-size correction  $N\nu_{\text{M}}/2$  was due to the special treatment of an integrable divergence. However, the orbital energies do not agree. Treating the Madelung contribution as an additive constant to the total energy yields the orbital energies

$$\varepsilon_p = T_{pp} + V_{pp} + \sum_i [\langle pi | pi \rangle - \langle pi | ip \rangle], \quad (4.27)$$

which differs from the previous result because the occupied orbital energies are not modified. Therefore, the occupied orbital energies will converge slowly to the thermodynamic limit, with a finite-size error that decays as  $L^{-1} \sim N_k^{-1/3}$ . This result would be acceptable if not for the physical meaning of the occupied orbital energies as approximate ionization potentials according to Koopmans' theorem.

We can calculate the energies of the Hamiltonian in Eq. (4.21) with  $N + 1$  and  $N - 1$  electrons in order to understand this discrepancy, recalling that an additional neutralizing charge density is

implicitly added in order to compensate the additional charge. The energy obtained from electron addition, ignoring orbital relaxation, is

$$\begin{aligned}
E^{(N+1)} &= \langle \Phi^a | H_{\text{el}} | \Phi^a \rangle = \sum_{i=1}^N [T_{ii} + V_{ii}] + [T_{aa} + V_{aa}] \\
&+ \frac{1}{2} \sum_{ij} [\langle ij | ij \rangle - \langle ij | ji \rangle] + \sum_i [\langle ai | ai \rangle - \langle ai | ia \rangle] \\
&+ \frac{(N+1)v_M}{2} \\
&= E_0^{(N)} + \varepsilon_a + \frac{v_M}{2}
\end{aligned} \tag{4.28}$$

and from electron removal is (by the same manipulations)

$$E^{(N-1)} = \langle \Phi_i | H_{\text{el}} | \Phi_i \rangle = E_0^{(N)} - \varepsilon_i - \frac{v_M}{2}. \tag{4.29}$$

Therefore, when  $N$  is treated as a constant, the orbital energies  $\varepsilon_p$  do not satisfy Koopmans' theorem for electron affinities and ionization potentials. However, this is not the main problem; in fact, treating  $N$  as a one-body operator leads to different orbital energies that do satisfy Koopmans' theorem but for which both the occupied and the unoccupied orbital energies differ from those of the previous section and thus converge slowly as  $L^{-1}$ .

The main problem is that the periodic Hamiltonian potentially has an undesired interaction energy for a non-neutral system. The desired thermodynamic limit is  $N \rightarrow \infty$  with a single excess electron (or hole). Therefore, the interaction energy between the excess charge and its periodic images, along with the neutralizing background, is artificial. This excess energy is  $\Delta E = v_M/2$  and should be subtracted from the total energy of *both* charged systems, giving

$$E^{(N+1)} = \langle \Phi^a | H_{\text{el}} | \Phi^a \rangle - \frac{v_M}{2} = E_0^{(N)} + \varepsilon_a + \frac{v_M}{2} - \frac{v_M}{2} \tag{4.30a}$$

$$E^{(N-1)} = \langle \Phi_i | H_{\text{el}} | \Phi_i \rangle - \frac{v_M}{2} = E_0^{(N)} - \varepsilon_i - \frac{v_M}{2} - \frac{v_M}{2}. \tag{4.30b}$$

The electron affinity and ionization potential are then

$$\text{EA} = E^{(N+1)} - E_0^{(N)} = \varepsilon_a + \frac{v_M}{2} - \frac{v_M}{2} = \varepsilon_a \quad (4.31a)$$

$$\text{IP} = E_0^{(N)} - E^{(N-1)} = \varepsilon_i + \frac{v_M}{2} + \frac{v_M}{2} = \varepsilon_i + v_M, \quad (4.31b)$$

in agreement with the previous section's treatment of HF finite-size effects due to the integrable divergence in the exchange energy. For future reference, we emphasize that there are two corrections to the orbital energies (the second and third terms in Eq. (4.31)): the first correction is due to the uniform background and is identical for occupied and unoccupied orbitals (and cancels in the band gap); the second is due to the spurious image charge interaction and is opposite in sign for the occupied and virtual orbitals.

#### 4.3.2 Perturbation theory

The results of perturbation theory depend on the partitioning of the Hamiltonian. The most natural partitioning of the Hamiltonian in Eq. (4.21) is the usual Møller-Plesset one,  $H = H_0 + V$  with

$$H_0 = E_0 + \sum_a \varepsilon_a \{a_a^\dagger a_a\} + \sum_i \varepsilon_i \{a_i^\dagger a_i\} \quad (4.32a)$$

$$V = \frac{1}{4} \sum_{pqrs} \langle pq||rs \rangle \{a_p^\dagger a_q^\dagger a_s a_r\} \quad (4.32b)$$

where  $\{\dots\}$  indicates normal-ordering with respect to the HF determinant. As usual, the zeroth-order energy is exactly the HF one  $E_0$  and the first-order energy vanishes. The second-order MP2 correlation energy is

$$E_c^{(2)} = \frac{1}{4} \sum_{ijab} \frac{|\langle ij||ab \rangle|^2}{\varepsilon_i + \varepsilon_j - \varepsilon_a - \varepsilon_b}. \quad (4.33)$$

This approach to perturbation theory has the appealing property that the Madelung contribution only affects the HF energy and thus the correlation energy is independent of the Madelung constant.

Unfortunately, as discussed in the previous sections, the occupied orbital energies calculated in this way converge slowly as  $L^{-1}$ . Because they enter in the denominator, we expect the same slow convergence in the MP2 correlation energy. In Fig. 4.2, we show the MP2 correlation energy per primitive unit cell of diamond and lithium fluoride. When uncorrected orbital energies are used, the correlation energy converges as  $L^{-1}$  i.e. as  $N_k^{-1/3}$ ; the scaling becomes  $N_k^{-1}$  when orbital energies are corrected as discussed in Sec. 4.3.1. Quantitatively, the denominator is too small without the finite-size correction, compared to its value in the thermodynamic limit, and thus the MP2 correlation energy is too large in magnitude and converges from below.

An alternative Hamiltonian partitioning can be chosen based on one-electron energies that satisfy Koopmans' theorem with finite-size corrections,

$$H_0 = E_0 + \sum_a \varepsilon_a \{a_a^\dagger a_a\} + \sum_i (\varepsilon_i + v_M) \{a_i^\dagger a_i\} \quad (4.34a)$$

$$V = -v_M \sum_i \{a_i^\dagger a_i\} + \frac{1}{4} \sum_{pqrs} \langle pq || rs \rangle \{a_p^\dagger a_q^\dagger a_s a_r\}. \quad (4.34b)$$

The zeroth- and first-order energies are the same as before but the second-order MP2 energy is now

$$E_c^{(2)} = \frac{1}{4} \sum_{ijab} \frac{|\langle ij || ab \rangle|^2}{2v_M + \varepsilon_i + \varepsilon_j - \varepsilon_a - \varepsilon_b}. \quad (4.35)$$

Because the denominator now has a finite-size error that decays as  $L^{-3}$  (due to the cancellation of leading-order errors in  $2v_M + \varepsilon_i + \varepsilon_j$ ), we expect faster convergence to the thermodynamic limit. This behavior is confirmed in Fig. 4.2, which shows that this finite-size corrected MP2 correlation energy, based on the partitioning in Eqs. (4.34), converges as  $L^{-3}$ , i.e.  $N_k^{-1}$ . The correlation energy of lithium fluoride, a large gap insulator, converges especially quickly when corrected. Importantly, both approaches give the same correlation energy in the thermodynamic limit. The faster convergence demonstrates that the corrected approach is to be preferred. These results are in complete agreement with those derived on the basis of integrable divergences. This latter partitioning is also the one implicitly chosen in MP2 calculations on the finite uniform electron gas [191].

### 4.3.3 Coupled-cluster theory

Unlike finite-order perturbation theory, CC theory is invariant to a repartitioning of orbital energies. In that sense, the two partitionings above can be viewed as a level shift introduced in the CCSD iterations, which does not change the solution at convergence. However, the second partitioning above (where  $H_0$  and  $V$  both have Madelung constant shifts) is perhaps preferable because the initial guess will yield the improved version of MP2 theory. Numerical results (shown in Figs. 4.2 and 4.3) also indicate that this version of MP2 theory at a finite  $k$ -point grid is in better agreement with the converged CCSD solution and so presumably fewer iterations are required.

This invariance to Madelung corrections is the same as that determined in the the previous section on integrable divergences. In particular, this means we can treat the Madelung constant contribution to the total energy  $Nv_M/2$  as a part of the HF energy and calculate the correlation energy separately using integrals evaluated with the Ewald potential, i.e. with the  $\mathbf{G} = 0$  term explicitly removed. This result holds for any “wavefunction” based theory, but clearly not for perturbation theories.

### 4.3.4 IP/EA equation-of-motion coupled-cluster theory

The analysis of IP/EA EOM-CCSD with the Ewald potential is very similar to that for the HF eigenvalues and IPs/EAs. A straightforward treatment of the  $Nv_M/2$  term will give

$$\text{EA} = (\dots) + \frac{v_M}{2} \quad (4.36a)$$

$$\text{IP} = (\dots) + \frac{v_M}{2} \quad (4.36b)$$

and a bandgap that is unchanged, where all terms in  $(\dots)$  are calculated with the nondivergent Ewald potential. Again, a physical argument suggests that the interaction energy between the excess charges and their periodic images  $v_M/2$  is artificial and should be subtracted from the energies

of the  $(N \pm 1)$ -electron energies, giving

$$\text{EA} = (\dots) \quad (4.37\text{a})$$

$$\text{IP} = (\dots) + v_M. \quad (4.37\text{b})$$

If we further assume, physically, that the artificial interacting energy is screened by the dielectric constant of the material, then we should subtract  $v_M/(2\epsilon)$  instead; this gives

$$\text{EA} = (\dots) + \frac{v_M}{2} \left(1 - \frac{1}{\epsilon}\right) \quad (4.38\text{a})$$

$$\text{IP} = (\dots) + \frac{v_M}{2} \left(1 + \frac{1}{\epsilon}\right) \quad (4.38\text{b})$$

in agreement with the more careful analysis of the  $\mathbf{G} = 0$  limit presented above.

#### 4.4 The shifted Ewald potential

The many-body Hamiltonian based on the Ewald potential can be re-written as

$$\begin{aligned} H = & - \sum_{i=1}^N \frac{1}{2} \nabla_i^2 - \sum_{i=1}^N \sum_{A=1}^M Z_A [v_E(r_i, R_A) - v_M] \\ & + \sum_{i=1}^N \sum_{j>i}^N [v_E(r_i, r_j) - v_M] \\ & + \sum_{A=1}^M \sum_{B>A}^M Z_A Z_B [v_E(R_A, R_B) - v_M] \\ & + \frac{v_M}{2} \left( N - \sum_A Z_A \right)^2, \end{aligned} \quad (4.39)$$

where the final term vanishes for a neutral system. The shifted Ewald potential  $v_s(r) \equiv v_E(r) - v_M$  clearly has the Fourier components

$$v_s(G) = \begin{cases} 4\pi/\Omega G^2 & G \neq 0 \\ -v_M & G = 0. \end{cases} \quad (4.40)$$

#### 4.4.1 Hartree-Fock theory

Again we can evaluate the energy of an  $N$ -electron determinant,

$$\begin{aligned} E_0 &= \langle \Phi | H | \Phi \rangle \\ &= E_{\text{nuc}} + \sum_{i=1}^N [T_{ii} + V_{ii}] + \frac{1}{2} \sum_{ij} [\langle ij | ij \rangle - \langle ij | ji \rangle] \\ &= E_{\text{nuc}} + \sum_{i=1}^N [T_{ii} + \bar{V}_{ii}] + N v_M \sum_{A=1}^M Z_A \\ &\quad + \frac{1}{2} \sum_{ij} [\overline{\langle ij | ij \rangle} - \overline{\langle ij | ji \rangle}] - \frac{N^2 v_M}{2} + \frac{N v_M}{2} \end{aligned} \quad (4.41)$$

where the overline indicates that the pure Ewald interaction is used (without a Madelung constant shift). There are two terms of  $O(N^2)$ ,  $N^2 v_M - N^2 v_M / 2$ , arising from the electron-nuclear and the Hartree term of the electron-electron interaction. If we consider the nuclear-nuclear energy,

$$\begin{aligned} E_{\text{nuc}} &= \sum_{A=1}^M \sum_{B>A}^M Z_A Z_B [v_E(R_A, R_B) - v_M] \\ &= \bar{E}_{\text{nuc}} - \frac{v_M}{2} \sum_{A=1}^M Z_A^2 - v_M \sum_{A=1}^M \sum_{B>A}^M Z_A Z_B \\ &= \bar{E}_{\text{nuc}} - \frac{v_M}{2} \sum_{A=1}^M \sum_{B=1}^M Z_A Z_B = \bar{E}_{\text{nuc}} - \frac{N^2 v_M}{2}, \end{aligned} \quad (4.42)$$

we see a third term of  $O(N^2)$  that cancels the other two. Thus, the electron-nuclear, nuclear-nuclear, and Hartree term of the electron-electron interaction produce a sum that is independent of

whether one uses  $v_E(r, s)$  or  $v_E(r, s) - v_M$ . Thus we can write

$$\begin{aligned} E_0 &= \langle \Phi | H | \Phi \rangle \\ &= \bar{E}_{\text{nuc}} + \sum_{i=1}^N [T_{ii} + \bar{V}_{ii}] + \frac{1}{2} \sum_{ij} [\overline{\langle ij | ij \rangle} - \langle ij | ji \rangle]. \end{aligned} \quad (4.43)$$

In this form, it is clear that the correction  $Nv_M/2$  can be associated with the exchange energy. The Fock matrix follows simply as

$$\begin{aligned} f_{pq} &= T_{pq} + \bar{V}_{pq} + \bar{J}_{pq} + K_{pq} \\ &= T_{pq} + \bar{V}_{pq} + \sum_i [\overline{\langle pi | qi \rangle} - \langle pi | iq \rangle]. \end{aligned} \quad (4.44)$$

In the canonical HF basis, we can see that the Madelung constant modifies the occupied and unoccupied orbitals in different ways,

$$\varepsilon_j = \dots - \sum_i \langle ji | ij \rangle = \dots - \sum_i \overline{\langle ji | ij \rangle} + v_M \quad (4.45a)$$

$$\varepsilon_a = \dots - \sum_i \langle ai | ia \rangle = \dots - \sum_i \overline{\langle ai | ia \rangle}, \quad (4.45b)$$

consistent with the usual picture and all discussions above.

#### 4.4.2 Perturbation theory

It is simple to check that the Madelung shift does not alter the ERIs relevant for MP2 theory,

$$\begin{aligned} \langle ij | ab \rangle &= \frac{4\pi}{\Omega} \sum_{\mathbf{G} \neq 0} \frac{\rho_{ia}(\mathbf{G}) \rho_{jb}(-\mathbf{G})}{G^2} \\ &\quad - v_M \frac{4\pi}{\Omega} \rho_{ia}(\mathbf{G} = 0) \rho_{jb}(\mathbf{G} = 0), \end{aligned} \quad (4.46)$$

because the final term vanishes by orbital orthogonality. Therefore, only the orbital energies are affected as discussed above and this leads to the improved version of MP2 theory with  $L^{-3} \sim N_k^{-1}$  convergence.

### 4.4.3 Coupled-cluster theory

The analysis of CC theory with the shifted Ewald potential is similar to that in the presence of integrable divergences because the  $\mathbf{G} = 0$  terms need special attention. Like in that case, only ladder ERIs of the form  $\langle ij|kl\rangle$ ,  $\langle ab|cd\rangle$ , and  $\langle ia|jb\rangle$  are modified by the Madelung shift. Again if we consider the particle-particle ladder contraction,

$$\begin{aligned}\sigma_{ij}^{ab}(\text{pp}) &= \sum_{cd} \langle ab|cd\rangle t_{ij}^{cd} \\ &= \frac{4\pi}{\Omega} \sum_{\mathbf{G}} \sum_{cd} \frac{\rho_{ac}(\mathbf{G})\rho_{bd}(-\mathbf{G})}{G^2} t_{ij}^{cd} - v_{\text{M}} t_{ij}^{ab}\end{aligned}\tag{4.47}$$

we immediately recover the correction derived above in the section on integrable divergences. Clearly the shifted Ewald potential naturally ‘‘Madelung-corrects’’ all leading-order integrable divergences while leaving all other terms unchanged. As in all previous CC sections, a full analysis will show that all Madelung constant corrections cancel in the CCSD  $t$ -amplitude and energy equations.

### 4.4.4 IP/EA equation-of-motion coupled-cluster theory

For the IP/EA problem, one has to decide whether to include the final term in Eq. (4.39), i.e. the one that vanishes for neutral systems. However, note that this term adds an energy  $\Delta E = v_{\text{M}}/2$  to both the negatively and positively charged systems. This is precisely the energy that was argued to be artificial, representing the interaction between the excess charge and its periodic images. Make sure this makes sense. Therefore, if this term is kept, one recovers the same answer as when using the normal Ewald Hamiltonian (uncorrected); if this term is neglected, one recovers the same answers as when treating integrable divergences or when the results obtained with a normal Ewald Hamiltonian are corrected based on the physical argument of a fictitious interaction.

## 4.5 Conclusions and outlook

We have carried out a detailed discussion on three approaches that correct the leading-order ( $L^{-1} \sim N_k^{-1/3}$ ) finite-size errors in HF, MP2, CCSD, and IP/EA-EOM-CCSD calculations of solids. Mathematical and numerical proofs have been given for the improved scaling, i.e.  $L^{-3} \sim N_k^{-1}$ , leading to faster convergence of energies toward the thermodynamic limit (TDL). The present manuscript also establishes the equivalence of the three seemingly distinct approaches: despite their different treatments on Hamiltonian or the energy expression, the three approaches based on (1) addressing integrable divergences, (2) the Ewald potential, and (3) a shift Ewald potential actually describe the same physical results.

We would like to emphasize that our analysis of the finite-size errors can be extended to wavefunction-based methods in general. With a deeper understanding of the finite-size behavior, it is hoped that reliable extrapolation schemes can be applied to more approaches in order to avoid the necessity for very large super-cell calculations. The development of rigorous correction schemes for the residual finite-size errors is also of great interest for our future work.

## Chapter 5: Improved MP2 band gaps of semiconductors and insulators

The material for this chapter was taken from Reference [192]

### 5.1 Introduction

Second-order Møller-Plesset perturbation theory (MP2) is the simplest ab initio treatment of dynamical electron correlation. Its low cost makes it especially attractive for large systems including periodic solids. Although periodic MP2 has been found to perform reasonably well for the description of ground-state properties [193, 194, 195, 95, 5, 196, 197, 198, 199, 97, 200, 1], its performance is less satisfactory for charged excitation energies and band gaps [5, 6]. For example, in Ref. [5], MP2 was applied to thirteen semiconductors and insulators and exhibited average errors of 0.5% for lattice constants, 4.1% for bulk moduli, and 0.23 eV for cohesive energies, but predicted negative band gaps for materials that are known to be semiconducting, such as silicon and silicon carbide. This unsatisfactory performance was attributed to the lack of screening in finite-order perturbation theory. Indeed, the GW approximation [56, 201, 202] and equation-of-motion coupled-cluster theory [203, 82, 79, 204, 55] describe excitation energies with infinite-order perturbation theory and predict accurate band gaps of semiconductors [202, 205, 1], albeit with a computational cost that is higher than that of MP2.

Here, we study the performance of a second-order approximation to equation-of-motion coupled-cluster theory with single and double excitations (EOM-CCSD), first presented in Refs. [116, 117]. Despite making sequential second-order approximations, the method will be seen to be equivalent to the use of a self-energy containing all second-order diagrams and a few third-order diagrams.

## 5.2 Theory

Consider the Møller-Plesset partitioning of the many-body Hamiltonian, leading to the Hartree-Fock (HF) orbitals  $\phi_p(\mathbf{r})$  with orbital energies  $\varepsilon_p$ ; as usual, we denote the orbitals occupied in the HF determinant by  $i, j, k, l$ , those unoccupied by  $a, b, c, d$ , and general orbitals by  $p, q, r, s$ . The self-energy evaluated to second-order in perturbation theory is

$$\Sigma_{pq}^{\text{MP2}}(\omega) = \frac{1}{2} \sum_{lcd} \frac{V_{pl}^{cd} V_{cd}^{ql}}{\omega + \varepsilon_l - \varepsilon_c - \varepsilon_d} + \frac{1}{2} \sum_{kld} \frac{V_{pd}^{kl} V_{kl}^{qd}}{\omega + \varepsilon_d - \varepsilon_k - \varepsilon_l}, \quad (5.1)$$

where the antisymmetrized two-electron integrals are defined by  $V_{pq}^{rs} = \langle pq|rs \rangle - \langle pq|sr \rangle$ , with

$$\langle pq|rs \rangle = \int d\mathbf{x}_1 d\mathbf{x}_2 \phi_p^*(\mathbf{x}_1) \phi_q^*(\mathbf{x}_2) r_{12}^{-1} \phi_r(\mathbf{x}_1) \phi_s(\mathbf{x}_2) \quad (5.2)$$

and  $\mathbf{x}$  is a combined space and spin variable. Unlike the GW approximation, the MP2 self-energy has exact second-order exchange and is therefore free of self-screening error.

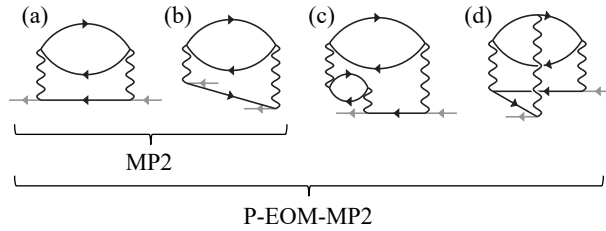


Figure 5.1: Self-energy diagrams included in the MP2 and P-EOM-MP2 Green's function beyond first-order. All diagrams are time-ordered with time increasing from left to right; hole lines point towards decreasing time and particle lines point towards increasing time. All Coulomb interactions (wavy lines) are antisymmetrized, yielding exchange diagrams not explicitly drawn here. The MP2 self-energy includes diagrams (a) and (b) only. The P-EOM-MP2 self-energy includes all four diagrams shown. The GW self-energy includes the non-exchange versions of diagrams (a), (b), (c), and many others.

An alternative theory can be obtained by a second-order approximation to EOM-CCSD, leading to a method originally referred to as EOM-MBPT(2) [116] or EOM-CCSD(2) [118]. In this method, the ground-state CCSD amplitudes are approximated by their MP2 values, avoiding the expensive iterative solution of the CCSD amplitude equations. In this work, we consider the ad-

ditional approximation of partitioning the EOM Hamiltonian into single and double excitation spaces and perturbatively treating the latter. Under this approximation, the large double excitation block of the similarity-transformed Hamiltonian is a diagonal matrix of orbital energy differences. This method has been referred to as DSO-GF [116] and P-EOM-MBPT(2) [117, 45]; because we always use a Hartree-Fock reference, we will refer to the method as P-EOM-MP2.

Unlike typical Green's function techniques, the EOM approach yields ionization potentials (IPs) and electron affinities (EAs) from separate eigenvalue calculations. In practice, these eigenvalues are found iteratively using the Davidson algorithm. As shown by Nooijen and Snijders [116], the P-EOM-MP2 IPs can equivalently be obtained from the self-consistent eigenvalues of a matrix with elements  $\varepsilon_i \delta_{ij} + \Sigma_{ij}^{\text{EOM}}(\omega)$ , where

$$\Sigma_{ij}^{\text{EOM}}(\omega) = \frac{1}{2} \sum_{lcd} \frac{V_{il}^{cd} V_{cd}^{jl}}{\varepsilon_j + \varepsilon_l - \varepsilon_c - \varepsilon_d} + \frac{1}{2} \sum_{kld} \frac{W_{id}^{kl} V_{kl}^{jd}}{\omega + \varepsilon_d - \varepsilon_k - \varepsilon_l} \quad (5.3)$$

and likewise for the EAs. The above matrix is clearly similar to the MP2 self-energy matrix (5.1), except for three differences. The first difference is the neglected coupling between the particle and hole spaces. Within the common diagonal approximation to the self-energy, this coupling is irrelevant and we have numerically confirmed that it is a negligible difference in this work. The second difference is the perturbative replacement of  $\omega = \varepsilon_j$  in one of the two terms. When this replacement is done in the MP2 self-energy, we find that it makes the results slightly *worse* and is thus not responsible for the improvement to be shown in the P-EOM-MP2 band gaps (vide infra).

The third and most important difference is the presence of the intermediate

$$W_{id}^{kl} = V_{id}^{kl} + P_{-}(kl) \sum_{me} V_{im}^{ke} t_{lm}^{de} + \frac{1}{2} \sum_{ef} V_{id}^{ef} t_{kl}^{ef} \quad (5.4)$$

where the antisymmetrization operator is  $P_{-}(kl)A_{kl} = A_{kl} - A_{lk}$  and

$$t_{ij}^{ab} = \frac{V_{ab}^{ij}}{\varepsilon_i + \varepsilon_j - \varepsilon_a - \varepsilon_b}. \quad (5.5)$$

Viewed in terms of the similarity-transformed Hamiltonian  $\bar{H} = e^{-T} H e^T$ , the first term in Eq. (5.3) reflects a renormalization of the one-body interactions due to ground-state correlation and the presence of  $W$  in the second term reflects a renormalization of the two-body interactions, i.e. it is a screened Coulomb interaction. Alternatively, the intermediate  $W$  can be understood as the inclusion of a few third-order self-energy diagrams, with a perturbative evaluation of the frequency denominator. In Fig. 5.1, we show the time-ordered self-energy diagrams included in the MP2 and P-EOM-MP2 Green’s functions beyond first-order (i.e. beyond Hartree-Fock).

Assuming  $n_{\text{occ}}$  occupied orbitals and  $n_{\text{vir}}$  virtual orbitals with  $n_{\text{vir}} > n_{\text{occ}}$ , then the more expensive electron affinity EOM-CCSD (EA-EOM-CCSD) has an iterative  $O(n_{\text{occ}}^2 n_{\text{vir}}^4)$  cost due to ground-state CCSD and an iterative  $O(n_{\text{occ}}^2 n_{\text{vir}}^3)$  cost per eigenvalue for excited-state matrix-vector multiplication. The P-EOM-MP2 method reduces the above to a non-iterative  $O(n_{\text{occ}}^2 n_{\text{vir}}^2)$  cost due to ground-state MP2 (ignoring the integral transformation) and an iterative  $O(n_{\text{occ}} n_{\text{vir}}^3)$  cost per eigenvalue due to excited-state matrix-vector multiplication. This significant cost reduction makes P-EOM-MP2 an attractive approach for complex materials. (Strictly speaking, P-EOM-MP2 has a non-iterative  $O(N^6)$  step due to the formation of the intermediate (5.4), but this is typically not the most time-consuming step. If necessary, the one-time intermediate construction can be avoided but results in an iterative  $O(N^5)$  cost.)

### 5.3 Results and Discussion

We have applied the above two theories to the calculation of the minimum band gaps of eleven simple, three-dimensional semiconductors and insulators. Seven have a diamond/zinc-blende crystal structure: Si, SiC, GaP, BP, GaN, C, BN; two have a rock-salt crystal structure: MgO and LiF; and two have a face-center cubic crystal structure: Ar and Ne. Calculations were done with periodic boundary conditions using the PySCF software package [157, 206]. All calculations were done without pseudopotentials using the all-electron cc-pVTZ basis set except for Ne and Ar, which used the aug-cc-pVTZ basis set. Calculations using larger basis sets (not shown) suggest that our results are close to the basis set limit, consistent with analogous results obtained with

the GW approximation [9]. Two-electron integrals were calculated by periodic Gaussian density fitting [207] using JKFIT auxiliary basis sets [208].

For charged excitation energies, finite-size effects are large [1, 186]. Here, we have included one Madelung constant correction to the occupied orbital energies and another to the final IPs. The former correction has no impact in wavefunction-based theories such as EOM-CCSD, but does have an impact in finite-order perturbation theories (similar to the differing behaviors of ground-state CCSD and MP2); the latter correction is familiar from periodic calculations of charged systems and can be given a many-body interpretation on the basis of the excited-state structure factor [186]. We have performed calculations with  $N_k = 2^3 - 5^3$   $k$ -points sampled uniformly in the Brillouin zone. Band gaps were then extrapolated to the thermodynamic limit assuming an  $O(N_k^{-1/3})$  finite-size error. Other treatments of finite-size effects are possible, but all are expected to exhibit finite-size errors with the same scaling.

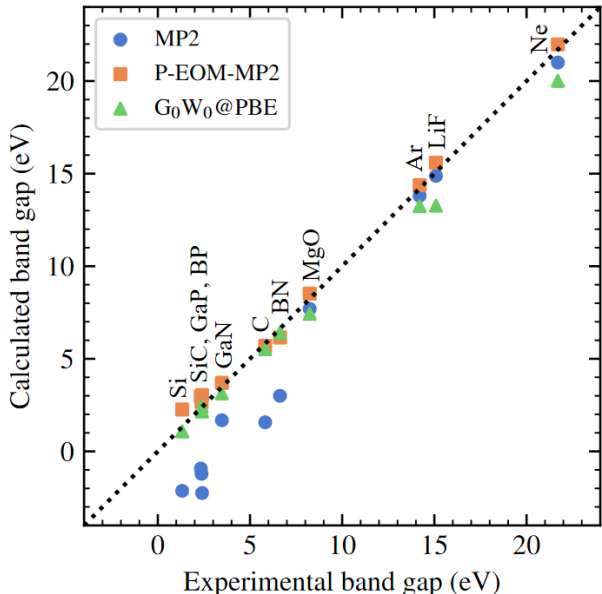


Figure 5.2: Comparison of calculated band gaps to experimental band gaps (including zero-point renormalization) for the eleven semiconducting and insulating materials indicated. GW approximation results were obtained at the  $G_0W_0@PBE$  level of theory.

In Fig. 5.2, we compare the minimum band gaps obtained by MP2, P-EOM-MP2, and the GW approximation to experimental values at 300 K. Because the calculations do not account for vibrational effects, we have adjusted the experimental values according to calculated electron-phonon

Material	$a$ (Å)	Reference		MP2		P-EOM-MP2		$G_0W_0@PBE$	
		Expt. $E_g$	el-ph	$E_g$	Error	$E_g$	Error	$E_g$	Error
Si	5.431	1.24	-0.06	-2.13	-3.43	2.26	0.96	1.08	-0.22
SiC	4.350	2.2	-0.17	-1.21	-3.58	2.66	0.29	2.44	0.07
GaP	5.450	2.27	-0.07	-0.93	-3.27	2.96	0.62	2.33	-0.01
BP	4.538	2.4	-	-2.25	(-4.65)	3.04	(0.64)	2.15	(-0.25)
GaN	4.520	3.30	-0.18	1.68	-1.80	3.70	0.22	3.13	-0.35
C	3.567	5.48	-0.33	1.57	-4.24	5.70	-0.11	5.52	-0.29
BN	3.615	6.2	-0.41	3.00	-3.61	6.15	-0.46	6.41	-0.20
MgO	4.213	7.67	-0.52	7.70	-0.49	8.52	0.33	7.43	-0.76
Ar	5.256	14.2	$\sim 0$	13.80	-0.40	14.38	0.18	13.24	-0.96
LiF	4.035	14.5	-0.59	14.88	-0.21	15.59	0.50	13.27	-1.82
Ne	4.429	21.7	$\sim 0$	21.00	-0.70	21.98	0.28	20.01	-1.69
MSE (eV)					-2.17		+0.28		-0.62
MUE (eV)					2.17		0.40		0.64

Table 5.1: Minimum band gap  $E_g$  as measured experimentally and as predicted by MP2, P-EOM-MP2 and  $G_0W_0@PBE$  (from Ref. [9]). Errors in predicted band gaps are calculated with respect to experimental values with electron-phonon (el-ph) renormalization. All energies are in eV. Mean signed error (MSE) and mean unsigned error (MUE) are given in eV. percentage. Results on BP were excluded from error statistics due to the missing electron-phonon renormalization. Experimental band gaps are from Refs. [209, 210, 211], zero-point contributions to electron-phonon renormalization are from Refs. [47, 212], the thermal contribution to electron-phonon renormalization for LiF is from Ref. [213], and  $G_0W_0@PBE$  results are from Refs. [9, 59].

renormalizations from the literature [47, 212] based on the Allen-Heine-Cardona framework [214, 215, 216]. We only include the zero-point renormalization for all materials except LiF, which has a sizable thermal contribution to the renormalization at 300 K [213]; for the other materials, this latter contribution is relatively small. Lattice expansion is already accounted for because our lattice constants are experimental 300 K values. Precise numbers and crystal geometries are given in Tab. 5.1. We note that experimental band gaps and calculated electron-phonon renormalizations vary throughout the literature.

Consistent with Ref. [5], we find that MP2 systematically underestimates the band gap and predicts negative band gaps for Si, GaP, BP, and SiC (our MP2 band gaps are similar to those of Ref. [5], but some differ by as much as 0.5 eV, which we attribute to differences in the treatment of core electrons, basis set effects, finite-size effects). Remarkably, the P-EOM-MP2 band gaps are a significant improvement and show good agreement for all materials. The mean signed error

(MSE) is +0.28 eV and the mean unsigned error (MUE) is 0.40 eV. The largest signed error is for Si (+0.96 eV), which has the smallest gap of all materials considered.

In Fig. 5.2 and Tab. 5.1, we also compare results to those calculated by the  $G_0W_0$  approximation with a PBE reference. For all materials except LiF, we compare to all-electron, full-frequency calculations by Zhu and Chan [9], which were performed with PySCF using identical treatments of core electrons and identical Gaussian basis sets. The result for LiF is from Ref. [59]. Remarkably, the P-EOM-MP2 and GW approximation perform similarly well, despite their underlying physical differences. Roughly speaking, the GW approximation performs better for materials with the smallest gaps while P-EOM-MP2 performs better for those with the largest gaps. The largest errors for the GW approximation are for the large-gap insulators, whose band gaps are underestimated by about 1 eV or more, which we attribute to the use of a PBE starting point and the absence of second-order exchange. For the GW approximation, the MSE is  $-0.62$  eV and the MUE is 0.64 eV.

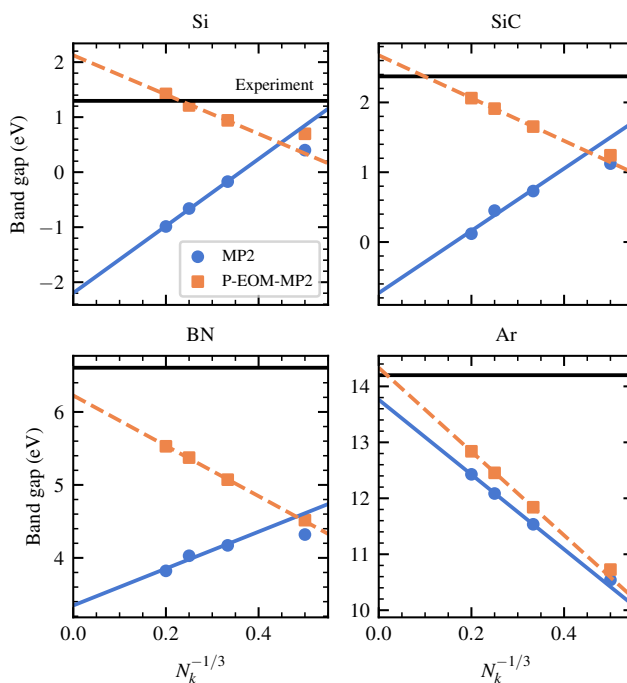


Figure 5.3: Convergence and extrapolation to the thermodynamic limit of the MP2 and P-EOM-MP2 band gaps for four example materials. Experimental values are corrected with a zero-point renormalization.

We performed additional calculations to estimate the effect of the various diagrams included

in the P-EOM-MP2 self-energy shown in Fig. 5.1. The HF band gap is always much too large and the direct second-order diagrams yield a large negative correction, which is largely responsible for the performance exhibited by MP2. Consistent with Ref. [5], we find that the second-order exchange diagrams make a small contribution ( $\lesssim 0.2$  eV) for small-gap materials but a larger contribution ( $\gtrsim 0.5$  eV) for large-gap materials. This can be attributed to the more localized nature of the electronic states in large-gap insulators. The screening diagram in Fig. 5.1(c) makes a large contribution (1 eV or more) for all materials and is most responsible for the significant improvement of P-EOM-MP2 over MP2. The final diagram in Fig. 5.1(d), a vertex correction beyond the GW approximation, typically raises the gap by about 0.2 eV.

In Fig. 5.3, we show the convergence of the band gap towards the thermodynamic limit for four of the materials considered here. As mentioned earlier, the finite-size error is large and must be removed by extrapolation. Interestingly, although MP2 and P-EOM-MP2 give similar band gaps for small  $k$ -point meshes, they exhibit very different convergence to the thermodynamic limit. This difference is largest for materials with small band gaps. We attribute this behavior to our use of Madelung constant corrections in the HF orbital energies. These corrections cause the HF gap to converge to the thermodynamic limit from above, such that the systems with smaller  $k$ -point meshes are more weakly correlated and the importance of third-order diagrams in the self-energy is diminished. On approach to the thermodynamic limit, the system becomes more strongly correlated and the results of the two methods deviate.

## 5.4 Conclusion

In conclusion, we have shown that the P-EOM-MP2 approach, a second-order approximation to EOM-CCSD, yields solid-state band gaps that are a significant improvement over those predicted by MP2. The success of P-EOM-MP2 contradicts the conventional wisdom that infinite-order screening is necessary for quantitative accuracy in band gap prediction. Rather, P-EOM-MP2 represents an affordable balance of low-order screening and exchange, yielding semiquantitative accuracy for materials with a wide range of band gaps. By starting from Hartree-Fock theory and

including antisymmetrization in all interaction vertices, the method is completely ab initio and free of self-interaction and self-screening errors. We note that P-EOM-MP2 is very similar to CC2 [119] and we therefore expect similar performance from the latter, which also includes some amount of orbital relaxation. Although P-EOM-MP2 has been found to perform well for three-dimensional materials, it will be interesting to apply it to low-dimensional semiconductors, where screening is more complicated.

## References

- [1] J. McClain, Q. Sun, G. K.-L. Chan, and T. C. Berkelbach, “Gaussian-Based Coupled-Cluster Theory for the Ground State and Band Structure of Solids,” J. Chem. Theory Comput., vol. 13, pp. 1209–1218, 2017.
- [2] G. H. Booth, A. Grüneis, G. Kresse, and A. Alavi, “Towards an exact description of electronic wavefunctions in real solids.,” Nature, vol. 493, pp. 365–70, 2013.
- [3] J. McClain, J. Lischner, T. Watson, D. A. Matthews, E. Ronca, S. G. Louie, T. C. Berkelbach, and G. K.-L. Chan, “Spectral functions of the uniform electron gas via coupled-cluster theory and comparison to the GW and related approximations,” Phys. Rev. B, vol. 93, no. 23, p. 235 139, 2016.
- [4] X. Wang and T. C. Berkelbach, “Excitons in solids from periodic equation-of-motion coupled-cluster theory,” arXiv:2001.11050, Jan. 29, 2020. arXiv: 2001.11050v1 [cond-mat.mtrl-sci].
- [5] A. Grüneis, M. Marsman, and G. Kresse, “Second-order møller–plesset perturbation theory applied to extended systems. II. structural and energetic properties,” J. Chem. Phys., vol. 133, no. 7, p. 074 107, 2010.
- [6] S. Isakov, A. A. Rusakov, D. Zgid, and E. Gull, “Effect of propagator renormalization on the band gap of insulating solids,” Physical Review B, vol. 100, no. 8, pp. 1–7, 2019. arXiv: 1812.07027.
- [7] T. N. Mihm, A. R. McIsaac, and J. J. Shepherd, “An optimized twist angle to find the twist-averaged correlation energy applied to the uniform electron gas,” Journal of Chemical Physics, vol. 150, no. 19, 2019. arXiv: 1906.04372.
- [8] C. Lin, F. H. Zong, and D. M. Ceperley, “Twist-averaged boundary conditions in continuum quantum Monte Carlo algorithms,” PRE - Statistical Physics, Plasmas, Fluids, and Related Interdisciplinary Topics, vol. 64, no. 1, p. 12, 2001. arXiv: 0101339 [cond-mat].
- [9] T. Zhu and G. K. L. Chan, “All-Electron Gaussian-Based G0W0for Valence and Core Excitation Energies of Periodic Systems,” Journal of Chemical Theory and Computation, vol. 17, no. 2, pp. 727–741, 2021. arXiv: 2007.03148.
- [10] A. Severo Pereira Gomes and C. R. Jacob, “Quantum-chemical embedding methods for treating local electronic excitations in complex chemical systems,” Annual Reports on the Progress of Chemistry - Section C, vol. 108, pp. 222–277, 2012.

- [11] T. Schäfer, F. Libisch, G. Kresse, and A. Grüneis, “Local embedding of coupled cluster theory into the random phase approximation using plane waves,” Journal of Chemical Physics, vol. 154, no. 1, 2021. arXiv: 2012.06165.
- [12] D. J. Coughtrie, R. Giereth, D. Kats, H. J. Werner, and A. Köhn, “Embedded Multireference Coupled Cluster Theory,” Journal of Chemical Theory and Computation, vol. 14, no. 2, pp. 693–709, 2018.
- [13] F. Hummel, T. Tsatsoulis, and A. Grüneis, “Low rank factorization of the Coulomb integrals for periodic coupled cluster theory,” J. Chem. Phys., vol. 145, p. 124 105, 2017.
- [14] A. Kumar and T. D. Crawford, “Frozen virtual natural orbitals for coupled-cluster linear-response theory,” J. Phys. Chem. A, vol. 121, no. 3, pp. 708–716, 2017.
- [15] A. Landau, K. Khistyayev, S. Dolgikh, and A. I. Krylov, “Frozen natural orbitals for ionized states within equation-of-motion coupled-cluster formalism,” J. Chem. Phys., vol. 132, no. 1, p. 014 109, 2010.
- [16] A. G. Taube and R. J. Bartlett, “Frozen natural orbital coupled-cluster theory: Forces and application to decomposition of nitroethane,” Journal of Chemical Physics, vol. 128, no. 16, 2008.
- [17] W. M. Foulkes, L. Mitas, R. J. Needs, and G. Rajagopal, “Quantum Monte Carlo simulations of solids,” Reviews of Modern Physics, vol. 73, no. 1, pp. 33–83, 2001.
- [18] E. A. Hylleraas, “Neue Berechnung der Energie des Heliums im Grundzustande, sowie des tiefsten Terms von Ortho-Helium,” Zeitschrift für Physik, vol. 54, no. 5-6, pp. 347–366, 1929.
- [19] W. Kutzelnigg, “R12 -dependent terms in the wave function as closed sums of partial wave amplitudes for large l,” Theor. Chim. Acta, vol. 68, p. 445, 1985.
- [20] J. Noga, S. Kedžuch, J. Šimunek, and S. Ten-no, “Explicitly correlated coupled cluster f12 theory with single and double excitations,” J. Chem. Phys., vol. 128, no. 17, p. 174 103, 2008.
- [21] G. Knizia, T. B. Adler, and H. J. Werner, “Simplified CCSD(T)-F12 methods: Theory and benchmarks,” Journal of Chemical Physics, vol. 130, no. 5, 2009.
- [22] G. Pestka, M. Bylicki, and J. Karwowski, “Geminals in Dirac-Coulomb Hamiltonian eigenvalue problem,” Journal of Mathematical Chemistry, vol. 50, no. 3, pp. 510–533, 2012.

- [23] T. Helgaker, S. Coriani, P. Jørgensen, K. Kristensen, J. Olsen, and K. Ruud, "Recent advances in wave function-based methods of molecular-property calculations," Chemical Reviews, vol. 112, no. 1, pp. 543–631, 2012.
- [24] A. J. C. Varandas, "Extrapolating to the one-electron basis-set limit in electronic structure calculations Extrapolating to the one-electron basis-set limit in electronic," vol. 244105, no. 2007, 2011.
- [25] A. J. Varandas, "CBS extrapolation in electronic structure pushed to the end: A revival of minimal and sub-minimal basis sets," Physical Chemistry Chemical Physics, vol. 20, no. 34, pp. 22 084–22 098, 2018.
- [26] A. J. C. Varandas, "Straightening the Hierarchical Staircase for Basis Set Extrapolations: A Low-Cost Approach to High-Accuracy Computational Chemistry," Annual Review of Physical Chemistry, vol. 69, no. 1, 2018.
- [27] D. G. Truhlar, "Basis-set extrapolation," Chemical Physics Letters, vol. 294, no. 1-3, pp. 45–48, 1998.
- [28] G. M. Barca, P. F. Loos, and P. M. Gill, "Many-Electron Integrals over Gaussian Basis Functions. I. Recurrence Relations for Three-Electron Integrals," Journal of Chemical Theory and Computation, vol. 12, no. 4, pp. 1735–1740, 2016.
- [29] A. Grüneis, S. Hirata, Y. ya Ohnishi, and S. Ten-No, "Perspective: Explicitly correlated electronic structure theory for complex systems," Journal of Chemical Physics, vol. 146, no. 8, 2017.
- [30] C. R. Myers, C. J. Umrigar, J. P. Sethna, and J. D. M. III, "Fock's expansion, Kato's cusp conditions, and the exponential ansatz Christopher," Physical Review A, vol. 44, no. 9, 1991.
- [31] W. Klopper, F. R. Manby, S. Ten-No, and E. F. Valeev, "R12 methods in explicitly correlated molecular electronic structure theory," International Reviews in Physical Chemistry, no. 3, pp. 427–468, 2007.
- [32] S. Ten-No, "Explicitly correlated wave functions: Summary and perspective," Theoretical Chemistry Accounts, vol. 131, no. 1, 2012.
- [33] S. Ten-no and J. Noga, "Explicitly correlated electronic structure theory from R12/F12 ansätze," Wiley Interdisciplinary Reviews: Computational Molecular Science, vol. 2, no. 1, pp. 114–125, 2012.
- [34] C. Hättig, W. Klopper, A. Köhn, and D. P. Tew, "Explicitly correlated electrons in molecules," Chemical Reviews, vol. 112, no. 1, pp. 4–74, 2012.

- [35] L. Kong, F. A. Bischoff, and E. F. Valeev, “Explicitly correlated R12/F12 methods for electronic structure,” Chemical Reviews, vol. 112, no. 1, pp. 75–107, 2012.
- [36] T. Shiozaki and H. J. Werner, “Multireference explicitly correlated F12 theories,” Molecular Physics, vol. 111, no. 5, pp. 607–630, 2013.
- [37] P. Pulay and S. Saebø, “Orbital-invariant formulation and second-order gradient evaluation in Møller-Plesset perturbation theory,” Theoretica Chimica Acta, vol. 69, no. 5-6, pp. 357–368, 1986.
- [38] G. Stollhoff and P. Fulde, “Description of intraatomic correlations by the Local Approach,” Zeitschrift für Physik B Condensed Matter and Quanta, vol. 29, no. 3, pp. 231–237, 1978.
- [39] P. Y. Ayala and G. E. Scuseria, “Linear scaling second-order Moller-Plesset theory in the atomic orbital basis for large molecular systems,” Journal of Chemical Physics, vol. 110, no. 8, pp. 3660–3671, 1999.
- [40] N. Flocke and R. J. Bartlett, “Correlation energy estimates in periodic extended systems using the localized natural bond orbital coupled cluster approach,” Journal of Chemical Physics, vol. 118, no. 12, pp. 5326–5334, 2003.
- [41] F. Neese, F. Wennmohs, and A. Hansen, “Efficient and accurate local approximations to coupled-electron pair approaches: An attempt to revive the pair natural orbital method,” J. Chem. Phys., vol. 130, no. 11, p. 114 108, 2009.
- [42] C. Riplinger and F. Neese, “An efficient and near linear scaling pair natural orbital based local coupled cluster method,” Journal of Chemical Physics, vol. 138, no. 3, 2013.
- [43] C. Riplinger, B. Sandhoefer, A. Hansen, and F. Neese, “Natural triple excitations in local coupled cluster calculations with pair natural orbitals,” Journal of Chemical Physics, vol. 139, no. 13, 2013.
- [44] Y. He, Z. He, and D. Cremer, “Comparison of CCSDT-n methods with coupled-cluster theory with single and double excitations and coupled-cluster theory with single, double, and triple excitations in terms of many-body perturbation theory - What is the most effective triple-excitation me,” Theoretical Chemistry Accounts, vol. 105, no. 3, pp. 182–196, 2001.
- [45] J. J. Goings, M. Caricato, M. J. Frisch, and X. Li, “Assessment of low-scaling approximations to the equation of motion coupled-cluster singles and doubles equations,” J. Chem. Phys., vol. 141, no. 16, p. 164 116, 2014.

- [46] A. K. Dutta, N. Vaval, and S. Pal, “Lower scaling approximation to EOM-CCSD: A critical assessment of the ionization problem,” Int. J. Quantum Chem., no. January, e25594, 2018.
- [47] A. Miglio, V. Brousseau-Couture, E. Godbout, G. Antonius, Y. H. Chan, S. G. Louie, M. Côté, M. Giantomassi, and X. Gonze, “Predominance of non-adiabatic effects in zero-point renormalization of the electronic band gap,” npj Computational Materials, vol. 6, no. 1, 2020. arXiv: 2011.12765.
- [48] G. Antonius, S. Poncé, P. Boulanger, M. Côté, and X. Gonze, “Many-body effects on the zero-point renormalization of the band structure,” Physical Review Letters, vol. 112, no. 21, pp. 1–5, 2014.
- [49] R. Tutchton, C. Marchbanks, and Z. Wu, “Structural impact on the eigenenergy renormalization for carbon and silicon allotropes and boron nitride polymorphs,” Physical Review B, vol. 97, no. 20, pp. 1–16, 2018.
- [50] F. Karsai, M. Engel, G. Kresse, and E. Flage-Larsen, “Electron-phonon coupling in semiconductors within the GW approximation,” New Journal of Physics, vol. 20, no. 12, 2018.
- [51] Y. Zhang, Z. Wang, J. Xi, and J. Yang, “Temperature-dependent band gaps in several semiconductors: From the role of electron-phonon renormalization,” Journal of Physics Condensed Matter, vol. 32, no. 47, 2020.
- [52] J. M. Tomczak, M. Casula, T. Miyake, F. Aryasetiawan, and S. Biermann, “Combined GW and dynamical mean-field theory: Dynamical screening effects in transition metal oxides,” Epl, vol. 100, no. 6, 2012. arXiv: 1210.6580.
- [53] S. Biermann, F. Aryasetiawan, and A. Georges, “First-Principles Approach to the Electronic Structure of Strongly Correlated Systems: Combining the [Formula presented] Approximation and Dynamical Mean-Field Theory,” Physical Review Letters, vol. 90, no. 8, p. 4, 2003.
- [54] T. D. Crawford and H. F. Schaefer, “An Introduction to Coupled Cluster Theory for Computational Chemists,” in Reviews in Computational Chemistry, K. B. Lipkowitz and D. B. Boyd, Eds., Hoboken, NJ, USA: John Wiley & Sons, Inc., Jan. 2007, pp. 33–136, ISBN: 978-0-470-12591-5 978-0-471-35495-6.
- [55] M. F. Lange and T. C. Berkelbach, “On the Relation between Equation-of-Motion Coupled-Cluster Theory and the GW Approximation,” Journal of Chemical Theory and Computation, 2018. arXiv: 1805.00043.

- [56] L. Hedin, “New Method for Calculating the One-Particle Green’s Function with Application to the Electron-Gas Problem,” *Phys. Rev.*, vol. 139, no. 3A, pp. 796–823, 1965.
- [57] M. S. Hybertsen and S. G. Louie, “First-principles theory of quasiparticles: Calculation of band gaps in semiconductors and insulators,” *Phys. Rev. Lett.*, vol. 55, no. 13, pp. 1418–1421, 1985.
- [58] A. Schindlmayr and R. W. Godby, “Systematic Vertex Corrections through Iterative Solution of Hedin’s Equations Beyond the  $\text{GW}$  Approximation,” *Phys. Rev. Lett.*, vol. 80, no. 8, pp. 1702–1705, 1998.
- [59] M. Shishkin, M. Marsman, and G. Kresse, “Accurate quasiparticle spectra from self-consistent GW calculations with vertex corrections,” *Phys. Rev. Lett.*, vol. 99, no. 24, pp. 14–17, 2007.
- [60] P Romaniello, S Guyot, and L Reining, “The self-energy beyond GW: Local and nonlocal vertex corrections,” *J. Chem. Phys.*, vol. 131, no. 15, p. 154 111, 2009.
- [61] A. Grüneis, G. Kresse, Y. Hinuma, and F. Oba, “Ionization potentials of solids: The importance of vertex corrections,” *Phys. Rev. Lett.*, vol. 112, no. 9, p. 096 401, 2014.
- [62] P. S. Schmidt, C. E. Patrick, and K. S. Thygesen, “Simple vertex correction improves GW band energies of bulk and two-dimensional crystals,” *Phys. Rev. B*, vol. 96, no. 20, p. 205 206, 2017. arXiv: 1711.02922.
- [63] I. Shavitt and R. J. Bartlett, *Many-Body Methods in Chemistry and Physics: MBPT and Coupled-Cluster Theory*. Cambridge; New York: Cambridge University Press, 2009.
- [64] D. L. Freeman, “Coupled-cluster expansion applied to the electron gas: Inclusion of ring and exchange effects,” *Phys. Rev. B*, vol. 15, pp. 5512–5521, 1977.
- [65] P. Ring and P. Shuck, *The Nuclear Many-Body Problem*. Springer-Verlag Berlin Heidelberg, 1980.
- [66] G. E. Scuseria, T. M. Henderson, and D. C. Sorensen, “The ground state correlation energy of the random phase approximation from a ring coupled cluster doubles approach,” *J. Chem. Phys.*, vol. 129, no. 23, p. 231 101, 2008.
- [67] L. S. Cederbaum, “One-body Green’s function for atoms and molecules: theory and application,” *J. Phys. B At. Mol. Opt. Phys.*, vol. 8, p. 290, 1975.

- [68] W. von Niessen, J. Schirmer, and L. S. Cederbaum, “Computational methods for the one-particle green’s function,” Comput. Phys. Reports, vol. 1, no. 2, pp. 57–125, 1984.
- [69] J. V. Ortiz, “Partial third-order quasiparticle theory: Comparisons for closed-shell ionization energies and an application to the Borazine photoelectron spectrum,” J. Chem. Phys., vol. 104, no. 19, pp. 7599–7605, 1996.
- [70] ———, “An efficient, renormalized self-energy for calculating the electron binding energies of closed-shell molecules and anions,” Int. J. Quantum Chem., vol. 105, no. 6, pp. 803–808, 2005.
- [71] J. Schirmer and L. S. Cederbaum, “The two-particle-hole Tamm-Dancoff approximation (2ph-TDA) equations for closed-shell atoms and molecules,” J. Phys. B At. Mol. Phys., vol. 11, no. 11, pp. 1889–1900, 1978.
- [72] O Walter and J Schirmer, “The two-particle-hole Tamm-Dancoff approximation (2ph-TDA) for atoms,” J. Phys. B At. Mol. Phys., vol. 14, p. 3805, 1981.
- [73] J. Schirmer, L. S. Cederbaum, and O. Walter, “New approach to the one-particle Green’s function for finite Fermi systems,” Phys. Rev. A, vol. 28, no. 3, pp. 1237–1259, 1983.
- [74] J. Ortiz, “A nondiagonal, renormalized extension of partial third-order quasiparticle theory: Comparisons for closed-shell ionization energies,” J. Chem. Phys., vol. 108, pp. 1008–1015, 1998.
- [75] A. Szabo and N. S. Ostlund, Modern Quantum Chemistry. Dover Publications, 1996.
- [76] L. J. Holleboom and J. G. Snijders, “A comparison between the Moller–Plesset and Green’s function perturbative approaches to the calculation of the correlation energy in the many-electron problem,” J. Chem. Phys., vol. 93, no. 8, p. 5826, 1990.
- [77] J. J. Phillips and D. Zgid, “Communication: The description of strong correlation within self-consistent Green’s function second-order perturbation theory,” J. Chem. Phys., vol. 140, no. 24, p. 241 101, 2014.
- [78] A. A. Kananenka, J. J. Phillips, and D. Zgid, “Efficient Temperature-Dependent Green’s Functions Methods for Realistic Systems: Compact Grids for Orthogonal Polynomial Transforms,” J. Chem. Theory Comput., vol. 12, no. 2, pp. 564–571, 2016.
- [79] J. F. Stanton and J. Gauss, “Analytic energy derivatives for ionized states described by the equation-of-motion coupled cluster method,” J. Chem. Phys., vol. 101, no. 1994, p. 8938, 1994.

- [80] A. I. Krylov, "Equation-of-motion coupled-cluster methods for open-shell and electronically excited species: the Hitchhiker's guide to Fock space.," Ann. Rev. Phys. Chem., vol. 59, pp. 433–462, 2008.
- [81] M. Nooijen and J. G. Snijders, "Coupled cluster approach to the single-particle Green's function," Int. J. Quantum Chem. Quantum Chem. Symp., vol. 83, pp. 55–83, 1992.
- [82] M. Nooijen and J. G. Snijders, "Coupled cluster Green's function method: Working equations and applications," Int. J. Quantum Chem., vol. 48, no. 1, pp. 15–48, 1993.
- [83] K. Bhaskaran-Nair, K. Kowalski, and W. A. Shelton, "Coupled cluster Green function: Model involving single and double excitations," J. Chem. Phys., vol. 144, no. 14, p. 144 101, 2016.
- [84] B. Peng and K. Kowalski, "Coupled-cluster Green's function: Analysis of properties originating in the exponential parametrization of the ground-state wave function," Phys. Rev. A, vol. 94, no. 6, p. 062 512, 2016.
- [85] ———, "Properties of advanced coupled-cluster Green's function," Mol. Phys., vol. 116, no. 5-6, pp. 561–569, 2018.
- [86] H. Nishi, T. Kosugi, Y. Furukawa, and Y.-i. Matsushita, "Quasiparticle energy spectra of isolated atoms from coupled-cluster singles and doubles (CCSD): Comparison with exact CI calculations," 2018. arXiv: 1803.01512.
- [87] Y. Furukawa, T. Kosugi, H. Nishi, and Y. I. Matsushita, "Band structures in coupled-cluster singles-and-doubles Green's function (GFCCSD)," J. Chem. Phys., vol. 148, no. 20, p. 204 109, 2018. arXiv: 1803.01564.
- [88] T. Kosugi, H. Nishi, Y. Furukawa, and Y.-i. Matsushita, "Comparison of Green's functions for transition metal atoms using self-energy functional theory and coupled-cluster singles and doubles (CCSD)," J. Chem. Phys., vol. 224103, p. 224 103, 2018. arXiv: 1803.01520.
- [89] Q. Ou and J. E. Subotnik, "Comparison between GW and Wave-Function-Based Approaches: Calculating the Ionization Potential and Electron Affinity for 1D Hubbard Chains," J. Phys. Chem. A, vol. 120, p. 4514, 2016.
- [90] J. W. Knight, X. Wang, L. Gallandi, O. Dolgounitcheva, X. Ren, J. V. Ortiz, P. Rinke, T. Körzdörfer, and N. Marom, "Accurate Ionization Potentials and Electron Affinities of Acceptor Molecules III: A Benchmark of GW Methods," J. Chem. Theory Comput., vol. 12, no. 2, pp. 615–626, 2016.

- [91] T. Rangel, S. M. Hamed, F. Bruneval, and J. B. Neaton, "Evaluating the GW Approximation with CCSD(T) for Charged Excitations Across the Oligoacenes," *J. Chem. Theory Comput.*, vol. 12, no. 6, pp. 2834–2842, 2016.
- [92] K. Krause, M. E. Harding, and W. Klopper, "Coupled-cluster reference values for the GW27 and GW100 test sets for the assessment of GW methods," *Mol. Phys.*, vol. 8976, no. July 2015, p. 1952, 2015.
- [93] F. Caruso, M. Dauth, M. J. van Setten, and P. Rinke, "Benchmark of GW Approaches for the GW100 Test Set," *J. Chem. Theory Comput.*, vol. 12, p. 5076, 2016.
- [94] M. J. van Setten, F. Caruso, S. Sharifzadeh, X. Ren, M. Scheffler, F. Liu, J. Lischner, L. Lin, J. R. Deslippe, S. G. Louie, C. Yang, F. Weigend, J. B. Neaton, F. Evers, and P. Rinke, "GW100: Benchmarking G0W0 for Molecular Systems," *J. Chem. Theory Comput.*, vol. 11, no. 12, pp. 5665–5687, 2015.
- [95] M. Marsman, A. Grüneis, J. Paier, and G. Kresse, "Second-order Møller-Plesset perturbation theory applied to extended systems. I. Within the projector-augmented-wave formalism using a plane wave basis set," *J. Chem. Phys.*, vol. 130, no. 18, 2009.
- [96] A. Grüneis, G. H. Booth, M. Marsman, J. Spencer, A. Alavi, and G. Kresse, "Natural orbitals for wave function based correlated calculations using a plane wave basis set," *J. Chem. Theory Comput.*, vol. 7, no. 9, pp. 2780–2785, 2011.
- [97] M. Del Ben, J. Hutter, and J. Vandevondele, "Second-order moller-plesset perturbation theory in the condensed phase: An efficient and massively parallel gaussian and plane waves approach," *J. Chem. Theory Comput.*, vol. 8, no. 11, pp. 4177–4188, 2012.
- [98] A. Gruneis, J. J. Shepherd, A. Alavi, D. P. Tew, and G. H. Booth, "Explicitly correlated plane waves: Accelerating convergence in periodic wavefunction expansions," *J. Chem. Phys.*, vol. 139, no. 8, p. 084 112, 2013.
- [99] A. Grüneis, "A coupled cluster and Møller-Plesset perturbation theory study of the pressure induced phase transition in the LiH crystal," *J. Chem. Phys.*, vol. 143, no. 10, p. 102 817, 2015.
- [100] K. Liao and A. Grüneis, "Communication: Finite size correction in periodic coupled cluster theory calculations," *J. Chem. Phys.*, vol. 145, p. 141 102, 2016.
- [101] A. L. Fetter and J. D. Walecka, *Quantum Theory of Many-Particle Systems*. Dover Publications, 2003.
- [102] Y. Pavlyukh and W. Hübner, "Configuration interaction approach for the computation of the electronic self-energy," *Phys. Rev. B*, vol. 75, no. 20, pp. 1–7, 2007.

- [103] F. Bruneval, “Ionization energy of atoms obtained from GW self-energy or from random phase approximation total energies,” J. Chem. Phys., vol. 136, no. 19, 2012.
- [104] M. J. van Setten, F. Weigend, and F. Evers, “The GW-Method for Quantum Chemistry Applications: Theory and Implementation,” J. Chem. Theory Comput., vol. 9, no. 1, pp. 232–246, 2013.
- [105] F. Bruneval, T. Rangel, S. M. Hamed, M. Shao, C. Yang, and J. B. Neaton, “MOLGW 1: Many-body perturbation theory software for atoms, molecules, and clusters,” Comput. Phys. Commun., vol. 208, pp. 149–161, 2016.
- [106] K Emrich, “An Extension of the Coupled Cluster Formalism To Excited-States .2. Approximations and Tests,” Nucl. Phys. A, vol. 351, no. 3, pp. 397–438, 1981.
- [107] T. C. Berkelbach, arXiv: 1804.01037.
- [108] P.-O. Löwdin, “Studies in perturbation theory,” J. Mol. Spectrosc., vol. 10, no. 1-6, pp. 12–33, 1963.
- [109] A. A. Golubeva, P. A. Pieniazek, and A. I. Krylov, “A new electronic structure method for doublet states: Configuration interaction in the space of ionized 1h and 2h1p determinants,” J. Chem. Phys., vol. 130, no. 12, p. 124 113, 2009.
- [110] X. Ren, N. Marom, F. Caruso, M. Scheffler, and P. Rinke, “Beyond the GW approximation: A second-order screened exchange correction,” Phys. Rev. B, vol. 92, no. 8, pp. 1–6, 2015.
- [111] E. Maggio, P. Liu, M. J. Van Setten, and G. Kresse, “GW100: A Plane Wave Perspective for Small Molecules,” J. Chem. Theory Comput., vol. 13, no. 2, pp. 635–648, 2017.
- [112] M. Govoni and G. Galli, “GW100: Comparison of Methods and Accuracy of Results Obtained with the WEST Code,” J. Chem. Theory Comput., vol. Article ASAP, 2018.
- [113] A. K. Dutta, N. Vaval, and S. Pal, “Performance of the EOMIP-CCSD (2) method for determining the structure and properties of doublet radicals: A benchmark investigation,” J. Chem. Theory Comput., vol. 9, no. 10, pp. 4313–4331, 2013.
- [114] A. K. Dutta, J. Gupta, H. Pathak, N. Vaval, and S. Pal, “Partitioned EOMEA-MBPT(2): An efficient N 5 scaling method for calculation of electron affinities,” J. Chem. Theory Comput., vol. 10, no. 5, pp. 1923–1933, 2014.
- [115] V. Rishi, A. Perera, M. Nooijen, and R. J. Bartlett, “Excited states from modified coupled cluster methods: Are they any better than EOM CCSD?” J. Chem. Phys., vol. 146, no. 14, p. 144 104, 2017.

- [116] M. Nooijen and J. G. Snijders, “Second order many-body perturbation approximations to the coupled cluster Green’s function,” J. Chem. Phys., vol. 102, no. 4, p. 1681, 1995.
- [117] S. R. Gwaltney, M. Nooijen, and R. J. Bartlett, “Simplified methods for equation-of-motion coupled-cluster excited state calculations,” Chem. Phys. Lett., vol. 248, no. January, pp. 189–198, 1996.
- [118] J. F. Stanton and J. Gauss, “Perturbative treatment of the similarity transformed Hamiltonian in equation-of-motion coupled-cluster approximations,” J. Chem. Phys., vol. 103, no. 3, p. 1064, 1995.
- [119] O. Christiansen, H. Koch, and P. Jorgensen, “The second-order approximate coupled cluster singles and doubles model CC2,” Chem. Phys. Lett., vol. 243, no. 5-6, pp. 409–418, 1995.
- [120] J. N. Byrd, V. Rishi, A. Perera, and R. J. Bartlett, “Approximating electronically excited states with equation-of-motion linear coupled-cluster theory,” J. Chem. Phys., vol. 143, no. 16, p. 164 103, 2015.
- [121] J. W. Negele and H. Orland, Quantum Many-Particle Systems. Perseus Books, 1998.
- [122] G. Wälz, D. Usvyat, T. Korona, and M. Schütz, “A hierarchy of local coupled cluster singles and doubles response methods for ionization potentials,” J. Chem. Phys., vol. 144, no. 8, p. 084 117, 2016.
- [123] F. Weigend and R. Ahlrichs, “Balanced basis sets of split valence, triple zeta valence and quadruple zeta valence quality for H to Rn: Design and assessment of accuracy,” Phys. Chem. Chem. Phys., vol. 7, no. 18, p. 3297, 2005.
- [124] Q. Sun, T. C. Berkelbach, N. S. Blunt, G. H. Booth, S. Guo, Z. Li, J. Liu, J. D. McClain, E. R. Sayfutyarova, S. Sharma, S. Wouters, and G. K. L. Chan, “PySCF: the Python-based simulations of chemistry framework,” Wiley Interdiscip. Rev. Comput. Mol. Sci., vol. 8, no. 1, e1340, 2018.
- [125] R. J. Bartlett and M. Musial, “Coupled-cluster theory in quantum chemistry,” Rev. Mod. Phys., vol. 79, no. 1, pp. 291–352, 2007.
- [126] R. M. Richard, M. S. Marshall, O. Dolgounitcheva, J. V. Ortiz, J. L. Brédas, N. Marom, and C. D. Sherrill, “Accurate Ionization Potentials and Electron Affinities of Acceptor Molecules I. Reference Data at the CCSD(T) Complete Basis Set Limit,” J. Chem. Theory Comput., vol. 12, no. 2, pp. 595–604, 2016.
- [127] M. Schütz and F. R. Manby, “Linear scaling local coupled cluster theory with density fitting. Part I: 4-external integrals,” Phys. Chem. Chem. Phys., vol. 5, no. 16, pp. 3349–3358, 2003.

- [128] E. G. Hohenstein, S. I. Kokkila, R. M. Parrish, and T. J. Martínez, “Tensor hypercontraction equation-of-motion second-order approximate coupled cluster: Electronic excitation energies in O (N4) time,” *J. Phys. Chem. B*, vol. 117, no. 42, pp. 12 972–12 978, 2013.
- [129] M. F. Lange and T. C. Berkelbach, “Active space approaches combining coupled-cluster and perturbation theory for ground states and excited states,” *Mol Phys.*, vol. 118, 2020.
- [130] C. Sosa, J. Geertsen, G. W. Trucks, R. J. Bartlett, and J. A. Franz, “Selection of the reduced virtual space for correlated calculations. an application to the energy and dipole moment of h2o,” *Chem. Phys. Lett.*, vol. 159, no. 2-3, pp. 148–154, 1989.
- [131] A. G. Taube and R. J. Bartlett, “Frozen natural orbitals: Systematic basis set truncation for coupled-cluster theory,” *Collect. Czech. Chem. Commun.*, vol. 70, no. 6, pp. 837–850, 2005.
- [132] C. Hampel and H.-J. Werner, “Local treatment of electron correlation in coupled cluster theory,” *J. Chem. Phys.*, vol. 104, no. 16, pp. 6286–6297, Apr. 1996.
- [133] W. Li, P. Piecuch, J. R. Gour, and S. Li, “Local correlation calculations using standard and renormalized coupled-cluster approaches,” *J. Chem. Phys.*, vol. 131, no. 11, p. 114 109, 2009.
- [134] Z. Rolik and M. Kállay, “A general-order local coupled-cluster method based on the cluster-in-molecule approach,” *J. Chem. Phys.*, vol. 135, no. 10, p. 104 111, 2011.
- [135] J. Yang, G. K.-L. Chan, F. R. Manby, M. Schütz, and H.-J. Werner, “The orbital-specific-virtual local coupled cluster singles and doubles method,” *J. Chem. Phys.*, vol. 136, no. 14, p. 144 105, 2012.
- [136] M. Nooijen, “Combining coupled cluster and perturbation theory,” *J. Chem. Phys.*, vol. 111, no. 24, pp. 10 815–10 826, 1999.
- [137] A. D. Bochevarov and C. D. Sherrill, “Hybrid correlation models based on active-space partitioning: Correcting second-order møller-plesset perturbation theory for bond-breaking reactions,” *J. Chem. Phys.*, vol. 122, no. 23, p. 234 110, 2005.
- [138] P. Piecuch, S. A. Kucharski, and R. J. Bartlett, “Coupled-cluster methods with internal and semi-internal triply and quadruply excited clusters: Ccsdt and ccsdtq approaches,” *J. Chem. Phys.*, vol. 110, no. 13, pp. 6103–6122, Apr. 1999.
- [139] P. Piecuch, “Active-space coupled-cluster methods,” *Mol. Phys.*, vol. 108, no. 21-23, pp. 2987–3015, Nov. 2010.

- [140] J. Shen and P. Piecuch, “Biorthogonal moment expansions in coupled-cluster theory: Review of key concepts and merging the renormalized and active-space coupled-cluster methods,” Chem. Phys., vol. 401, pp. 180–202, 2012.
- [141] ———, “Combining active-space coupled-cluster methods with moment energy corrections via the CC(p;q) methodology, with benchmark calculations for biradical transition states,” J. Chem. Phys., vol. 136, no. 14, p. 144 104, 2012.
- [142] R. H. Myhre, A. M. S. de Merás, and H. Koch, “The extended CC2 model ECC2,” Mol. Phys., vol. 111, no. 9-11, pp. 1109–1118, 2013.
- [143] R. H. Myhre, A. M. J. S. de Merás, and H. Koch, “Multi-level coupled cluster theory,” J. Chem. Phys., vol. 141, no. 22, p. 224 105, 2014.
- [144] R. H. Myhre and H. Koch, “The multilevel CC3 coupled cluster model,” The Journal of Chemical Physics, vol. 145, no. 4, p. 044 111, 2016.
- [145] G. H. Booth, A. Grüneis, G. Kresse, and A. Alavi, “Towards an exact description of electronic wavefunctions in real solids,” Nature, vol. 493, no. 7432, pp. 365–370, 2012.
- [146] T. Gruber, K. Liao, T. Tsatsoulis, F. Hummel, and A. Grüneis, “Applying the coupled-cluster ansatz to solids and surfaces in the thermodynamic limit,” Phys. Rev. X, vol. 8, no. 2, p. 021 043, 2018.
- [147] A. Pulkin and G. K.-L. Chan, “First principles coupled cluster theory of the electronic spectrum of the transition metal dichalcogenides,” [arXiv:1909.10886](https://arxiv.org/abs/1909.10886), Sep. 24, 2019. [arXiv: 1909.10886v1](https://arxiv.org/abs/1909.10886v1) [[cond-mat.mtrl-sci](https://arxiv.org/archive/cond-mat)].
- [148] Y. Gao, Q. Sun, J. M. Yu, M. Motta, J. McClain, A. F. White, A. J. Minnich, and G. K.-L. Chan, “Electronic structure of bulk manganese oxide and nickel oxide from coupled cluster theory,” [arXiv:1910.02191](https://arxiv.org/abs/1910.02191), Oct. 5, 2019. [arXiv: 1910.02191v2](https://arxiv.org/abs/1910.02191v2) [[cond-mat.mtrl-sci](https://arxiv.org/archive/cond-mat)].
- [149] J. F. Stanton and R. J. Bartlett, “The equation of motion coupled-cluster method. A systematic biorthogonal approach to molecular excitation energies, transition probabilities, and excited state properties,” J. Chem. Phys., vol. 98, no. 9, p. 7029, 1993.
- [150] M. W. Schmidt, E. A. Hull, and T. L. Windus, “Valence virtual orbitals: An unambiguous ab initio quantification of the lumo concept,” J. Phys. Chem. A, vol. 119, no. 41, pp. 10 408–10 427, 2015.
- [151] S. D. Folkestad and H. Koch, “Multilevel CC2 and CCSD methods with correlated natural transition orbitals,” J. Chem. Theory Comput., vol. 16, no. 1, pp. 179–189, 2020.

- [152] Z.-H. Cui, T. Zhu, and G. K.-L. Chan, “Efficient implementation of ab initio quantum embedding in periodic systems: Density matrix embedding theory,” J. Chem. Theory Comput., vol. 16, no. 1, pp. 119–129, 2020.
- [153] H. Q. Pham, M. R. Hermes, and L. Gagliardi, “Periodic electronic structure calculations with the density matrix embedding theory,” J. Chem. Theory Comput., vol. 16, no. 1, pp. 130–140, 2020.
- [154] T. Zhu, Z.-H. Cui, and G. K.-L. Chan, “Efficient formulation of ab initio quantum embedding in periodic systems: Dynamical mean-field theory,” J. Chem. Theory Comput., vol. 16, no. 1, pp. 141–153, 2020.
- [155] P. Piecuch, N. Oliphant, and L. Adamowicz, “A state-selective multireference coupled-cluster theory employing the single-reference formalism,” J. Chem. Phys., vol. 99, no. 3, pp. 1875–1900, 1993.
- [156] K. Kowalski and P. Piecuch, “The state-universal multi-reference coupled-cluster theory with perturbative description of core–virtual excitations,” Chem. Phys. Lett., vol. 334, no. 1-3, pp. 89–98, 2001.
- [157] Q. Sun, T. C. Berkelbach, N. S. Blunt, G. H. Booth, S. Guo, Z. Li, J. Liu, J. D. McClain, E. R. Sayfutyarova, S. Sharma, S. Wouters, and G. K.-L. Chan, “Pyscf: The python-based simulations of chemistry framework,” WIREs Comput. Mol. Sci., vol. 8, no. 1, e1340, 2017.
- [158] J. J. Shepherd and A. Grüneis, “Many-body quantum chemistry for the electron gas: Convergent perturbative theories,” Phys. Rev. Lett., vol. 110, no. 22, p. 226 401, 2013.
- [159] S. Goedecker, M. Teter, and J. Hutter, “Separable dual-space gaussian pseudopotentials,” Phys. Rev. B, vol. 54, no. 3, pp. 1703–1710, 1996.
- [160] C. Hartwigsen, S. Goedecker, and J. Hutter, “Relativistic separable dual-space gaussian pseudopotentials from h to rn,” Phys. Rev. B, vol. 58, no. 7, pp. 3641–3662, 1998.
- [161] J. VandeVondele, M. Krack, F. Mohamed, M. Parrinello, T. Chassaing, and J. Hutter, “Quickstep: Fast and accurate density functional calculations using a mixed gaussian and plane waves approach,” Comput. Phys. Commun., vol. 167, no. 2, pp. 103–128, 2005.
- [162] A. Milgram and M. P. Givens, “Extreme ultraviolet absorption by lithium fluoride,” Phys. Rev., vol. 125, no. 5, pp. 1506–1509, 1962.
- [163] H. Koch and P. Jørgensen, “Coupled cluster response functions,” J. Chem. Phys., vol. 93, no. 5, pp. 3333–3344, 1990.

- [164] H. Stoll, “The correlation energy of crystalline silicon,” Chemical Physics Letters, vol. 191, no. 6, pp. 548–552, 1992.
- [165] ———, “Correlation energy of diamond,” Phys. Rev. B, vol. 46, no. 11, pp. 6700–6704, Sep. 1992.
- [166] ———, “The correlation energy of crystalline silicon,” Chemical Physics Letters, vol. 191, no. 6, pp. 548–552, Apr. 1992.
- [167] B. Fiedler and J. Friedrich, “The incremental method–theory and applications in chemistry and physics,” Chemical Modelling, vol. 13, pp. 132–190, 2016.
- [168] P. Cortona, “Self-consistently determined properties of solids without band-structure calculations,” Phys. Rev. B, vol. 44, no. 16, pp. 8454–8458, Oct. 1991.
- [169] J. E. Inglesfield, “A method of embedding,” J. Phys. C: Solid State Phys., vol. 14, no. 26, pp. 3795–3806, Sep. 1981.
- [170] G. Knizia and G. K.-L. Chan, “Density Matrix Embedding: A Simple Alternative to Dynamical Mean-Field Theory,” Phys. Rev. Lett., vol. 109, no. 18, p. 186 404, Nov. 2012.
- [171] Q. Sun and G. K.-L. Chan, “Quantum Embedding Theories,” Acc. Chem. Res., vol. 49, no. 12, pp. 2705–2712, Dec. 2016.
- [172] D. J. Chadi and M. L. Cohen, “Special points in the brillouin zone,” Physical Review B, vol. 8, no. 12, pp. 5747–5753, 1973.
- [173] H. Monkhorst and J. Pack, “Special Points for Brilluoin-Zone integrations,” Physical Review B, vol. 13, no. 12, 1976. arXiv: 1011.1669v3.
- [174] A. Halkier, T. Helgaker, P. Jørgensen, W. Klopper, H. Koch, J. Olsen, and A. K. Wilson, “Basis-set convergence in correlated calculations on Ne, N<sub>2</sub>, and H<sub>2</sub>O,” Chemical Physics Letters, vol. 286, no. 3, pp. 243–252, Apr. 1998.
- [175] T. Helgaker, J. Olsen, A. Halkier, W. Klopper, and P. Jørgensen, “Basis-set convergence of the energy in molecular Hartree–Fock calculations,” Chemical Physics Letters, vol. 302, no. 5-6, pp. 437–446, 2002.
- [176] R. Sundararaman and T. A. Arias, “Regularization of the Coulomb singularity in exact exchange by Wigner-Seitz truncated interactions: Towards chemical accuracy in nontrivial systems,” Physical Review B - Condensed Matter and Materials Physics, vol. 87, no. 16, 2013. arXiv: 1302.6204.
- [177] H. J. Monkhorst, “Hartree-Fock density of states for extended systems,” Phys. Rev. B, vol. 20, no. 4, pp. 1504–1513, Aug. 1979.

- [178] F. E. Harris, L. Kumar, and H. J. Monkhorst, “Electronic-Structure Studies of Solids. II. “Exact” Hartree-Fock Calculations for Cubic Atomic-Hydrogen Crystals,” Phys. Rev. B, vol. 7, no. 6, pp. 2850–2866, Mar. 1973.
- [179] J. Paier, R. Hirschl, M. Marsman, and G. Kresse, “The Perdew–Burke–Ernzerhof exchange-correlation functional applied to the G2-1 test set using a plane-wave basis set,” J. Chem. Phys., vol. 122, no. 23, p. 234 102, Jun. 2005.
- [180] P. Broqvist, A. Alkauskas, and A. Pasquarello, “Hybrid-functional calculations with plane-wave basis sets: Effect of singularity correction on total energies, energy eigenvalues, and defect energy levels,” Phys. Rev. B, vol. 80, no. 8, p. 085 114, Aug. 2009.
- [181] P. Ewald, “Evaluation of optical and electrostatic lattice potentials,” Ann Phys, vol. 64, pp. 253–287, 1921.
- [182] G. D. Purvis and R. J. Bartlett, “A full coupled-cluster singles and doubles model: The inclusion of disconnected triples,” J. Chem. Phys., vol. 76, no. 4, pp. 1910–1918, Feb. 1982.
- [183] S. Chiesa, D. M. Ceperley, R. M. Martin, and M. Holzmann, “Finite-Size Error in Many-Body Simulations with Long-Range Interactions,” Phys. Rev. Lett., vol. 97, no. 7, p. 076 404, Aug. 2006.
- [184] G. E. Engel, Y. Kwon, and R. M. Martin, “Quasiparticle bands in a two-dimensional crystal found by GW and quantum Monte Carlo calculations,” Phys. Rev. B, vol. 51, no. 19, pp. 13 538–13 546, May 1995.
- [185] R. J. Hunt, M. Szyniszewski, G. I. Prayogo, R. Maezono, and N. D. Drummond, “Quantum Monte Carlo calculations of energy gaps from first principles,” Phys. Rev. B, vol. 98, no. 7, p. 075 122, Aug. 2018.
- [186] Y. Yang, V. Gorelov, C. Pierleoni, D. M. Ceperley, and M. Holzmann, “Electronic band gaps from quantum monte carlo methods,” Phys. Rev. B, vol. 101, no. 8, p. 085 115, 2020.
- [187] M. Leslie and N. J. Gillan, “The energy and elastic dipole tensor of defects in ionic crystals calculated by the supercell method,” J. Phys. C: Solid State Phys., vol. 18, no. 5, pp. 973–982, Feb. 1985.
- [188] G. Makov and M. C. Payne, “Periodic boundary conditions in ab initio calculations,” Phys. Rev. B, vol. 51, no. 7, pp. 4014–4022, Feb. 1995.
- [189] R. J. Needs, M. D. Towler, N. D. Drummond, P. López Ríos, and J. R. Trail, “Variational and diffusion quantum Monte Carlo calculations with the CASINO code,” J. Chem. Phys., vol. 152, no. 15, p. 154 106, Apr. 2020.

- [190] L. M. Fraser, W. M. C. Foulkes, G. Rajagopal, R. J. Needs, S. D. Kenny, and A. J. Williamson, "Finite-size effects and Coulomb interactions in quantum Monte Carlo calculations for homogeneous systems with periodic boundary conditions," *Phys. Rev. B*, vol. 53, no. 4, pp. 1814–1832, Jan. 1996.
- [191] J. J. Shepherd, A. Grüneis, G. H. Booth, G. Kresse, and A. Alavi, "Convergence of many-body wave-function expansions using a plane-wave basis: From homogeneous electron gas to solid state systems," *Phys. Rev. B*, vol. 86, no. 3, p. 035 111, Jul. 2012.
- [192] M. F. Lange and T. C. Berkelbach, "Improving MP2 band gaps with low-scaling approximations to EOM-CCSD," pp. 1–5, 2021. arXiv: 2105.11564.
- [193] P. Y. Ayala, K. N. Kudin, and G. E. Scuseria, "Atomic orbital laplace-transformed second-order møller–plesset theory for periodic systems," *J. Chem. Phys.*, vol. 115, no. 21, pp. 9698–9707, 2001.
- [194] S. Hirata, R. Podeszwa, M. Tobita, and R. J. Bartlett, "Coupled-cluster singles and doubles for extended systems," *J. Chem. Phys.*, vol. 120, no. 6, pp. 2581–2592, 2004.
- [195] S. Hirata and T. Shimazaki, "Fast second-order many-body perturbation method for extended systems," *Phys. Rev. B*, vol. 80, no. 8, p. 085 118, 2009.
- [196] L. Maschio, D. Usvyat, M. Schütz, and B. Civalleri, "Periodic local møller–plesset second order perturbation theory method applied to molecular crystals: Study of solid NH<sub>3</sub> and CO<sub>2</sub> using extended basis sets," *J. Chem. Phys.*, vol. 132, no. 13, p. 134 706, 2010.
- [197] D. Usvyat, L. Maschio, C. Pisani, and M. Schütz, "Second order local møller–plesset perturbation theory for periodic systems: The CRYSCOR code," *Z. Phys. Chem.*, vol. 224, no. 3-4, pp. 441–454, 2010.
- [198] M. Katouda and S. Nagase, "Application of second-order møller–plesset perturbation theory with resolution-of-identity approximation to periodic systems," *J. Chem. Phys.*, vol. 133, no. 18, p. 184 103, 2010.
- [199] F. Göttl, A. Grüneis, T. Bučko, and J. Hafner, "Van der waals interactions between hydrocarbon molecules and zeolites: Periodic calculations at different levels of theory, from density functional theory to the random phase approximation and møller–plesset perturbation theory," *J. Chem. Phys.*, vol. 137, no. 11, p. 114 111, 2012.
- [200] M. Del Ben, J. Hutter, and J. VandeVondele, "Electron correlation in the condensed phase from a resolution of identity approach based on the gaussian and plane waves scheme," *J. Chem. Theory Comput.*, vol. 9, no. 6, pp. 2654–2671, 2013.
- [201] G. Strinati, H. J. Mattausch, and W. Hanke, "Dynamical aspects of correlation corrections in a covalent crystal," *Phys. Rev. B*, vol. 25, no. 4, pp. 2867–2888, 1982.

- [202] M. S. Hybertsen and S. G. Louie, “Electron correlation in semiconductors and insulators: Band gaps and quasiparticle energies,” Phys. Rev. B, vol. 34, no. 8, pp. 5390–5413, 1986.
- [203] H. J. Monkhorst, “Calculation of properties with the coupled-cluster method,” Int. J. Quantum Chem., vol. 12, no. S11, pp. 421–432, 1977.
- [204] M. Nooijen and R. J. Bartlett, “Equation of motion coupled cluster method for electron attachment,” J. Chem. Phys., vol. 102, no. 9, pp. 3629–3647, 1995.
- [205] M. van Schilfgaarde, T. Kotani, and S. Faleev, “Quasiparticle self-consistent gw theory,” Phys. Rev. Lett., vol. 96, no. 22, p. 226 402, 2006.
- [206] Q. Sun, X. Zhang, S. Banerjee, P. Bao, M. Barbry, N. S. Blunt, N. A. Bogdanov, G. H. Booth, J. Chen, Z.-H. Cui, J. J. Eriksen, Y. Gao, S. Guo, J. Hermann, M. R. Hermes, K. Koh, P. Koval, S. Lehtola, Z. Li, J. Liu, N. Mardirossian, J. D. McClain, M. Motta, B. Mussard, H. Q. Pham, A. Pulkin, W. Purwanto, P. J. Robinson, E. Ronca, E. R. Sayfutyarova, M. Scheurer, H. F. Schurkus, J. E. T. Smith, C. Sun, S.-N. Sun, S. Upadhyay, L. K. Wagner, X. Wang, A. White, J. D. Whitfield, M. J. Williamson, S. Wouters, J. Yang, J. M. Yu, T. Zhu, T. C. Berkelbach, S. Sharma, A. Y. Sokolov, and G. K.-L. Chan, “Recent developments in the PySCF program package,” J. Chem. Phys., vol. 153, no. 2, p. 024 109, 2020.
- [207] Q. Sun, T. C. Berkelbach, J. D. McClain, and G. K.-L. Chan, “Gaussian and plane-wave mixed density fitting for periodic systems,” J. Chem. Phys., vol. 147, no. 16, p. 164 119, 2017.
- [208] F. Weigend, “A fully direct RI-HF algorithm: Implementation, optimised auxiliary basis sets, demonstration of accuracy and efficiency,” Phys. Chem. Chem. Phys., vol. 4, no. 18, pp. 4285–4291, 2002.
- [209] O. Madelung, Semiconductors: Data Handbook. 2004, ISBN: 9783642623325.
- [210] T. Chiang, K. Frank, H. Freund, A. Goldmann, F. J. Himpsel, U. Karlsson, R. Lecky, and W. Schneider, Electronic Structure of Solids: Photoemission Spectra and Related Data. Springer, 1989.
- [211] N. Schwentner, F.-J. Himpsel, V. Saile, M. Skibowski, W. Steinmann, and E. Koch, “Photoemission from Rare-Gas Solids: Electron Energy Distributions from the Valence Bands,” Physical Review Letters, vol. 34, no. 9, pp. 528–531, 1975. arXiv:1011.1669v3.
- [212] G. Antonius, S. Poncé, E. Lantagne-Hurtubise, G. Auclair, X. Gonze, and M. Côté, “Dynamical and anharmonic effects on the electron-phonon coupling and the zero-point renormalization of the electronic structure,”

Physical Review B - Condensed Matter and Materials Physics, vol. 92, no. 8, pp. 1–9, 2015. arXiv: 1505.07738.

- [213] B. Monserrat, “Correlation effects on electron-phonon coupling in semiconductors: Many-body theory along thermal lines,” Physical Review B, vol. 93, no. 10, pp. 1–6, 2016. arXiv: 1603.00551.
- [214] P. B. Allen and V Heine, “Theory of the temperature dependence of electronic band structures,” J. Phys. C, vol. 9, no. 12, pp. 2305–2312, 1976.
- [215] P. B. Allen and M. Cardona, “Theory of the temperature dependence of the direct gap of germanium,” Phys. Rev. B, vol. 23, no. 4, pp. 1495–1505, 1981.
- [216] F. Giustino, S. G. Louie, and M. L. Cohen, “Electron-phonon renormalization of the direct band gap of diamond,” Phys. Rev. Lett., vol. 105, no. 26, p. 265 501, 2010.